PROMPT GAMMA ANALYSIS OF SOIL AND WATER SAMPLES FOR ENVIRONMENTAL STUDIES

BY

LIADI FATAI AYOFE

A Thesis Presented to the
DEANSHIP OF GRADUATE STUDIES

KING FAHD UNIVERSITY OF PETROLEUM & MINERALS

DHAHRAN, SAUDI ARABIA

In Partial Fulfillment of the
Requirements for the Degree of

MASTER OF SCIENCE

In

PHYSICS

MAY 2017

KING FAHD UNIVERSITY OF PETROLEUM & MINERALS

DHAHRAN- 31261, SAUDI ARABIA

DEANSHIP OF GRADUATE STUDIES

This thesis, written by **LIADI FATAI AYOFE** under the direction his thesis advisor and approved by his thesis committee, has been presented and accepted by the Dean of Graduate Studies, in partial fulfillment of the requirements for the degree of **MASTER OF SCIENCE IN PHYSICS.**

Prof. Akthar A. Naqvi
(Advisor)
01-06-2017

Dr. Abdullah A. Al-sunaidi
Department Chairman

Dr. Fatah Z. Khiari
(Member)
01/June/2017

Dr. Salam A. Zummo
Dean of Graduate Studies

Dr. Watheq Ahmed Al-Basheer
(Member)
04/June/2017

4/6/17
Date

Dedicated to my parents and my wife

ACKNOWLEDGMENTS

First of all, I am grateful to the **Almighty Allah,** the lord of Universe for enabling me to complete my MSc program at King Fahd University of Petroleum and Minerals (KFUPM) Saudi Arabia.

I wish to express my sincere gratitude to my advisor Professor Akthar A. Naqvi, for his guidance and patience throughout the course of this research work. His fatherly care, continuous support and encouragement are greatly appreciated.

I am greatly indebted to Dr. Fatah Z. Khiari for his efforts and support. I am extremely grateful to him for his expert, sincere, and valuable guidance and encouragement extended to me.

I extend my special thanks to my committee member Dr. Fatah Z. Khiari and Dr. Watheq Ahmed Al-Basheer for their time and guidance. May Allah reward them abundantly.

I also thank Mr. Raashid Muhammad, Mr. Khateeb-Ur-Rehman, the late Mr. Abdul Qadeer Khokhar for their tremendous and priceless support towards the completion of this work. [Mr. Khokhar pass away, May Allah forgive him and make his abode in Al-janah firidaus Ameen].

I also present, my sincere gratitude to Dr. Abdullah A. Al-sunaidi, chairman of the Physics department for all the available departmental research facilities used.

I take this opportunity to present my sincere thanks to all the faculty members of the department of Physics for their help and encouragement.

Lastly, I am hugely indebted to my parents, my wife, my entire family, and my friends as well as the Nigerian Community in KFUPM for their love, affection and continuous moral support.

TABLE OF CONTENTS

LIST OF TABLES

LIST OF FIGURES

LIST OF ABBREVIATIONS

PGNAA	:	Prompt Gamma-ray Neutron Activation Analysis
NIS	:	Neutron Inelastic Scattering
TNC	:	Thermal Neutron Capture
LIBS	:	Laser Induced Breakdown Spectroscopy
ICP-OES	:	Inductively coupled plasma optical emission spectrometry
SMCL	:	Secondary Maximum Contaminant Levels
PHCs	:	Petroleum Hydrocarbons

ABSTRACT

Full Name : Liadi Fatai Ayofe

Thesis Title : Prompt Gamma Analysis of Soil and Water Samples for Environmental Studies

Major Field : Physics

Date of Degree : May, 2017

In this study, prompt gamma analysis of Mercury, Chromium, Nickel, Boron, Cadmium and Chlorine-contaminated water samples along with petroleum-contaminated soil samples was carried out. The toxic elements and petroleum hydrocarbons (PHCs)-contaminated samples were analyzed due to their significant adverse effect on the environment. The samples were analyzed using Thermal Neutron Capture (TNC) and 14 MeV neutrons inelastic scattering (NIS)-based Prompt Gamma-ray Neutron Activation Analysis (PGNAA) techniques. The study was undertaken at KFUPM 350 keV accelerator and MP320 portable neutron generator laboratories using $LaBr_3$:Ce, $CeBr_3$ and BGO gamma ray detectors.

For toxic element analysis in water samples, the minimum detection limit (MDC) of Hg, Cr, Ni, B, Cd and Cl in water samples were measured to be 0.15±0.05 wt.%, 1.03 ± 0.31 to 2.98 ± 0.91 wt.%, 1.98 ± 0.60 to 3.88 ± 1.18 wt.%, 24.4±7.43 ppm, 95.6±29.1 ppm and 1.47 ± 0.45 to 4.20 ± 1.28 wt.% respectively.

In the analysis of petroleum contaminated soil samples, carbon, silicon, hydrogen and oxygen concentrations were determined in benzene-contaminated soil samples. 14 MeV neutron beam moderation effects from moisture and petroleum (benzene) contents in the soil sample were quite significant. For a soil sample with fixed silicon concentration, the

intensity of silicon prompt gamma ray was decreasing with increasing moisture and petroleum concentration in the soil samples. This trend was validated through Monte Carlo simulation of the reaction. There is excellent agreement between experimental results and results of the Monte Carlo simulations.

ملخص الرسالة

الاسم الكامل: ليادي فاتي أيوف

عنوان الرسالة: استخدام أشعة غاما الفورية لتحليل عينات التربة والمياه للدراسات البيئية

التخصص: فيزياء

تاريخ الدرجة العلمية: مايو 2017

في هذه الدراسة، تم استخدام أشعة غاما الفورية لتحليل محتوى العناصر في عينات المياه الملوثة بالزئبق والكروميوم والنيكل والبورون والكادميوم والكلور وعينات التربة الملوثة بالمشتقات النفطية. تم تحليل محتوى هذه العناصر السامة وكذلك الهيدروكربونات الناتجة عن المشتقات النفطية بسبب تأثيرها الضار على البيئة. تم تحليل محتوى العناصر عن طريق اشعة غاما الفورية المنبعثة من العينات نتيجة اصطياد النيوترونات الحرارية (350 كيلوالكترون فولت) والاستطارة اللامرنة للنيوترونات الساقطة بطاقة مقدارها 14 ميجا الكترون فولت. أجريت الدراسة باستخدام مسارع جامعة الملك فهد للبترول والمعادن ومولّد النيوترونات المحمول كما تم استخدام ثلاثة أنواع من كواشف أشعة غاما؛ "لنثانوم بروماید" و "لنثانوم كلورايد" و "بزموث جرمانيت".

تم تحليل محتوى الزئبق والكروميوم والنيكل والبورون والكادميوم والكلور في عينات المياه ليكون 0.15 ± 0.05 نسبة مئوية بالوزن، 1.03 ± 0.31 إلى 2.98 ± 0.91 نسبة مئوية بالوزن، 1.98 ± 0.60 إلى 3.88 ± 1.18 نسبة مئوية بالوزن، 24.4 ± 7.43 جزء في المليون، 95.6 ± 29.1 جزء في المليون ، 1.47 ± 0.45 إلى 4.20 ± 1.28 نسبة مئوية بالوزن على التوالي.

في تحليل عينات التربة الملوثة بالبمشتقات النفطية، تم تحديد تركيز الكربون والسليكون والهيدروجين والأكسجين في عينات التربة الملوثة بالنفط. لقد لوحظ خلال هذه الدراسة اعتماد شدة اشعة غاما الفورية على رطوبة العينات وعلى محتوى المشتقات النفطية فيها. فبالنسبة لعينات التربة ذات تركيز سيليكون ثابت، كانت شدة أشعة غاما الفورية تتناقص مع زيادة الرطوبة وتركيز المشتقات النفطية في عينات التربة. ولقد تم استخدام طريقة "مونتي كارلو" للمحاكاة لدراسة هذه العلاقة ولقد كانت نتيجة هذه المحاكاة النظرية متوافقة تماما مع النتائج المخبرية.

CHAPTER 1

INTRODUCTION

Environmental studies mainly deal with contamination of the atmosphere, soil and water. The threats of soil and water contaminants to human health are well documented. The accumulation and migration of heavy metals in the water and soil environment as a result of human activities results in potential ecological and health risks [1]. Basic features of soil contamination such as accumulation and irreversibility are different from those of air and water contamination [2]. Soil accommodates many kinds of pollutants. Soil pollutants can be transferred from a compartment of the environment to another, like groundwater, and, consequently, have an effect on human health. Pollutants such as heavy metals continuously draw much attention because of their toxicity and persistence in the environment [2, 3]. In this study, work focuses on analysis of contamination of water and soil samples for environmental studies. Main focus was on water contamination due to toxic heavy metals from waste discharge of industries in to the surface and ground water. Also the soil contamination due to hydrocarbon contamination in the soil surface was studied [4].

The toxic elements boron, cadmium, mercury, chromium, nickel and chlorine were important because of their adverse effects on the environment. The main sources of pollution of cadmium and boron of environmental water are the manufacturing industries,

fertilizer production facilities, atmospheric deposition, and sewage sludge [4]. Accumulation of high concentrations of cadmium and boron in humans is due to consumption of crops grown on soil irrigated with cadmium and boron contaminated sewage water over long periods of time. This accumulation could result in numerous illnesses [4]. For example, the effects of high concentration of cadmium in humans can induce diarrhea, bone fracture, severe vomiting, damage to the central nervous system, cancer development, infertility, and ultimately death [5]. Higher concentrations of boron can damage human organs and cause stunted growth of agricultural products [5]. Mercury is a highly toxic element and its intake by humans may lead to memory loss, menstrual disorders in women, cardiovascular homoeostasis in children, increased muscular fatigue and reduced fertility rates. The increased intake of mercury by humans is due to its multiple pathways such as eating fish, contaminated water, flu vaccines, and cosmetics [6, 7]. Despite its many useful industrial applications such as in textile manufacturing, photoengraving, and wood preservation, chromium may also be harmful to humans and animals due to its several adverse effects on health such as skin tumors, hepatotoxicity, alteration in the reproductive function, bronchial asthma and nephrotoxicity [8,9]. Nickel is one of the carcinogenic metals and long exposure to nickel has been connected with increased risk of lung cancer, cardiovascular disease, neurological deficits, developmental deficits in childhood, and high blood pressure [10]. Additionally, nickel has been identified as a toxin that severely damages reproductive health and can lead to infertility, miscarriage, birth defects, and nervous system defects [11].

Ground water and surface water pollution is very serious in countries with freezing winter weather [12]. For such countries chloride contamination of ground and surface water is mainly due to direct addition of sodium chloride salt in environment during its spraying for de-icing of roads, parking lots, and other impervious surfaces in freezing winter [13,14]. The direct addition of chlorine to environment causes concern about degradation of quality of groundwater and surface water that may be used for drinking-water supply, aquatic habitat and for industrial use [15]. Due to corrosive nature of chloride salts, chloride contamination of feed water of steam-generating systems is also very harmful for steam boilers even at the parts per billion level of contamination. In the boilers during evaporation process, initial ppb range chlorine concentration, enriches exponentially resulting in serious harm to boiler vessel. In shorts chloride in water has adverse effects on environment and industry. The U.S. Environmental Protection Agency (USEPA) has set a maximum contaminant level (SMCL) of 250 mg/L for chloride in drinking water [16].

Like surface and ground water pollution due to toxic elements, soil contamination with hydrocarbon has alarming impact on the environment. It has attracted considerable public attention during the past few decades [17]. Many countries encountered serious problems of soil contamination by hydrocarbons [18,19]. Hydrocarbons are one of the most frequent categories of constant organic contaminants in the environment and are known to be toxic to numerous living organisms [20]. The occurrence of hydrocarbons in soils is not only harmful to humans, but has also a negative impact on plant development and growth [21,22]. Their destructive effects consist of reduction of photosynthetic pigments, shortening of roots and aerial organs, inhibition of seed germination, and slowdown of

nutrient assimilation. It is also likely that some fractions of hydrocarbon can dissolve biological membranes and, as a result, interrupt the building of plant root [23-27]. The effective control in environmental pollutant in water and soil require their monitoring in the environment. These require efficient and accurate techniques to determine the pollutant quantity in the environment through environmental surface water, ground water and soil samples analysis. There are several chemical and physical techniques available to carryout environmental sample analysis. Particularly important are X-ray and gamma ray techniques [28], inductively coupled plasma optical emission spectrometry (ICP-OES) technique [29], Gravimetric technique [30], Sequential extraction procedures technique [31], Laser Induced Breakdown Spectroscopy (LIBS) technique [32], etc… These techniques have their merit and disadvantages such as long analysis and complicated sample preparation. For instance, ICP-OES can't detect very low concentration levels of mercury in water. LIBS suffers from difficulty in quantifying inhomogeneous sample, lack of background elimination and signal saturation effects for high concentration elements due to self-absorption. Gravimetry lacks multi-elemental analysis, it usually analyzes a single element at a time. The disadvantages of sequential extraction procedures are the evidence for redistribution during fractionation and non-selectivity of reagents for each fraction. X-ray technique is limited to surface analysis.

1.1 Prompt Gamma Ray Neutron Activation Analysis Approach

Prompt Gamma Ray Neutron Activation Analysis (PGNAA) is an analytical technique used to determine elemental concentrations. PGNAA is a non-destructive, technique that is capable of measuring multi-elemental concentrations in bulk liquid and solid samples.

The continuous development of gamma ray detection capability, such as improved energy resolution and detection efficiency, has made PGNAA technique prominent in various disciplines. PGNAA has a wide range of applications in industry, mining, quality control, medical sciences, building construction and concrete corrosion, as well as environmental sciences [33-43]. In Prompt Gamma Ray Neutron Activation Analysis (PGNAA) method, the production of prompt gamma rays and irradiation of material with neutrons are achieved through either neutron inelastic scattering (n, n'γ) or thermal neutron capture (n_{th}, γ). Neutron Inelastic Scattering technique is denoted as **NIS** while Thermal Neutron Capture technique is denoted as **TNC.**

1.1.1 Prompt Gamma Ray Production Through Thermal Neutron Capture and Neutron Inelastic Scattering Reaction

Radiative neutron capture is the process in which a neutron is absorbed by a target nucleus to form an (excited) compound nucleus. The compound nucleus de-excites back to the ground state by emitting prompt and delayed gamma-rays (see Figure 1.1). The prompt gamma-ray intensity is proportional to the number of atoms and the energy values of the gamma –rays identify the nuclide. Each element emits a distinctive gamma-ray signature as it returns to a stable state. To be measured, the element must have a high capture cross section for thermal neutrons, and it must emit a gamma-ray within the energy window being analyzed. The amount of atoms of an element present in the sample must be adequate to produce a measurable intensity of gamma rays [44]. These gamma-rays are collected and measured with a high-resolution gamma-ray detector. The energy resolution of the

detector determines the capability of the detector to distinguish between two gamma rays with very close energies.

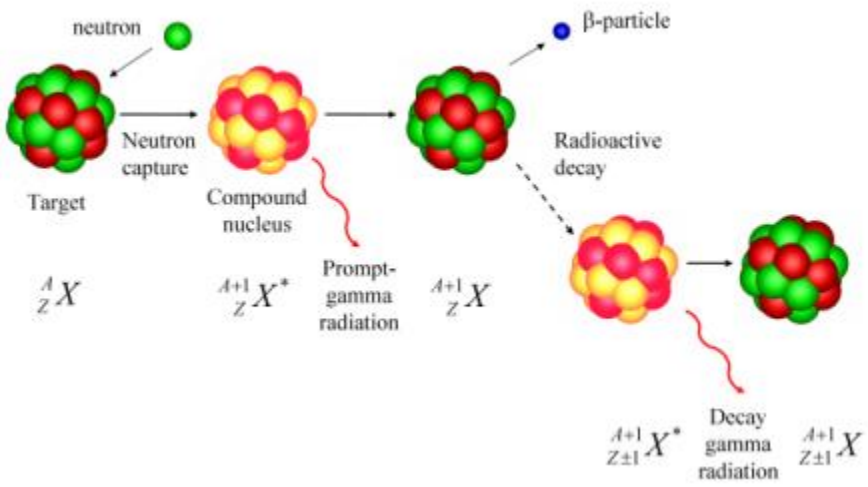

Figure 1.1: Schematic diagram illustrating thermal neutron capture process and decay products [32].

Neutron Inelastic scattering is a scattering in which the energy of excitation is transmitted to the scattering nucleus, and this excitation energy can be detected through the emitted gamma rays. During neutron inelastic scattering, the product nucleus will be left in an excited state after the emission of an inelastically scattered neutron. The nucleus will be excited to a level equal to the energy of the incident neutron minus the energy of the emitted neutron and the kinetic energy of recoil of the nucleus. The excited nucleus usually emits its excitation energy as one or more prompt gamma rays. The scattered neutrons, on the other hand, carry the remaining energy [45]. The illustration of neutron inelastic scattering is shown in Fig. 1.2 below

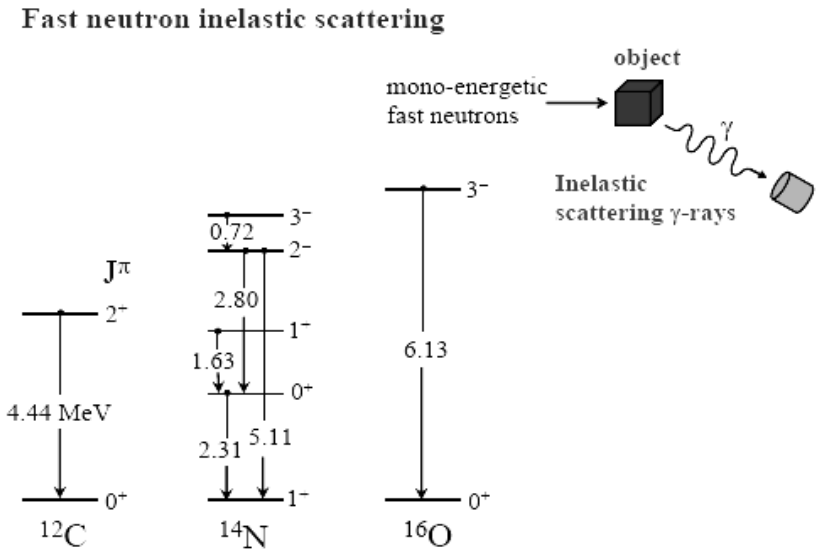

Figure 1.2: Schematic diagram illustrating inelastic scattering of neutrons from C, N and O gamma ray decay.

CHAPTER 2

MONTE CARLO STUDIES

In this study, the Monte Carlo calculations were carried out for Thermal Neutron Capture (TNC) and Neutron Inelastic Scattering (NIS)-based PGNAA setup shown in Figure 2.1 and Figure 2.3 respectively. This method basically obtains physical quantities by simulating the interactions of a large number of individual particles, and recording some of their properties. The average behavior of particles in the physical system is then inferred from the average behavior of the simulated particles. The procedure used are described in Appendix A.

2.1 Thermal Neutron Capture (TNC) Prompt Gamma Ray Yield Calculations

2.1.1 KFUPM 2.5 MeV TNC PGNAA Setup Description

The portable neutron generator-based PGNAA setup, as shown in Fig. 2.1, mainly consists of a cylindrical moderator made of high density polyethylene. The moderator has a central cylindrical cavity that can accommodate a cylindrical specimen with a maximum diameter of 9 cm and a length of 14 cm. A cylindrical 76 mm x 76 mm (diameter x length) $CeBr_3$ gamma-ray detector, with its longitudinal axis aligned along the moderator and sample's major axis, views the sample at a right angle to the neutron generator axis. The empty cylindrical 106 mm x 125 mm (diameter x height) polyethylene plastic sample container has a mass of 96 g with a density of 0.92 g/cm^3. Figure 2.1 shows the PGNAA setup with

the high-density polyethylene cylindrical moderator, portable neutron generator and the $CeBr_3$ detector. In order to prevent undesired gamma-rays and neutrons from reaching the detector, lead and paraffin shielding were provided around the gamma-ray detector.

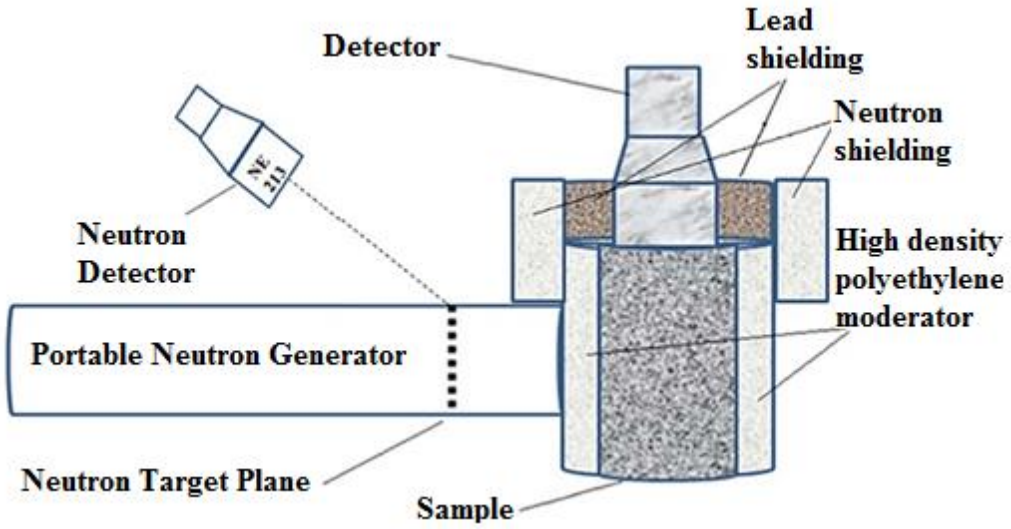

Figure 2.1: Schematic diagram of the portable neutron generator-based PGNAA setup.

The detector is shielded against thermal neutrons and gamma rays through neutron and lead shielding, respectively. Neutron shielding is made of paraffin and lithium carbonate mixed in equal weight proportions.

2.1.2 Gamma Ray Yield Calculations from B, Cd, Hg, Cr, and Ni-Contaminated Water Samples

The intensities of 368 keV mercury, 478 keV boron, 558 keV cadmium, (8483-8511, 8884, 9719) keV chromium and (8533,8998) keV nickel prompt gamma rays were calculated from water samples containing 0.75-2.5 wt. % mercury concentrations, 0.31-2.5 wt. % boron concentrations, 0.0625-0.500 wt. % cadmium concentrations, 2.9-15.7 wt. % chromium concentrations and 20.3-51.7 wt. % nickel concentrations using the general

purpose MCNP4B2 code [46]. The calculations were carried out for the 2.5 MeV neutrons–based PGNAA setup shown in Figure 2.1. The simulations were carried out for prompt gamma rays induced by 2.5 MeV neutrons thermalized in the high-density polyethylene moderator. For this simulation study, the sample was divided into sub-cells of 1 cm thickness. This allowed the transport of the neutrons and gamma rays of appropriate statistical weight to the next adjacent cell, without any loss. The prompt gamma ray intensity was then calculated in the detector volume using the F4 tally. Gamma ray yields were calculated for 368 keV mercury, 478 keV boron, 558 keV cadmium, (8483-8511, 8884, 9719) keV chromium and (8533,8998) keV nickel prompt gamma rays produced due to capture of thermal neutrons in mercury, boron, cadmium, chromium and nickel contaminated water samples. The thermal neutrons were produced through moderation of 2.5 MeV neutrons in the moderator. The calculated yield curves of mercury, boron, cadmium, chromium and nickel prompt gamma rays are plotted along with the experimental data in Fig. 4.36, 4.37, 4.38, 4.41 and 4.42 respectively.

2.1.3 Gamma Ray Yield Calculations from Chlorine-Contaminated Water Samples

The intensities of 517, 788, 1165, 1951, 2863, 6110, 6619, and 8578 keV chlorine prompt gamma rays were calculated from saline water samples containing 0.0-8.0 wt. % chlorine using the general purpose MCNP4B2 code [46]. Saline water samples were prepared by thoroughly mixing water with 0.0-8.0 wt. % chlorine.

Figures 2.2 shows the calculated yield of 517, 788, 1165, 1951, 2863, 6110, 6619 and 8578 keV prompt gamma rays as a function of chlorine concentration in the saline water samples.

As the chlorine concentration increases in the saline sample, the yield of the prompt gamma rays also increases but each gamma ray line has a different slope. The calculated yield curves will be compared with the experimental yields results later.

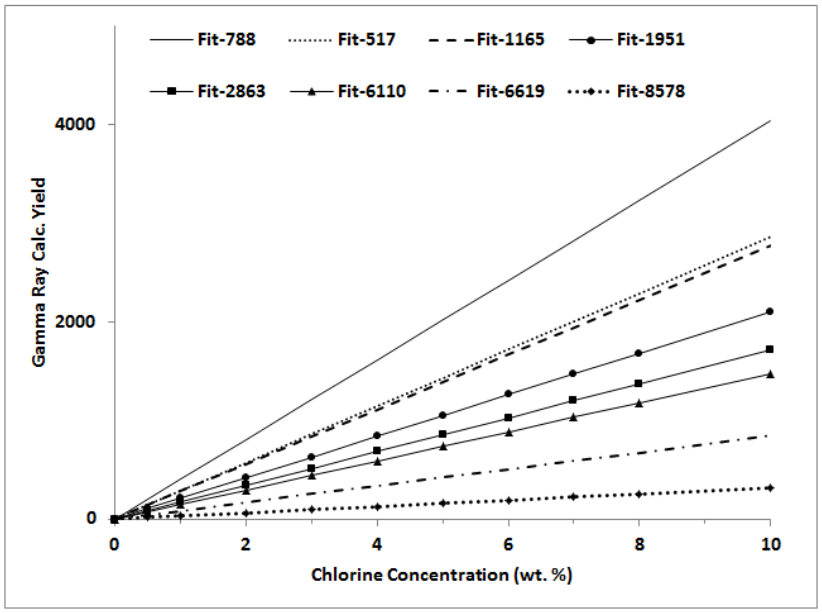

Figure 2.2: Shows the calculated yield of 517, 788, 1165, 1951, 2863, 6110, 6619 and 8578 keV prompt gamma rays as a function of 0-10 wt.% chlorine in the saline water samples.

2.2 Neutron Inelastic Scattering (NIS) Prompt Gamma Ray Yield Calculations

2.2.1 KFUPM 14 MeV NIS PGNAA Setup Description

The neutron inelastic scattering based PGNAA setup shown in Fig. 2.3. The setup mainly consists of a cylindrical polyethylene plastic sample container with 106 mm x 125 mm (diameter x height) dimensions. The sample container is placed at 0° angle with respect to the 14 MeV neutron beam and at a center- to-center distance of 70 mm from the 14 MeV neutron source. The neutron source was assumed to be point source. The empty polyethylene container has a mass of 96 g with a density of 0.92 g/cm^3. In the

simulation study, the plastic container was modeled thereby resulting in non-zero hydrogen gamma ray counts for zero-moisture concentration. The density of dry soil was taken as 1.69 g/cm^3 [49]. A cylindrical 76 mm x 76 mm (diameter x height) $LaBr_3$:Ce detector, placed at a center-to-center distance of 125 mm from the sample, detects the gamma rays from the sample at an angle of 90° with respect to the 14 MeV neutron beam axis. The detector was shielded against 14 MeV neutrons and gamma rays through tungsten and lead shielding, respectively. The fast neutron flux from the tritium target will be monitored using a cylindrical 76 mm x 76 mm (diameter x height) NE213 fast neutron detector, placed at a distance of 1.8 m from the target and making an angle of 130^o with respect to the beam.

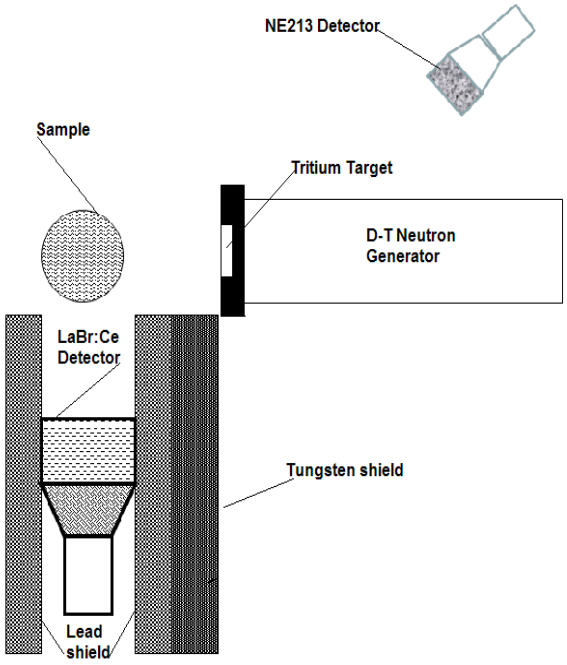

Figure 2.3: Schematic of 14 MeV neutron-based setup used for analysis of soil bulk samples.

2.2.2 Gamma Ray Yield Calculation from Moisture-Contaminated Soil Samples

The intensities of 1.78 MeV silicon, 6.13 MeV oxygen, and 2.22 MeV hydrogen prompt gamma rays were calculated from soil samples containing 0.0–15.0 wt% moisture using the general purpose MCNP4B2 code [46]. The calculations were carried out for the 14 MeV neutron-based PGNAA setup shown in Fig. 2.3. The procedure used in the present study was similar to the one described earlier [48, 49]. The simulations were carried out for prompt gamma rays induced by 14 MeV neutrons inelastic scattering in bulk soil samples.

For this simulation study, the sample was divided into sub-cells of 1 cm thickness. This allowed the transport of the neutrons and gamma rays of appropriate statistical weight to the next adjacent cell, without any loss.

In order to study prompt gamma ray production over the sample volume, 14 MeV neutrons as well as thermal neutron intensities were calculated over the sample diameter for 0–20% moisture concentrations using the F5 tally of a point detector. Fig. 2.4 shows the 14 MeV and thermal neutron intensity profiles over the sample diameter. The 14 MeV point source was located at x = -5.3 cm. The fast neutron data is shown with different symbols. The symbols are superimposed upon each other because the change in intensity of 14 MeV neutrons for various moisture concentrations is insignificant. The decrease in 14 MeV flux is mainly due to 1/distance^2 dependence of flux from the source. This is confirmed by the 1/distance^2 fit made to the 14 MeV neutron intensity data shown by the solid line. The calculated thermal neutron intensity

is plotted with symbols connected with solid lines. The thermal neutron intensity shows a dependence upon radial distance as well as moisture concentration. The thermal neutron intensity first increases with increasing radial distance from the source then reaches a maximum around the sample center and finally starts decreasing afterwards. The initial increase in thermal neutron intensity is due to increasing moderation of fast neutrons due to increasing moisture concentration.

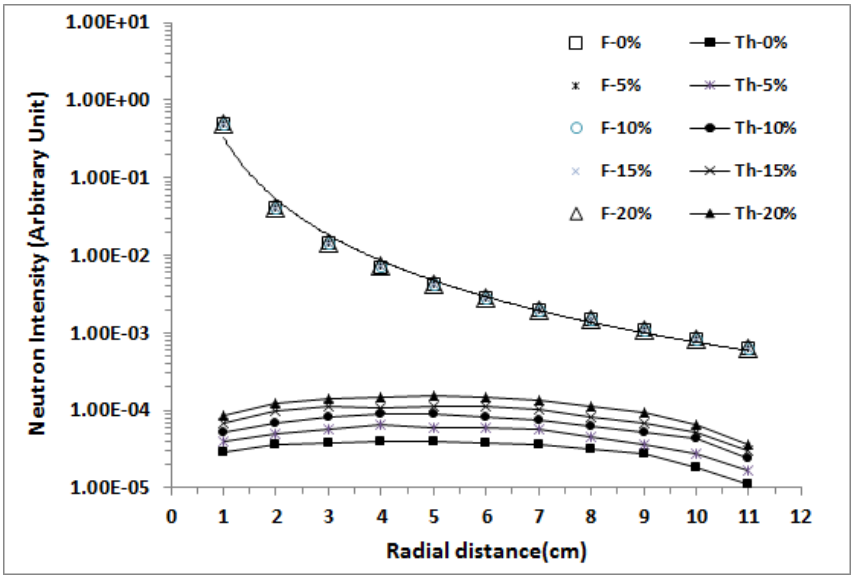

Figure 2.4: Calculated intensity profile of 14 MeV and thermal neutrons plotted over the sample diameter for 0–20% moisture concentration (wt%).

The decrease in thermal neutron intensity beyond the sample center is due to the loss of 14 MeV neutrons. Fig. 2.5 shows the thermal neutron intensity radial profile on an enlarged scale.

The location of maximum thermal neutron intensity is almost fixed around the center of sample diameter and is independent of moisture concentration. The thermal neutron intensity over the sample diameter increases with increasing moisture concentration.

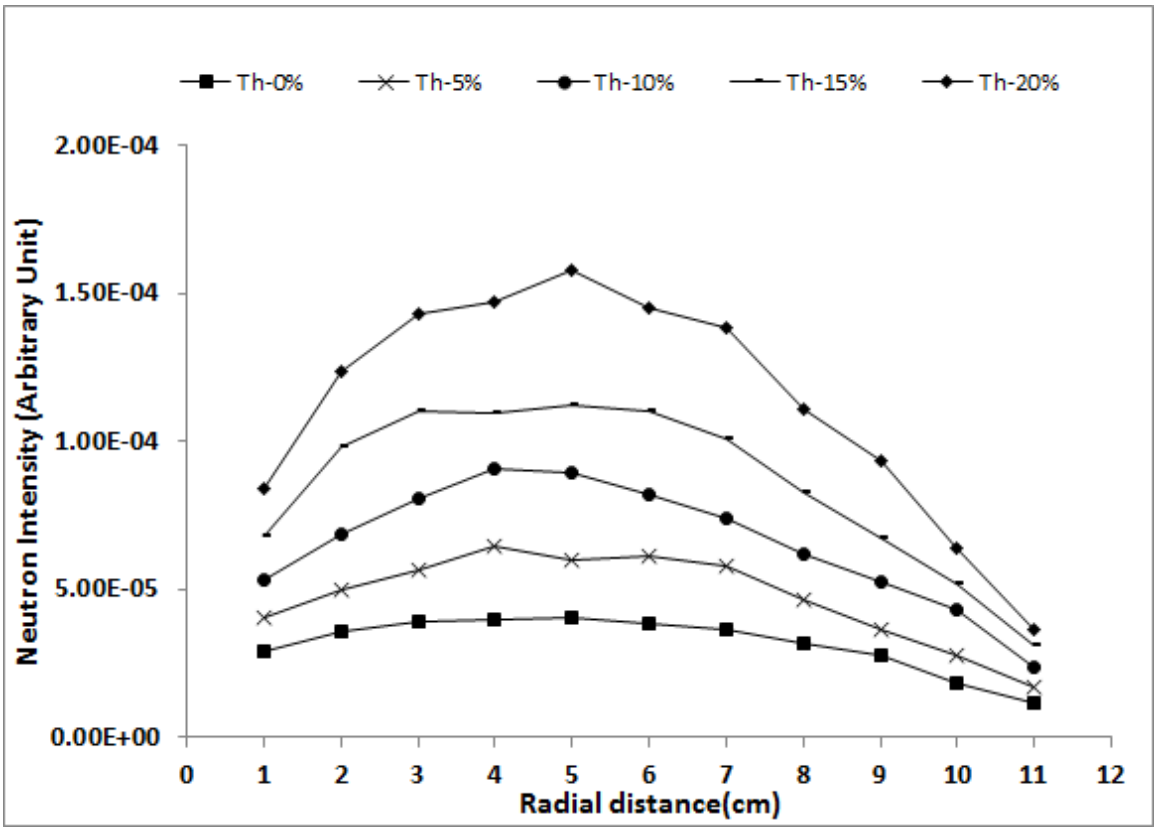

Figure 2.5: Calculated intensity profile thermal neutrons plotted over the sample diameter for 0–20% moisture concentration (wt%).

The prompt gamma ray intensity was then calculated in the detector volume using the F4 tally. The chemical composition of the soil sample used in the simulation is given in Table 2.1. There was no hydrocarbon contamination in the sample which may otherwise moderate the 14 MeV neutrons. Water was added to a soil sample with a predetermined mass, thereby increasing the total sample mass. The soil samples were thoroughly mixed with water to achieve 0.0–15.0 wt% moisture concentrations. Gamma ray intensities were calculated for 1.78 MeV silicon, 6.13 MeV oxygen, and 2.22 MeV hydrogen prompt gamma rays. The 2.22 MeV hydrogen gamma rays were produced due to capture of thermal neutrons in the hydrogen of the moisture in the sample. The thermal neutrons were produced due to moderation of 14 MeV neutrons in the sample.

Table 2.1: Chemical composition of dry soil sample used in the present study. [50]

Composition	Constituents (wt%)
SiO_2	88.01
Al_2O_3	2.99
Fe_2O_3	1.28
MgO	1.57
CaO	4.18
Na_2O	0.64
K_2O	0.85
TiO_2	0.48

In order to relate the variation in gamma ray intensity to change in thermal neutron flux due to added moisture, the thermal neutron and the hydrogen prompt gamma ray intensities were calculated inside the sample volume as a function of moisture concentration. Furthermore, the ratio of hydrogen gamma ray intensity to thermal neutron intensity was/ calculated. Fig. 2.6 shows the thermal neutron intensity as well as hydrogen gamma ray/ thermal neutron intensity ratio plotted as a function of moisture concentration. The hydrogen gamma ray/thermal neutron intensity ratio curve should reflect the variation of gamma ray intensity as a function of moisture concentration only, excluding the effect of thermal neutron flux. The gamma ray/thermal neutron intensity ratio curve initially exhibits a plateau over a smaller moisture concentration range of 0.0–8.0% and then starts showing a linear dependence upon moisture concentration over 8.0–20.0% range, as shown by the solid and dotted lines in Fig. 2.6.

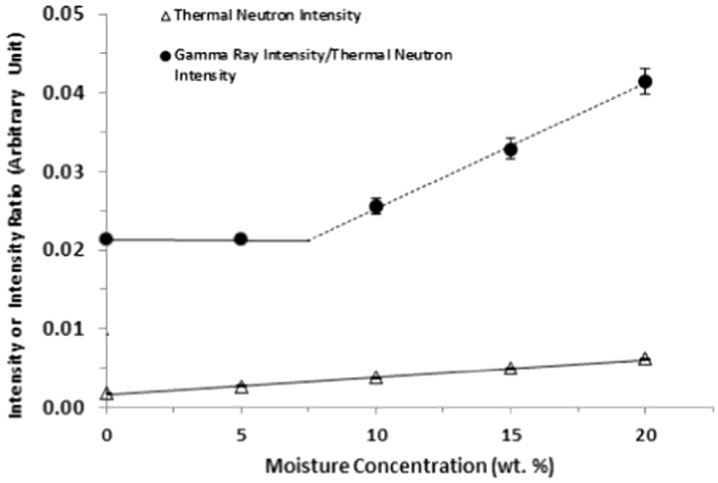

Figure 2.6: Calculated thermal neutron intensity as well as hydrogen gamma ray intensity/thermal neutron intensity ratio plotted as a function of moisture concentration (wt%).

Since both the thermal neutron flux as well as hydrogen gamma ray/thermal neutron intensity ratio shown in Fig. 2.6 exhibit a linear dependence upon moisture concentration beyond 8.0 wt%, it may be inferred that hydrogen gamma ray intensity will show a quadratic dependence upon moisture concentration beyond 8.0wt%.This is confirmed by linear correlation among hydrogen gamma ray intensity and square of moisture concentration (wt%) plotted in Fig. 2.7.

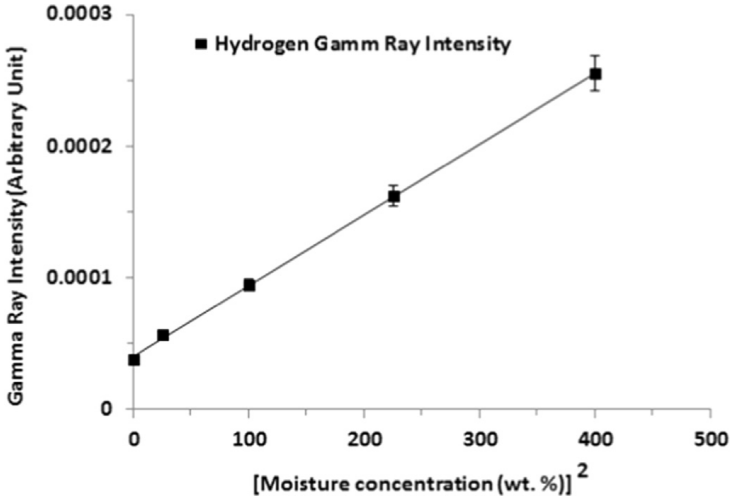

Figure 2.7: Calculated hydrogen gamma ray intensity plotted as a function of [moisture concentration (wt%)]^2.

Then, the intensities of 1.78 MeV silicon gamma ray and 6.13 MeV oxygen gamma rays were calculated as a function of moisture concentration in the soil samples. As the moisture concentration increases in the sample, the 14 MeV neutron flux decreases due to their increasing moderation in the sample. This results in decreasing intensities of the 1.78 MeV Si gamma rays and the 6.13 MeV O gamma rays with increasing moisture concentration in the soil sample, this explain the negative slope of the intensities of 1.78 MeV Si and 6.13 MeV O prompt gamma rays with respect to sample moisture concentration. Although moisture increase causes an increase in oxygen concentration in the sample, the decrease due to lower 14 MeV flux is more significant than the increase due to higher oxygen concentration, thereby resulting in a net decrease in intensity of 6.13 MeV O gamma rays.

The slope of the gamma ray intensity as a function of moisture concentration is higher for silicon gamma rays (1.78 MeV) as compared to those of oxygen gamma rays (6.13 MeV). This might be due to a higher attenuation of lower energy silicon gamma rays as compared to the higher energy oxygen gamma rays in increasing moisture concentration. The increasing moderation of 14 MeV neutrons with increasing moisture concentration increases the thermal neutron flux in the sample. This results in an increase in the intensity of 2.22 MeV hydrogen gamma rays from the soil sample. The 1.78 MeV Si prompt gamma rays and 2.22 MeV H prompt gamma rays have opposite trends in intensity variation with increasing moisture concentration in the soil sample. The results of these Monte Carlo calculations will be compared to the experimental results later.

2.2.3 Gamma Ray Yield Calculations from Benzene-Contaminated Soil Samples

The intensity variations of 1.78 MeV silicon, 4.44 MeV carbon, 6.13 MeV oxygen, and 2.22 MeV hydrogen prompt gamma rays were calculated from soil samples containing 0-10.4 wt. % benzene concentration using the general purpose MCNP4B2 code [46]. The calculations were carried for the 14 MeV neutron–based PGNAA setup shown in Figure 2.3. The procedure used in the present study was similar to the one described earlier in section 2.1.3.

The chemical composition of the soil samples used in the simulation is given in Table 2.1. The soil samples were thoroughly mixed with benzene to achieve 0-10.4 wt. % benzene concentrations. The gamma ray yields were calculated for 1.78 MeV silicon, 4.44 MeV carbon, 6.13 MeV oxygen, and 2.22 MeV hydrogen prompt gamma rays. The 2.22 MeV hydrogen gamma rays were produced due to capture of thermal neutrons in the hydrogen of the benzene in the sample. The thermal neutrons were produced due to moderation of 14 MeV neutrons in the sample.

Figures 2.8 shows the calculated yield of 1.78 MeV Silicon prompt gamma rays, 6.13 MeV Oxygen prompt gamma rays, 4.44 MeV Carbon prompt gamma rays and 2.22 MeV Hydrogen prompt gamma rays as a function of benzene concentration in the soil samples. As the benzene concentration increases in the sample, the 14 MeV neutrons flux decreases due to their increasing moderation in the sample. This results in decreasing intensities of the 1.78 MeV Si gamma rays and the 6.13 MeV O gamma rays with increasing benzene concentration in the soil sample. This is clearly shown in Fig. 2.8 with the negative slope of the yield of 1.78 MeV Si and 6.13 MeV O prompt gamma rays as a function of sample benzene concentration. An

increase in benzene concentration causes an increase in carbon concentration in the sample, thereby resulting in increase in intensity of 4.44 MeV C gamma ray, as shown in Figure 2.8. Although the increase in benzene concentration result in increases in hydrogen concentration in the sample but the increase in moderation of 14 MeV neutrons with increasing benzene concentration result in insignificant increases in the thermal neutron flux in the sample. This results in constant yield of 2.22 MeV H gamma rays from the soil sample as a function of benzene concentration, as shown in Figure 2.8. The 4.44 MeV C gamma ray has opposite trends in intensity variation with respect to 1.78 MeV Si and 6.13 MeV O prompt gamma rays with increasing benzene concentration in the soil sample.

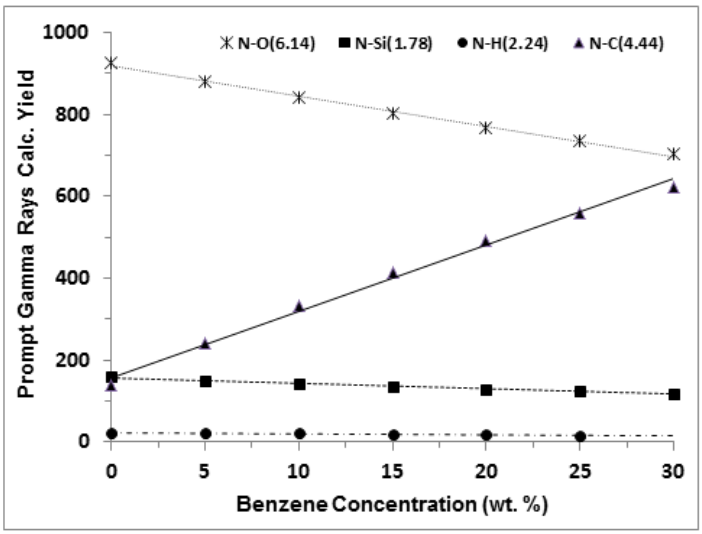

Figure 2.8: Calculated yield of 1.78 MeV Si, 4.44 MeV C, 2.22 MeV H and 6.13 MeV O prompt gamma rays from soil sample as a function of benzene contents in soil sample.

Figure 2.9 shows results of similar calculations related to the effect of moisture on prompt gamma yields of 1.78 MeV Si, 6.13 MeV O and 2.22 MeV H gamma rays from soil sample containing 5.1, 7.4, 9.7, 11.9 and 14.0 wt. % water reported earlier [49].

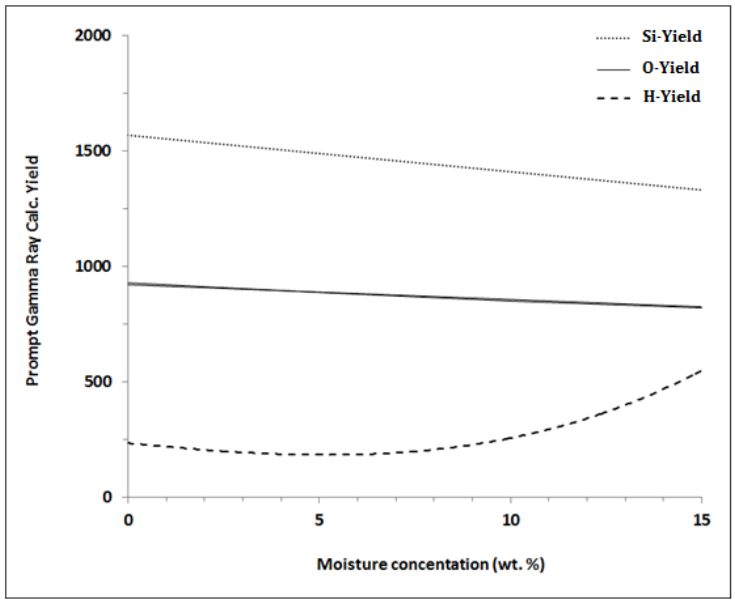

Figure 2.9: Calculated yield of 1.78 MeV Si, 2.22 MeV H and 6.13 MeV O prompt gamma rays from soil sample as a function of moisture contents in soil sample.

The trends of to 1.78 MeV Si and 6.13 MeV O prompt gamma rays with increasing benzene observed in this study agrees with the moisture study. However, yield of 2.22 MeV H gamma rays as a function of moisture concentration shows initial almost constant intensity up till 8.0 wt.% moisture. Since benzene has 13 % less hydrogen concentration, in case of benzene this constant yield of 2.22 MeV H gamma ray been observed uptill around 10.4 wt %, which is in agreement with moisture study [49].

CHAPTER 3

ENERGY RESOLUTION MEASUREMENTS OF $CeBr_3$ and $LaBr_3$:Ce DETECTORS

In this study, performance tests of the $CeBr_3$ and $LaBr_3$:Ce detectors were carried out. In order to obtain the maximum yield of detected gamma rays, the performance of a large cylindrical 100 mm x 100 mm $LaBr_3$:Ce and 76 mm x 76 mm (height x diameter) cerium tribromide ($CeBr_3$) detectors were tested for gamma rays produced through radio-isotope sources as well as from thermal neutron capture in contaminated water samples and detector's materials using a portable Deuterium-Deuterium reaction neutron generator-based prompt gamma ray neutron activation analysis (PGNAA) setup. Finally the energy resolution of the $CeBr_3$ and $LaBr_3$:Ce detectors were calculated for the well resolved gamma rays.

3.1 Experimental Setup

The performance tests of the $CeBr_3$ and $LaBr_3$:Ce detectors were carried out using the portable neutron generator based PGNAA setup described previously.

The samples were filled in cylindrical plastic bottles of 14 cm length and 9 cm internal diameter. They were then irradiated using a pulsed beam of 2.5 MeV neutrons with 70 keV voltage and a current of 70 μA. The prompt gamma-ray data from the samples was acquired for 25 min.

Detectors signals were acquired using standard NIM electronics modules as shown in Figure 3.1. For each detector, the signal that was routed through a preamplifier and was processed through a spectroscopy amplifier with shaping time of 1 μs. A Logical gate signal was generated for each signal processed by the amplifier using single channel analyzer and gate and delay generator modules. For dead time correction, one of the outputs of the gate and delay generator was used to gate the Multichannel Buffer, while another output was used to calculate the dead time correction.

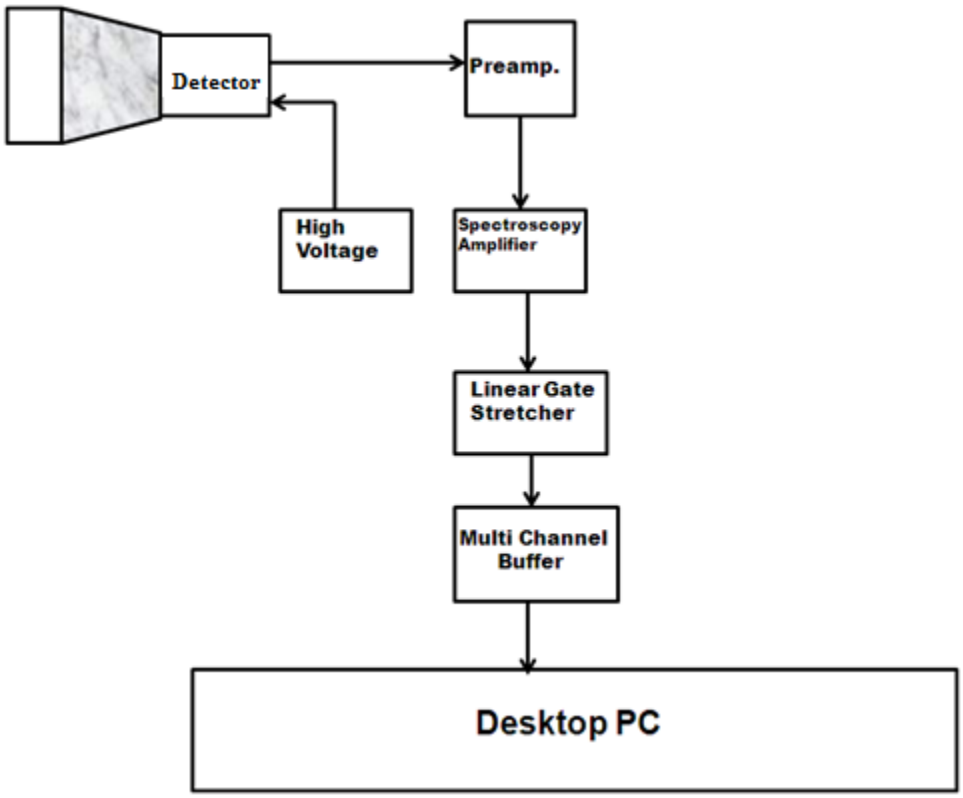

Figure 3.1: Electronic Configuration Diagram

Dead time correction (DTC) was calculated to be less than 1% at the end of each experimental run from the integrated counts in the stored spectrum N_{tot} and total gate signals N_{gates}, counted independently through the relation [4, 51, 52]

$$DTC = \frac{Ngates - Ntot}{Ngates} \qquad (3.0)$$

The dead time corrected counts under a peak $Y_{DTC-Corr}$ were then obtained from the experimental counts under the peak Y_{exp} using the relation:

$$Y_{DTC-Corr} = Y_{exp}(1 + DTC) \qquad (3.1)$$

The dead time correction depends upon the sample as can be seen in the following section.

3.2 Energy Resolution Measurements of $LaBr_3$:Ce Scintillation Detector

In this part of the study, the energy resolution of the $LaBr_3$:Ce detector was measured for prompt capture gamma ray peaks from chromium, nickel, mercury, boron and cadmium-contaminated water samples along with captured gamma rays from the detector materials and radioisotope sources. For each run the data was taken for 20 minutes. For capture gamma ray production, the procedure described earlier in section 3.1 was used. For radioisotope sources measurement only the source was placed in the sample cavity. The energy resolution of the large $LaBr_3$:Ce detector was measured for 662 keV gamma-rays from ^{137}Cs source. The pulse height spectrum of the large detector from ^{137}Cs source is shown in Fig. 3.2. For 662 keV gamma-rays, the energy resolution of the detector was measured to be 5.8%. This is 9% higher than the manufacturer's warranted energy resolution (5.3%) of the detector.

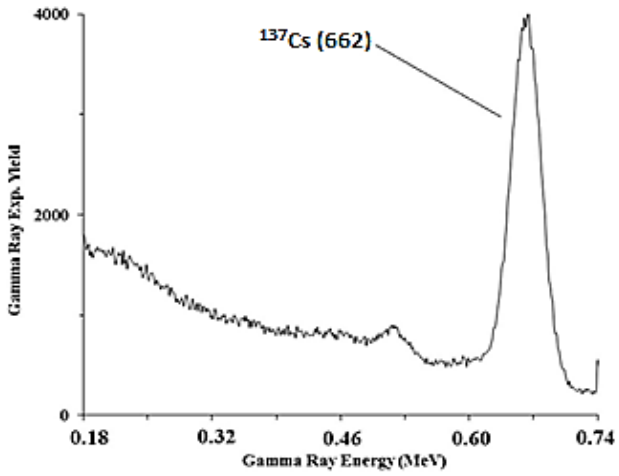

Figure 3.2: $LaBr_3$:Ce pulse height spectrum taken with ^{137}Cs source exhibiting 662 keV peak.

3.2.1 Measurement of the $LaBr_3$:Ce detector intrinsic activity

The $LaBr_3$:Ce detector (with 100 mm x 100 mm $LaBr_3$:Ce crystal, coupled to a fast photomultiplier model number R4144) was supplied to us by the manufacturer Saint Gobain, France, as a single unit along with a matching voltage divider. The detector was operated at negative 994 V voltage. The detector body has a common ground connection with dynode and timing output with grounded-anode configuration of the photomultiplier. The detector time resolution warranted by the manufacturer for 511 keV gamma rays was 608 ps. In the present study, the time resolution of the 100 mm x 100 mm detector was not measured. The manufacturer quoted time resolution of our detector is better than the time resolution for a 89 mm x 203 mm $LaBr_3$:Ce detector reported earlier [53]. The energy resolution of the 100 mm x 100 mm $LaBr_3$:Ce detector quoted by the manufacturer for 661 keV gamma rays was 5.3%.

The intrinsic activity of the 100 mm x 100 mm detector was determined using the procedure described for the smaller 76 mm x 76 mm $LaCl_3$:Ce [54, 55] and $LaBr_3$:Ce detectors [4]. The activity/second was determined from the area under the 1468 keV peak of the detector as shown in Fig. 3.3. The lack of a bend on the lower slope of the 1468 keV peak in this spectrum (as observed in other smaller sizes $LaBr_3$:Ce detectors) is due to poorer energy resolution of the detector caused by the coupled fast photomultiplier with poorer energy resolution. The detector activity was measured for 101sec and was found to be 142±1 counts/s. The photopeak efficiency (PE) of the large detector was calculated from the ratio of the measured activity count rate (142±1 counts/s) and the calculated activity of 775 Bq for a 100 mm x 100 mm $LaBr_3$ detector. The PE of the large detector was found to be 0.183. The activity of the 100 mm x 100 mm LaBr detector was calculated from extrapolation of [56] data for smaller sizes $LaBr_3$:Ce detectors to 100 x 100 mm^2 $LaBr_3$ detector. For smaller cylindrical $LaBr_3$:Ce detectors of 38 mm x 38 mm, 41 mm x 76 mm, and 51 mm x 76 mm sizes (diameter x height), Menge et al. reported calculated activity of the detector for 1436+32 keV as 42.6 Bq, 99.0 Bq, and 153 Bq, respectively. They also reported photopeak count rates (count/s) for expected/measured count rates for theses detectors as (3.32/3.55), (10.7/10.6) and (21.1/21.8), respectively. From the ratio of measured count rate and calculated activity, the photopeak efficiency was derived [56]. Previously, the PE of the 76 mm x 76 mm $LaBr_3$:Ce and LaCl3:Ce detectors were reported to be 0.191 [54] and 0.16 [55], respectively.

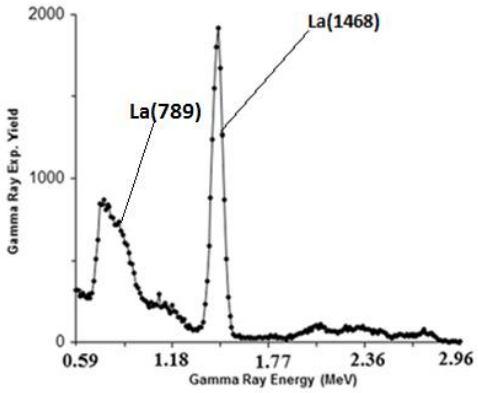

Figure 3.3: 100 mm x 100 mm LaBr3:C detector intrinsic activity pulse height spectrum exhibiting 1468 keV line from lanthanum.

3.2.2 Measurement of $LaBr_3$:Ce detector activation spectrum

The detector activation spectrum was produced due to the interaction of thermal neutrons with the detector material. The activation spectrum also contains gamma ray peaks due to room background. The energies of the gamma-rays are listed in Table 3.1 [57].

Fig. 3.4 shows a gamma ray spectrum of the large $LaBr_3$:Ce detector over 0.11 to 0.84 MeV energy range exhibiting prominent gamma-ray peaks of lanthanum, cerium, and bromine from the detector material.

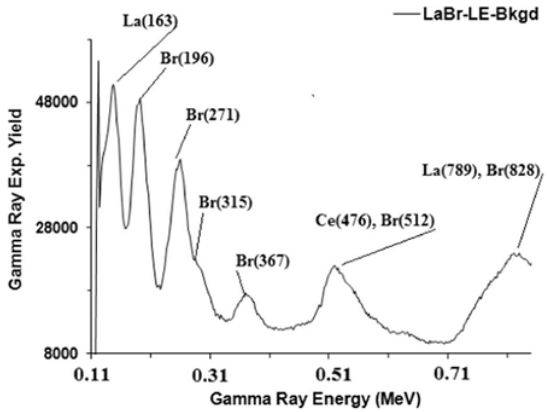

Figure 3.4: Prompt gamma-ray spectrum due to activation of the 100 mm x 100 mm LaBr3:Ce detector caused by capture of thermal neutrons in La, Br and Ce elements present in LaBr3:Ce detector.

Fig. 3.4 shows the lanthanum peaks at 163 and 789 keV along with the bromine peaks at 196, 276, 315, 367, and 512 keV. The Ce peak at 476 keV could not be resolved from the Br peak at 512 keV and from the La peaks at 567 and 595 keV. Also, the La peak at 789 keV could not be resolved from the Br peak at 828 keV. The detector energy resolution can be calculated from the activation spectrum for well resolved peaks of significant intensities.

For comparison, the activation spectrum of a smaller 76 mm x 76 mm $LaBr_3$:Ce detector [4] is shown in Fig. 3.5 over 0.05 to 2.55 MeV range. The energy resolution of the large detector is poorer as compared to that of the 76 mm x 76 mm $LaBr_3$:Ce detector and many peaks could not be resolved from adjacent ones.

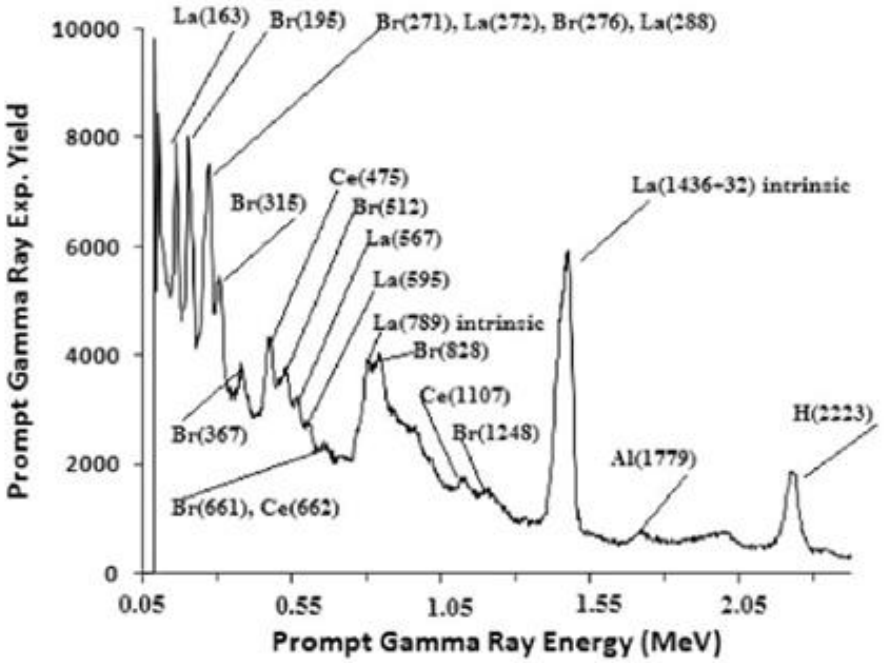

Figure 3.5: Prompt gamma-ray spectrum due to activation of the 76 mm x 76 mm LaBr3: Ce detector caused by capture of thermal neutrons in La, Br and Ce elements present in the LaBr3:Ce detector [4].

Table 3.1: Energies and partial elemental cross section $\sigma_\gamma^z(E_\gamma)$-barns of prominent capture gamma-rays used in this study [57].

Element	Gamma-ray energy (keV)	$\sigma_\gamma^z(E_\gamma)$-barns	Element	Gamma-ray energy (keV)	$\sigma_\gamma^z(E_\gamma)$-barns
B	478	716	Al	1623	0.0099
Cl	517	7.58	Cd	171	57
	786	3.42		245	274
	788	5.42		558	1860
	1164	8.90		651	359
	1601	1.21	Ce	475	0.082
	1951	6.33		662	0.241
	1959	4.10		737	0.026
	2863	1.82		1107	0.040
	3061	1.13	Hg	368	251
	4980	1.23		5967	62.5
	5715	1.82	H	2223	0.333
	6110	6.59	Ni	8533	0.721
	6619	2.53		8998	1.49
	6628	1.47	Br	196	0.434
	7414	3.29		245	0.80
	7790	2.66		271	0.462
	8578	0.88		275	0.158
Cr	7099	0.146		288	0.253
	7938	0.424		315	0.460
	8483	0.169		367	0.233
	8511	0.233		389	0.049
	8884	0.780		469	0.290
	9719	0.260		512	0.210
La	163	0.489		542	0.114
	272	0.502		554	0.838
	288	0.73		616	0.39
	567	0.335		619	0.515
	595	0.103		661	0.082
	789	Intrinsic		690	0.083
	1436±32	Intrinsic		776	0.990
	2521	0.212		828	0.285
	5126	0.114		1044	0.323
				1248	0.0527
				1317	0.314
				1475	0.193
				7577	0.108

3.2.3 B, Cd, Hg, Cr and Ni Contaminated Water Sample Data

The energy resolution of the $LaBr_3$:Ce detector was measured for capture gamma rays from B, Cd, Hg, Cr and Ni-contaminated water samples. The spectra of the large detector were recorded over 0.3 to 10 MeV gamma-ray energies. The detector spectra were acquired with two different energy ranges. The gamma-ray spectra from mercury, boron and cadmium were acquired over 0.09 to 0.61 MeV energy range with data acquisition time listed separately for each sample in Table 3.2. The gamma-ray spectra from chromium, mercury, and nickel were acquired over 1.33–10.0 MeV energy range. The mercury, boron, cadmium, chromium and nickel samples were prepared by dissolving various chemical compounds, such as boric acid, cadmium acetate, mercuric nitrate, chromium trioxide and nickel nitrate, in water and filling them in the 90 mm diameter x 140 mm long plastic (PET) bottles.

Table 3.2: Chemical composition and concentration of various elements samples used in the present study.

Chemical compound	Element	Concentration (wt%)	Measurement time (s)
Boric acid H_3BO_3	B	2.5	720
Cadmium acetate $Cd(CH_3CO_2)_2$	Cd	0.25	480
Mercuric nitrate $Hg(NO_{3)2}$	Hg	3.1	1600
Nickel nitrate $Ni(NO_3)_2$	Ni	22	4600
Chromium trioxide CrO_3	Cr	52	6400

These samples were supplied by the Department of Chemistry, King Fahd University of Petroleum and Minerals, Saudi Arabia. The concentrations of the various elements along with corresponding sample measurement times are listed in Table 3.2. The samples' measurement times vary from 480 s to 6400 s.

Figs. 3.6, 3.7 and 3.8 show the detector pulse height spectra over 0.09 to 0.61 MeV gamma-rays from the mercury, boron and cadmium samples superimposed upon background spectra while Figs. 3.9, 3.10 and 3.11 show their respective background-subtracted peaks.

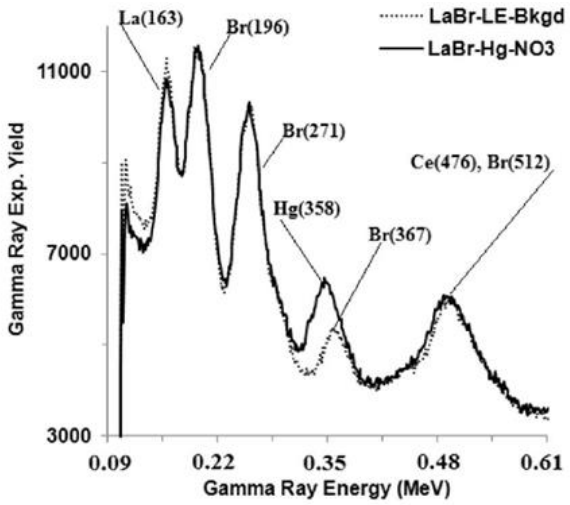

Figure 3.6: Prompt gamma-rays pulse height spectra of mercuric nitrate contaminated water sample superimposed upon background spectrum.

In order to superimpose the sample spectra upon the background spectra, both sample and background spectra were normalized to the same counting time and same neutron flux. This was obtained by normalizing both sample and background spectra in the region where background is constant (sample independent). Then, the background spectrum was subtracted from normalized spectrum to generate the difference spectrum.

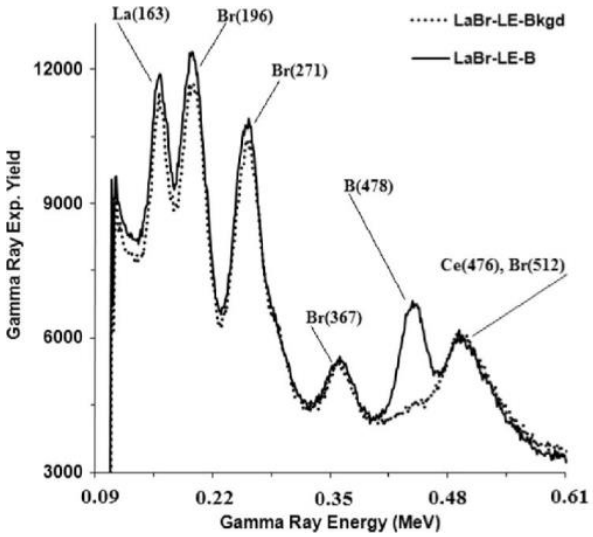

Figure 3.7: Prompt gamma-rays pulse height spectra of boric acid contaminated water sample superimposed upon background spectrum.

Figs. 3.12 and 3.14 show detector pulse height spectra over 1.33– 10.0 MeV gamma-rays from the chromium and nickel samples while Fig. 3.16 shows the detector pulse height spectrum over 0.54– 9.42 MeV gamma rays from the mercury sample. Figs. 3.13, 3.15 and 3.17 are subsections of Figs. 3.12, 3.14 and 3.16 showing enlarged plots of chromium, nickel and mercury peaks.

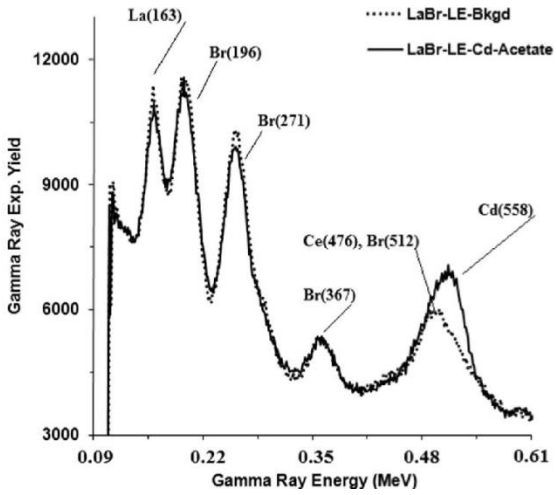

Figure 3.8: Prompt gamma-rays pulse height spectra of cadmium-acetate contaminated water sample superimposed upon background spectrum.

Fig. 3.6 shows the spectrum of mercury-contaminated water samples superimposed upon the background spectrum over 0.09 to 0.61 MeV. The mercury peak at 358 keV interferes with the bromine peak at 367 keV from the detector background. Fig. 3.9 shows the well resolved 358 keV mercury peak in the difference spectrum, obtained after subtracting background from mercury sample spectrum.

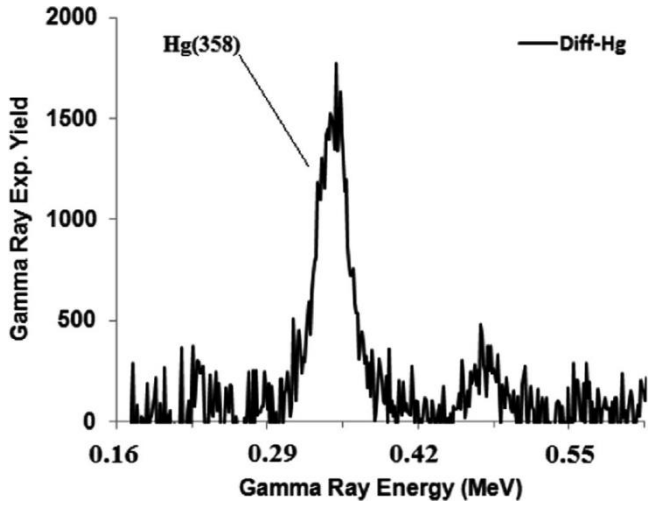

Figure 3.9: Difference pulse height spectra of mercuric nitrate contaminated water sample exhibiting 358 keV mercury peak.

Similarly, Fig. 3.7 shows the boron contaminated water sample spectrum superimposed upon background spectrum. The boron peak at 478 keV is interfering with cerium and bromine peaks at 476 and 512 keV, respectively. Fig. 3.10 shows the well resolved 478 keV boron peak in the difference spectrum, obtained after subtracting background from boron spectrum. The cadmium spectra acquired by the large detector are shown in Figs. 3.8 and 3.11. As shown in Fig. 3.8, the cadmium peak at 558 keV interferes with the cerium and bromine peaks at 476 and 512 keV, respectively. Fig. 3.11 shows the well resolved 558 keV cadmium peak in the difference spectrum, obtained after subtracting background spectrum from cadmium spectrum.

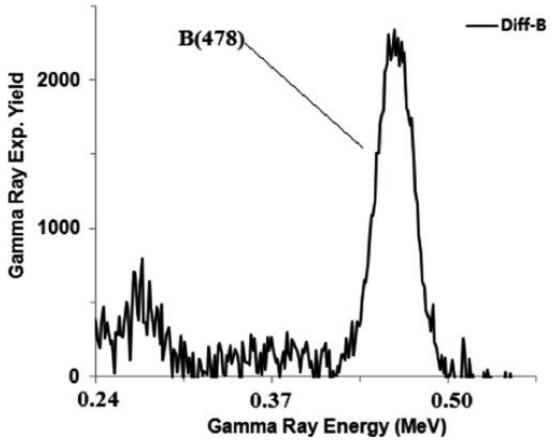

Figure 3.10: Difference pulse height spectra of boric acid contaminated water sample exhibiting 478 keV boron peak.

Fig. 3.12 shows the spectrum of chromium-contaminated water sample superimposed upon the background spectrum over 1.33 to 10.0 MeV. The chromium peaks at 7099, 7938, 8884 and 9719 keV appear at the end of the spectrum. Also shown in Fig. 3.12, is the hydrogen capture peak at 2223 keV due to capture of thermal neutrons in the high density polyethylene.

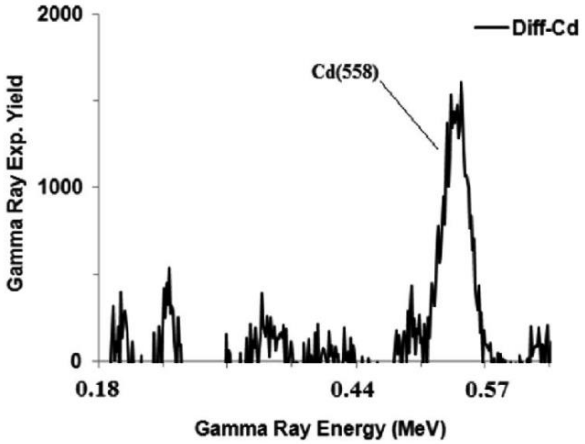

Figure 3.11: Difference pulse height spectra of cadmium-acetate contaminated water sample exhibiting 558 keV cadmium peak.

The lanthanum and bromine peaks from thermal neutron capture in the detector material appear at 5126 and 7577 keV, respectively. Fig. 3.13 shows the enlarged part of Fig. 3.12 over 7.28–10.0 MeV exhibiting the chromium peaks at 7099, 7938, 8884 and 9719 keV, along with the background spectrum.

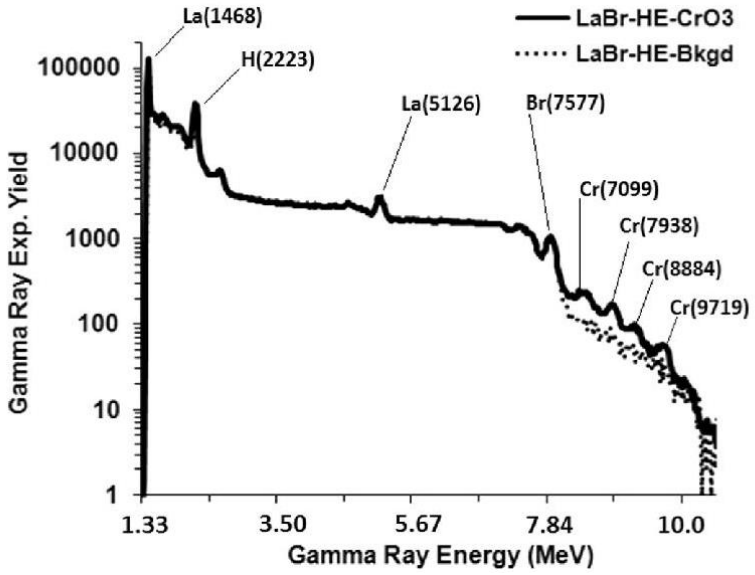

Figure 3.12: Prompt gamma-rays pulse height spectra of chromium trioxide (CrO3) contaminated water sample superimposed upon background spectrum.

Similarly, Fig. 3.14 shows the spectra of nickel-contaminated water samples superimposed upon background spectrum over 1.33–10.0 MeV. The nickel peaks at 8533 and 8998 keV appear at the end of the spectrum.

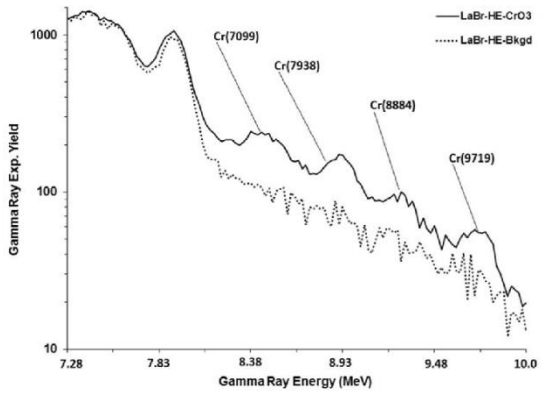

Figure 3.13: Enlarged pulse height spectrum of chromium trioxide contaminated water sample exhibiting 7099, 7938, 8884 and 9719 keV chromium peaks superimposed upon background spectrum.

Fig. 3.15 shows the enlarged part of Fig. 3.14 over 6.77 to 10.0 MeV exhibiting the nickel peaks at 8533 and 8998 keV along with the single escape peak superimposed upon the background spectrum. The high energy gamma-ray spectrum of mercury-contaminated water sample, superimposed upon background spectrum, is shown in Fig. 3.16 over 0.54 to 10.0 MeV. The mercury peak could be seen at 5967 keV energy. The 5967 keV mercury peak along with its associated single escape peak, superimposed upon the background, is shown on an enlarged scale in Fig. 3.17.

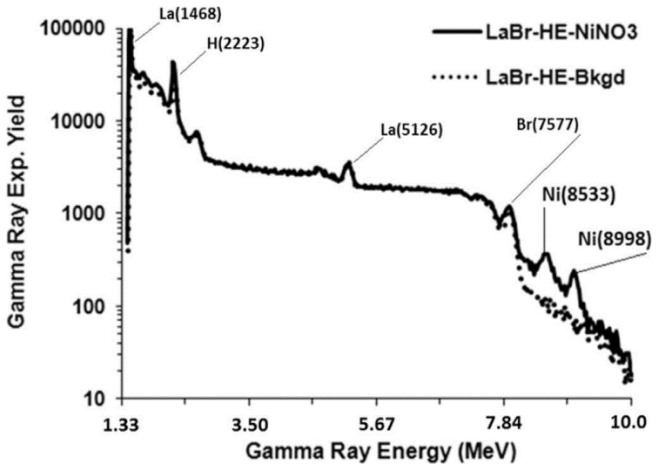

Figure 3.14: Prompt gamma-rays pulse height spectra of nickel nitrate (NINO3) contaminated water sample superimposed upon background spectrum.

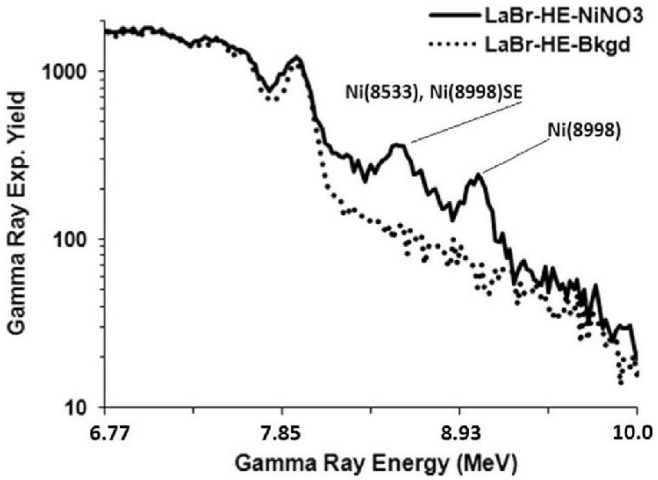

Figure 3.15: Enlarged pulse height spectrum of nickel nitrate contaminated water sample exhibiting 8533 and 8998 keV nickel peaks superimposed upon background spectrum.

The gamma ray peaks data from the detector material, as well as from boron, cadmium, mercury, chromium and nickel samples was fitted to determine the energy resolution (FWHM) of the detector using the least squares fit method. In order to investigate the effect of light collection from the $LaBr_3$:Ce crystal, the energy resolution (%) was plotted against$1/\sqrt{E_\gamma}$ in Figure 3.18.

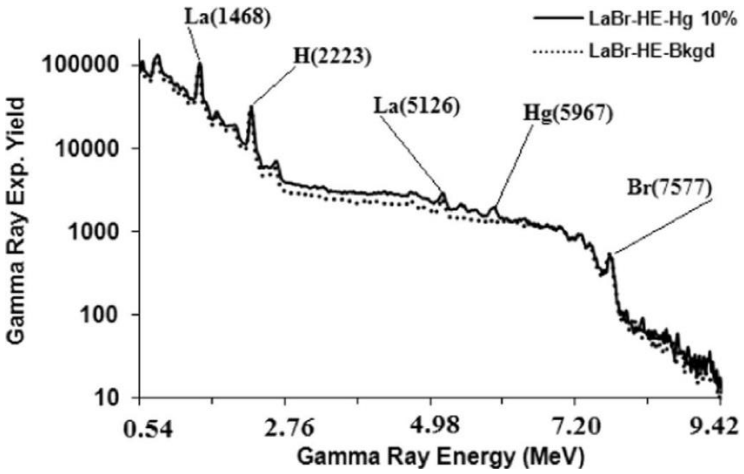

Figure 3.16: Prompt gamma-rays pulse height spectra of mercuric nitrate (HgNO3) contaminated water sample superimposed upon background spectrum.

The slope of the fit is indicative of the light collection of the detector assembly. For comparison, the energy resolution data of an 89 mm x 203 mm $LaBr_3$:Ce detector coupled to a photomultiplier with good energy resolution [53, 58], was also plotted against $1/\sqrt{E_\gamma}$.

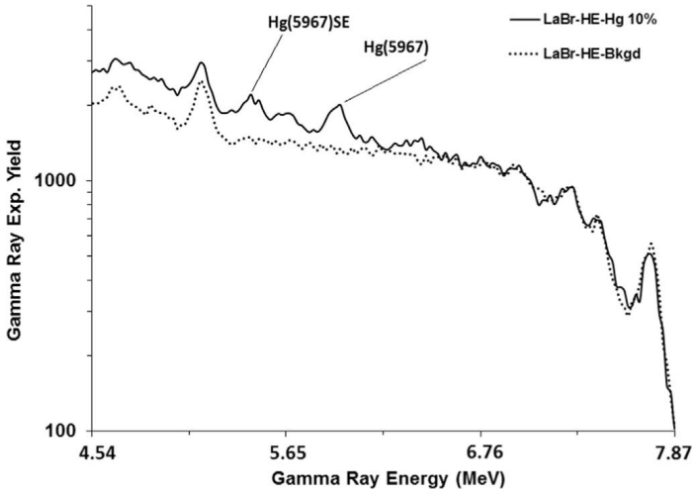

Figure 3.17: Enlarged pulse height spectrum of mercuric nitrate contaminated water sample exhibiting 5967 keV mercury peak superimposed upon background spectrum.

Since both detectors contains 5% Ce each, the only difference between them is more efficient light collection in the 89 mm x 203 mm $LaBr_3$:Ce detector [53, 58].

Figure 3.18 shows the energy resolution data of the 89 mm x 203 mm $LaBr_3$:Ce and 100 x 100 mm^2 $LaBr_3$:Ce detector plotted as a function of $1/\sqrt{E_\gamma}$. The solid line through the data represents linear least squares fit to the data of the type:

$$\Delta E/E(\%) = a/(\sqrt{E_\gamma}) + b.$$

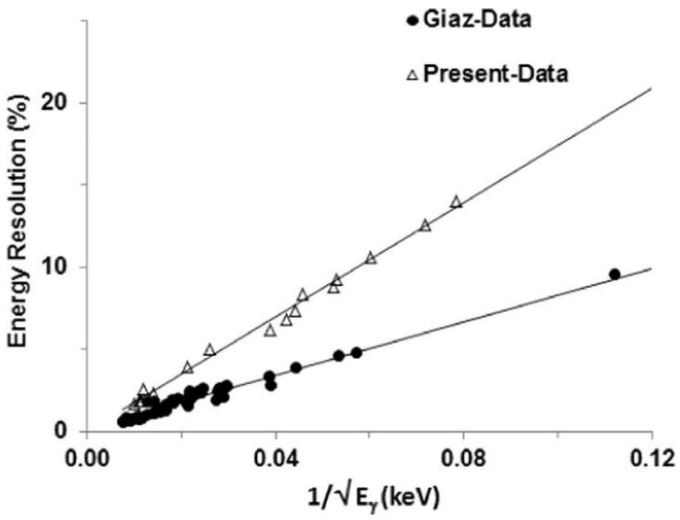

Figure 3.18: Energy resolution (%) of the 100 mm x 100 mm LaBr3:Ce detector and 89 mm x 203 mm LaBr3:Ce detector [53, 58] plotted as a function of 1/√Eγ.

The values of the coefficients a and b of the fit to both detectors' energy resolution data are listed in Table 3.3. The slope of the curve for 100 mm x 100 mm detector was calculated to be 174.4 while for the 89 mm x 203 mm $LaBr_3$:Ce detector its value was 80.9. The almost two times smaller value of the slope for the 89 mm x 203 mm $LaBr_3$:Ce detector indicates almost two times better light collection for 89 mm x 203 mm $LaBr_3$:Ce detector. This is due to the fact that the photomultiplier used in the 100 x 100 mm^2 $LaBr_3$:Ce detector has poorer energy resolution but superior timing resolution. The manufacturer claimed an excellent time resolution of 608 ps for the 100 x 100 mm^2 $LaBr_3$:Ce detector as compared to 880 ps reported for the 89 mm x 203 mm $LaBr_3$:Ce detector.

Table 3.3: Coefficient of fit to energy resolution data of 100 mm x 100 mm and 89 mm x 203 mm $LaBr_3$:Ce detector [53,58]. Fitted equation: ΔE/E(%) = a/(√Eg) + b.

Detector size	Fit coefficient	
	Coefficient a	Coefficient b
100 mm x 100 mm	174.4	0.011
89 mm x 203 mm	80.9	0.224

3.3 Energy Resolution Measurements of $CeBr_3$ and $LaCl_3$: Ce Detectors

In this study, the $CeBr_3$ and $LaCl_3$: Ce Detectors energy resolution were measured from gamma ray produced through thermal neutron capture in $CeBr_3$ and $LaCl_3$: Ce Detector's material as well as radiative gamma ray sources using MP320 portable deuterium-deuterium neutron generator based prompt gamma ray neutron activation analysis (PGNAA) setup.

3.3.1 Intrinsic Activity Spectra of $CeBr_3$ and $LaCl_3$: Ce Detectors

Ideally $CeBr_3$ detector should be free of intrinsic activity because Ce and Br are both non-radioactive but it has intrinsic activity due to of ^{227}Ac impurity in the detector material. The intrinsic activity the of $CeBr_3$ detector was measured following the procedure used previously for intrinsic activity measurements of $LaCl_3$:Ce detectors [54] and $LaBr_3$:Ce detector [55]. Detector intrinsic activity was measured when it was installed in the PGNAA setup without any additional low background chamber to isolate detector intrinsic activity from room background. For the sake of continuity, it will be briefly described here. The detector signal, which was routed through a preamplifier, was processed through a spectroscopy amplifier with shaping time of 1 microsecond. The amplifier signal was processed by a Multichannel Buffer (ADC) for subsequent storage in a personal computer. Fig. 3.19 shows intrinsic activity spectrum of the $CeBr_3$ detector in units of counts/s/cm^3 as a function of gamma ray energy, which was used to calculate intrinsic activity rate per unit volume of the $CeBr_3$ detector.

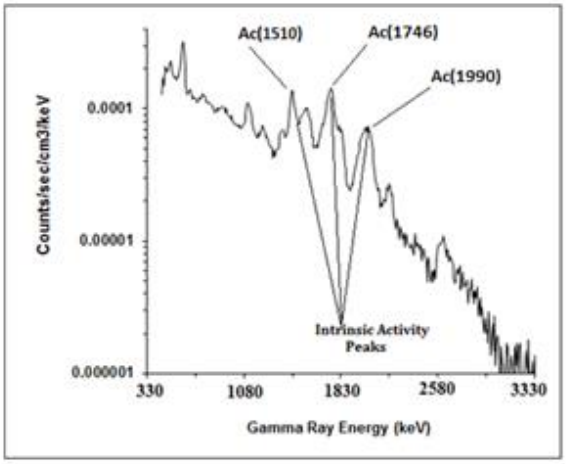

Figure 3.19: CeBr3 detector intrinsic activity spectrum in units of counts/s/cm3 as a function of gamma ray energy.

Fig. 3.19 also shows three prominent peaks of intrinsic activity of due to radioactive decay of ^{227}Ac impurity contaminants corresponding to 1510, 1746 and 1990 keV [59].

In the present study, the $CeBr_3$ detector intrinsic activity was measured over two different energy ranges namely; total intrinsic activity was measured over 0.33 to 3.33 MeV energy range (called total intrinsic activity in the following paragraphs) while ^{227}Ac activity (called partial ^{227}Ac activity in the following paragraphs) was measured over 1.20-2.20 MeV range. The total activity of the $CeBr_3$ detector was measured to be 0.022±0.001 counts/s/cm^3 and while partial ^{227}Ac activity was measured to be 0.007±0.001 counts/s/cm$^{3.}$ Previously intrinsic activity of two smaller 50 mm x 50 mm cylindrical $CeBr_3$ detectors namely detector # SBX 431 and detector # SFB 308 has been measured [59]. Figure 3.20 shows detector intrinsic activity pulse height spectrum superimposed upon detector energy calibration spectrum taken with a ^{207}Bi gamma ray source.

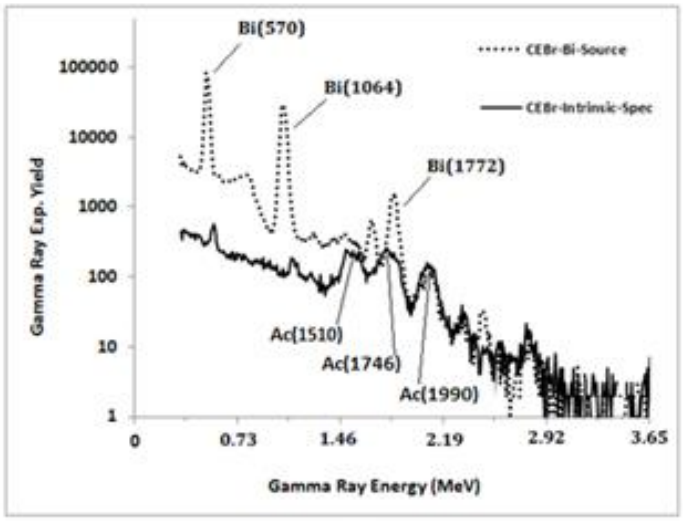

Figure 3.20: CeBr3 detector intrinsic activity spectrum superimposed upon 207Bi source spectrum plotted as a function of gamma ray energy.

The detector intrinsic activity spectrum without ^{207}Bi source, shows low gamma ray background below 1.4 MeV energy. The gamma ray intrinsic activity spectrum of the detector over 1200-2200 keV energy range is due to gamma rays emitted by alpha emitter contaminants of ^{227}Ac impurity produced by alpha particles of energies 5716 keV (^{223}Ra); 6000 keV (^{227}Th) **;** 6623 keV (^{211}Bi) ; 6819 keV (^{219}Rn) ; 7386 keV (^{215}Po) [59].

For the SBX 431 detector they reported a total activity of 0.019 ±0.001 counts/s/cm^3 while the partial ^{227}Ac activity was 0 .001±0.0005 counts/s/cm^3. For the SFB 308 detector the total activity was 0.043±0.001 counts/s/cm^3 while the partial ^{227}Ac activity was 0.022±0.001 counts/s/cm^3. The partial ^{227}Ac activity of the KFUPM $CeBr_3$ detector is 85 % higher than that of the SBX 431 detector and it is 3.1 times less than that of SFB 308 detector. This intrinsic activity variation may be due to different ^{227}Ac contaminants in the $CeBr_3$ detector crystals used [59].

Previously, the intrinsic activity rates of cylindrical 76 mm x 76 mm $LaBr_3$:Ce detector [55] and $LaCl_3$:Ce detector[54] were determined from the 1468 keV peak activity. The intrinsic activity-rate of the $LaCl_3$:Ce detector was measured to be 0.157counts/s/cm^3 while for the $LaBr_3$:Ce detector it was measured to be 0.182 counts/s/cm^3. Compared to the intrinsic activities of $LaCl_3$:Ce and $LaBr_3$:Ce detectors, the total activity of the $CeBr_3$ detector (used in the present study) is 7 and 8 times less than those of the $LaCl_3$:Ce [54] and $LaBr_3$:Ce detectors [55], respectively.

The intrinsic activity of the cylindrical $LaCl_3$:Ce detector was also recorded following a procedure similar to the one used for the $CeBr_3$ detector. Figure 3.21 shows the intrinsic spectrum of the $LaCl_3$:Ce detector showing the 1468 keV intrinsic activity peak due to the decay of radioactive lanthanum impurity superimposed upon ^{207}Bi source spectrum taken with the detector. Details of the origin of this activity have been published earlier [51].

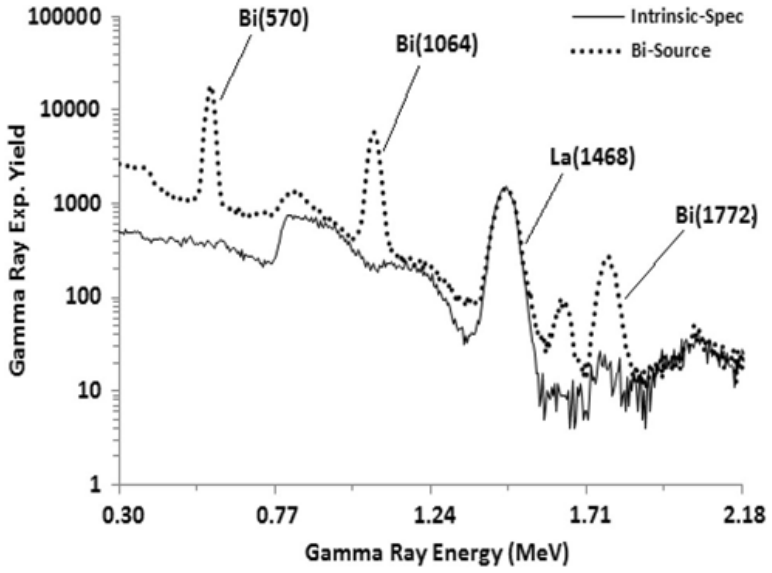

Figure 3.21: $LaCl_3$:Ce detector Intrinsic activity spectrum superimposed upon 207Bi source spectrum.

Quarati et al. [59] found that the intrinsic activity of a $CeBr_3$ detector is an order of magnitude less than the intrinsic activities of the $LaBr_3$:Ce and $LaCl_3$:Ce detectors of equivalent size.

3.3.2 Activation Spectrum of $CeBr_3$ and $LaCl_3$:Ce Detectors

The activation spectra of $CeBr_3$ and $LaCl_3$:Ce detectors were acquired using the procedure described earlier in section 3.2.2. The activation spectrum of the $CeBr_3$ detector was recorded for 40 min runs. it contains prompt gamma-rays peaks due to capture of thermal neutrons in Br and Ce elements present in the detector along with small intrinsic activity peaks due to ^{227}Ac contamination. Using a pulsed neutron beam improves the signal to background ratio because the beam associated background is reduced and is produced only during beam pulse duration. Energies and intensities of prominent prompt gamma-rays due to capture of thermal neutrons in bromine and cerium in the $CeBr_3$ detector are listed in Table 3.1 [57].

The activation spectrum of the $CeBr_3$ detector measured over 0.24-2.35 MeV energy is shown in Fig. 3.22. It contains most of the prompt gamma-ray lines of bromine and cerium from Table 3.1 over this energy range along with the 2.22 MeV hydrogen capture peak of thermal neutrons in the moderator.

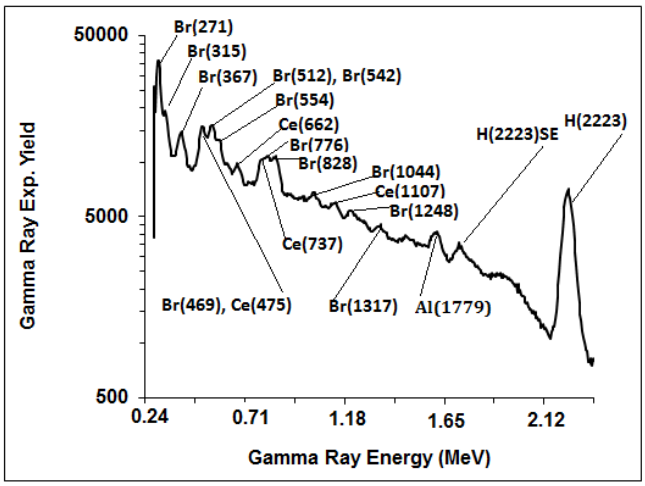

Figure 3.22: Activation spectrum of the $CeBr_3$ Detector.

Figure 3.23 shows an enlarged part of $CeBr_3$ detector activation spectrum over 0.0- 1.10 MeV superimposed upon ^{137}Cs source spectrum. The spectrum shows well resolved Br(196) , Br(271) and Br(367) peaks due to capture of thermal neutrons in bromine within the $CeBr_3$ detector material. Similar bromine energy peaks were also observed before along with La(163) peak in activation spectrum of a 100 mm x 100 mm $LaBr_3$:Ce detector, as shown in Fig. 3.24 [60].

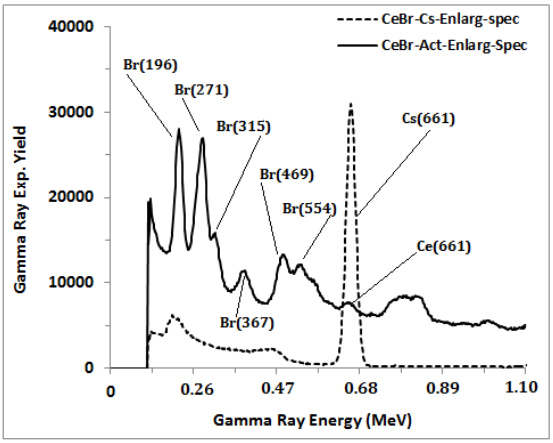

Figure 3.23: Portion of $CeBr_3$ activation spectrum superimposed upon ^{137}Cs source spectrum.

The activation spectrum of the $LaCl_3$:Ce detector was recorded for 30 mins. Fig. 3.25 shows the $LaCl_3$:Ce detector activation spectrum for gamma ray energies below 2.40 MeV. The spectrum shows well resolved peaks of La(271), Cl(517), Cl(1165), Cl(1951-1959) and H(2223) peaks. Similar lanthanum and cerium peaks were reported in the activation spectrum of a 76 mm x 76 mm (diameter x height) $LaBr_3$:Ce detector in Fig. 3.24 [4].

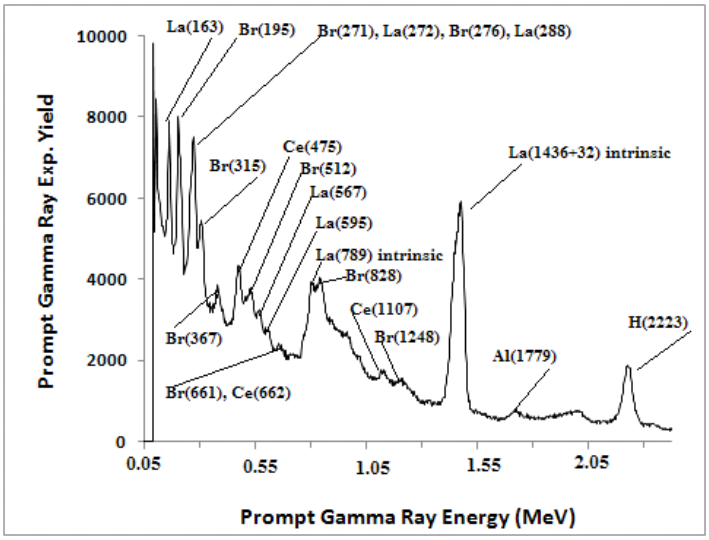

Figure 3.24: Activation spectrum of $LaBr_3$:Ce detector taken from reference [4].

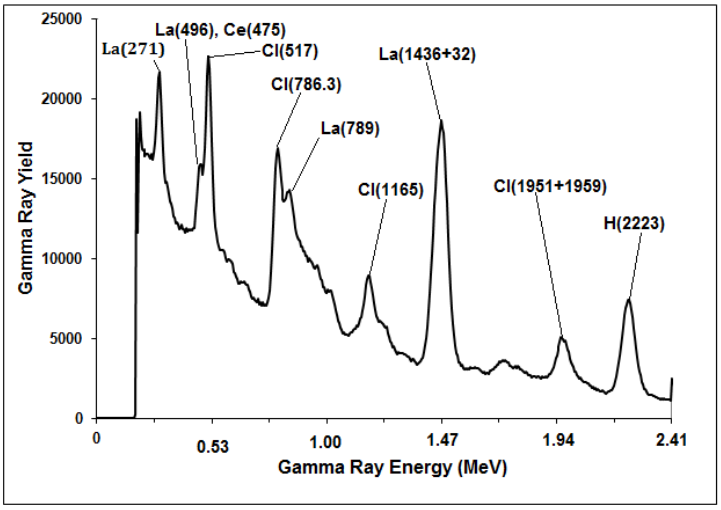

Figure 3.25: Activation spectrum of the $LaCl_3$:Ce Detector.

Due to short irradiation time, delayed gamma-rays from ^{140}La (half life = 40.3 h) could not be detected. Figure 3.26 shows an enlarged part of the $LaCl_3$:Ce detector activation spectrum over 2.13-9.69 MeV. The spectrum shows well resolved Cl(2470), Cl(2864), Cl(6111), Cl(6620-6628), Cl(6978) and Cl(8679) peaks due to capture of thermal neutrons in chlorine in the $LaCl_3$:Ce detector material [57].

Later on, all the well resolved energy peaks of the $CeBr_3$ and $LaCl_3$:Ce detectors in full as well as enlarged activation spectra were used to calculate each detector energy resolution for the corresponding gamma ray energy.

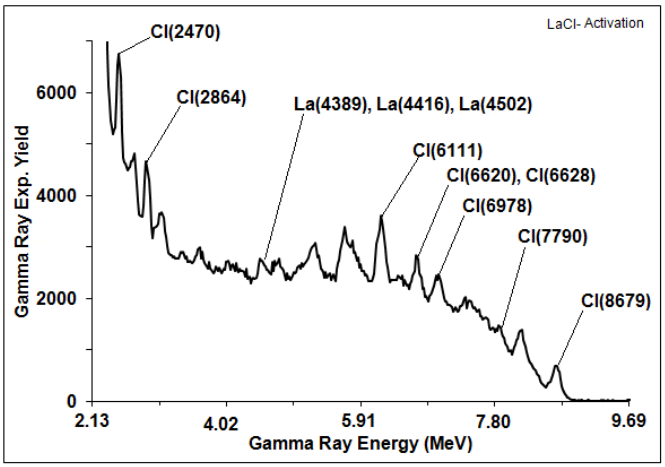

Figure 3.26: Enlarged portion of Activation spectrum of the $LaCl_3$:Ce Detector.

The energy resolution of the $CeBr_3$ detector was measured over 368 keV to 2223 keV energy using ^{207}Bi and ^{137}Cs gamma ray sources along with 2223 keV hydrogen capture peaks during prompt gamma rays studies. Energies of these gamma rays are listed in Table 3.6. For energy resolution measurements using activation spectrum of the $CeBr_3$ detector; Ce(475), and Ce(1107) peaks along with Br(196), Br(271), Br(367), Br(512), Br(554),

Br(1064) and Br (1317) peaks were analyzed. Also full energy peak and associated single escape peak of H (2223) were analyzed. Energies of theses peaks are listed in Table 3.6.

For 368 - 2223 keV gamma rays, energy resolution of the $CeBr_3$ detector varies from 6.64 ±0.04 % to 2.75±0.04 %. In Fig. 3.27 energy resolution data of the $CeBr_3$ detector is plotted as a function of gamma ray energy. Also shown in the Fig. 3.27 is a function of the type $\Delta E/E\ (\%) = a/E^b$ fitted to the $CeBr_3$ detector energy resolution data. In the fitted function a and b are constants and E_γ is the gamma ray energy given in keV. The fit is drawn with a solid line. The values of the constants a and b of the fit are listed in Table 3.4.

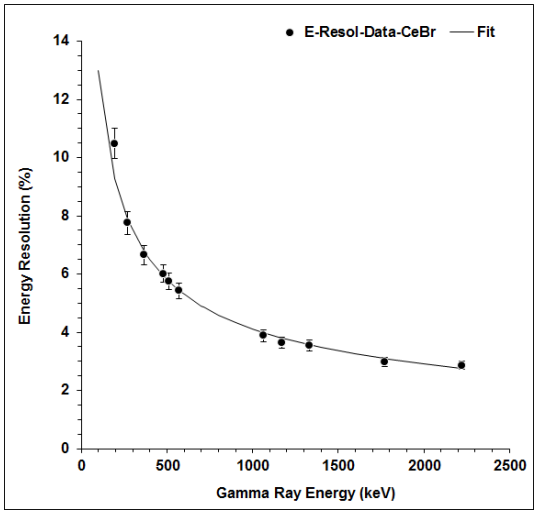

Figure 3.27: Energy resolution ΔE/E (%) data of the CeBr3 detector superimposed upon least square fit of type $\Delta E/E\ (\%) = a/E^b$

The energy resolution of the $LaCl_3$:Ce detector was measured over 272 - 8579 keV energy using 570, 1064 and 1770 keV gamma rays fron ^{207}Bi source along with 2223 keV hydrogen capture peaks during prompt gamma rays studies. For energy resolution measurements using activation spectrum of $LaCl_3$:Ce detector La(272), La(4502), Cl(1165), Cl(2470), Cl(2864), Cl(6111), Cl(6620), Cl(6978), Cl(7790) and Cl(8579)

peaks were analyzed. For 272 - 8579 keV gamma rays, the energy resolution of the $LaCl_3$:Ce detector varies from 7.09 ±0.02 % to 0.90±0.01 % .

Table 3.4: Coefficients of Fit of type $\Delta E/E(\%) = a/E^b$ to the Energy Resolution Data of (50 mm x50 mm) $CeBr_3$ [59], (76 mm x76 mm) $CeBr_3$, (76 mm x76 mm) $LaCl_3$;Ce, (50 mm x 50 mm) $LaBr_3$:Ce[59] and (100 mm x 100 mm) $LaBr_3$:Ce [60] detectors.

Detector Type	Detector Size	$\Delta E/E(\%) = a/E^b$	
		A	***b***
$CeBr_3$	76 mm x76 mm	130	0.507
$CeBr_3$ [12]	50 mm x50 mm	108	0.498
$LaBr_3$:Ce [12]	50 mm x50 mm	81	0.501
$LaCl_3$:Ce	76 mm x76 mm	122	0.505
$LaBr_3$:Ce [3]	100 mm x 100 mm	174	0.484

In Fig. 3.28, the energy resolution data of the $LaCl_3$:Ce detector is plotted as a function of as a function of gamma ray energy. Also in Fig. 3.28, the energy resolution data of the $LaCl_3$:Ce detector is a fitted with a function of the type $\Delta E/E$ (%) = a/E^b, where a and b are constants and E_γ is gamma ray energy given in keV. The fit is drawn with a solid line.

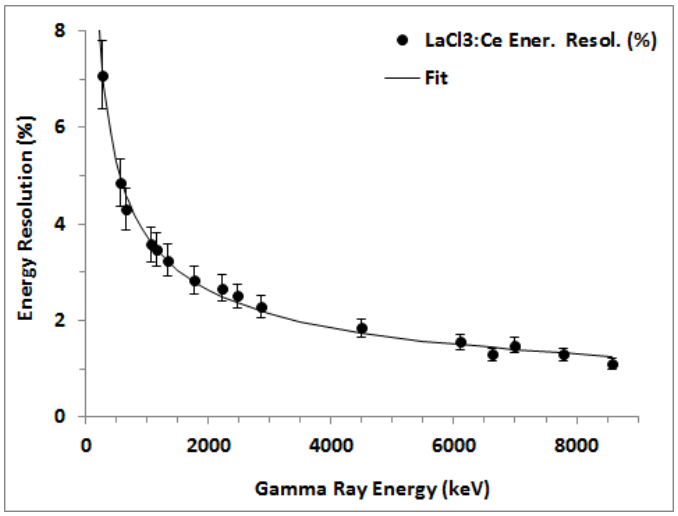

Figure 3.28: Energy resolution $\Delta E/E$ (%) data of the $CeBr_3$ detector superimposed upon least square fit of type $\Delta E/E$ (%) = a/E^b

The values of the constants *a* and *b* of the fit are listed in Table 3.4. Further energy resolution data of 50 mm x 50 mm (height x diameter) $CeBr_3$ and $LaBr_3$:Ce detectors [59] has been included in Table 3.4 for comparison with the present energy resolution data of the 76 mm x 76 mm (diameter x height) $CeBr_3$ and $LaCl_3$:Ce detectors. Also, the energy resolution data of a large 100 mm x 100 mm $LaBr_3$:Ce [60] has been included in Table 3.4.

As expected, the fit coefficient *b* for both types of detectors has a value of about 0.5. The value of the coefficient *a* shows dependence on detector volume and energy resolution at 661 keV. For detectors of the same type its value increases with detector volume. For detectors of different types but with the same volume, its value is proportional to the energy resolution of the detector for 661 keV gamma rays.

A comparison of coefficient ***a*** values of energy resolution fit to the data of 50 mm x 50 mm $CeBr_3$ detector data [59] and that of 76 mm x 76 mm $CeBr_3$ detector of the present study shows 20% larger value of the coefficient *a* for our 76 mm x 76 mm detector. Due to larger volume of the 76 mm x 76 mm $CeBr_3$ used in the present study, it might have resulted in increasing light absorption with increasing Ce contents in the larger volume $CeBr_3$ detector and hence poorer light collection in the larger volume $CeBr_3$ detector used in the present study. Table 3.5 shows energy resolution ratios of the $CeBr_3$, $LaBr_3$:Ce and $LaCl_3$:Ce detectors of various sizes for 661 keV energies and ratio of corresponding coefficient *a* of the fit to respective detector's energy resolution data .

Table 3.5: Ratios of Energy resolution and Coefficient of Energy Resolution Fit of (50 mm x 50 mm) $CeBr_3$ [59], (76 mm x 76 mm) $CeBr_3$, (76 mm x 76 mm) $LaCl_3$;Ce, (50 mm x 50 mm) $LaBr_3$:Ce [59] and (100 mm x 100 mm) $LaBr_3$:Ce [60] detectors

Detector* Ratio	**Energy Resolution (%) Ratio for 661 keV gamma rays**	***Ratio of Corresponding a coefficient of the fit***
$CeBr_3$ (50 mm) /$CeBr_3$(76 mm)	1	0.830
$CeBr_3$(76 mm) / $LaBr_3$Ce(50 mm)	1.517	1.333
$CeBr_3$(76 mm)/ $LaCl_3$:Ce (76 mm)	1.071	1.066
$LaCl_3$:Ce (76 mm)/ $LaBr_3$:Ce (100 mm)	0.774	0.701

*Detector is marked by detector diameter (x mm) assuming a cylindrical (x mm , x mm) .detector.

As expected, the coefficient ratio has good agreement with the 661 keV energy resolution data. The disagreement between the two values is only in the case when the two detectors under comparison have different volumes.

3.4 Energy Resolution Measurements of the BGO Detector

Cylindrical 102 mm x 102 mm (height x diameter) BGO detector was acquired from Scionix, Holland. The detector performance tests were carried out prior to its application in the detection of the toxic elements chromium and nickel. In these tests the response of the detector was measured for various monoenergetic gamma rays from radioisotope sources as well as prompt gamma rays emitted from detector material due to thermal neutron capture, following the procedure used for energy resolution measurements of the $CeBr_3$ and $LaCl_3$:Ce detectors [61]. Also, the detector activation spectrum was analyzed due to capture of thermal neutrons in detector material.

The energy resolution of the BGO detector was measured over 0.36-8.99 MeV energy using ^{207}Bi, ^{137}Cs and ^{133}Ba mono energetic gamma ray. Also used for this purpose were the Bi(2505) , Bi(2828), Ni(8533) and Ni(8998) peaks of the activation spectrum of the BGO detector and nickel contaminated water sample, along with H(2223) hydrogen capture peak from the moderator, as shown in Fig. 3.29.

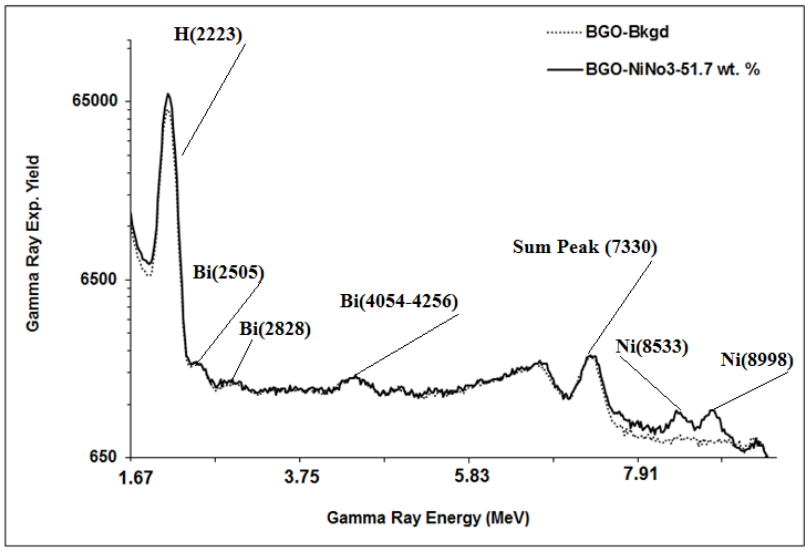

Figure 3.29: Prompt gamma-rays pulse height spectra of nickel nitrate $Ni(NO_3)_2$ contaminated water sample superimposed upon background spectrum taken with a BGO detector for energy resolution measurements.

Additionally, two naturally occurring gamma rays, namely the La(789) and La(1468) peaks, emitted by a 76 mm x 76 mm cylindrical $LaCl_3$:Ce detector, were also recorded using the BGO detector. Figure 3.30 shows the $LaCl_3$:Ce detector gamma ray intrinsic activity spectrum superimposed upon the background spectrum measured by a BGO detector.

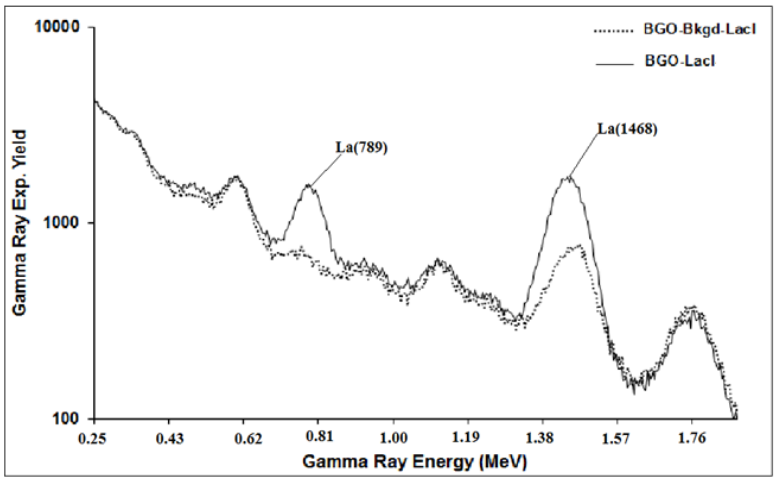

Figure 3.30: Intrinsic activity spectrum of a $LaCl_3$:Ce detector counted with a BGO detector along with background spectrum of the BGO detector.

Figure 3.31 shows the La(789) and La(1468) gamma ray difference spectrum from the $LaCl_3$:Ce detector measured by the BGO detector. These La gamma rays were also included in energy resolution measurements of the BGO detector.

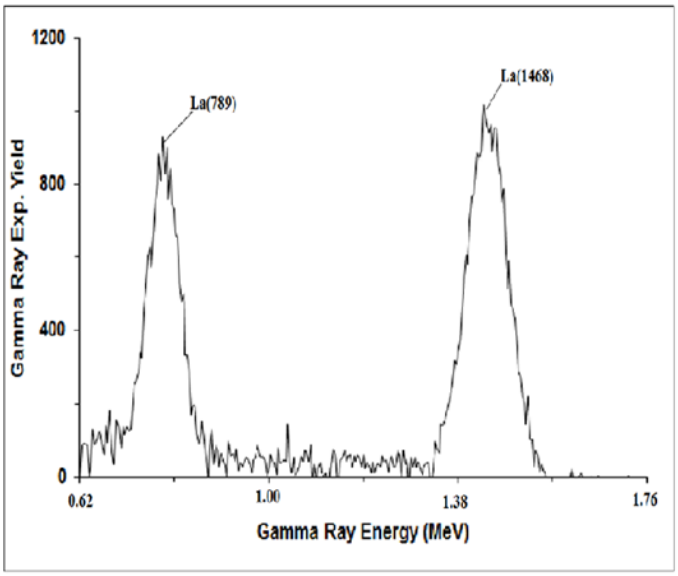

Figure 3.31: Difference of Intrinsic activity spectrum of a $LaCl_3$:Ce showing two peaks of La(1468) and La(789) impurity in $LaCl_3$:Ce detector measured by the BGO detector.

The energy resolution of the BGO detector varies from (14.2 ± 1.70) % to (2.40 ± 0.02) % over the 0.36-8.99 MeV energy range. In Fig.3.32, the energy resolution data of the BGO detector is plotted as a function of gamma ray energy. The data is fitted by the function $\Delta E/E(\%) = a/\sqrt{E(MeV)}$, with a = 104.26. The fit is drawn with a solid line. As expected, there is good agreement between the data and the fit.

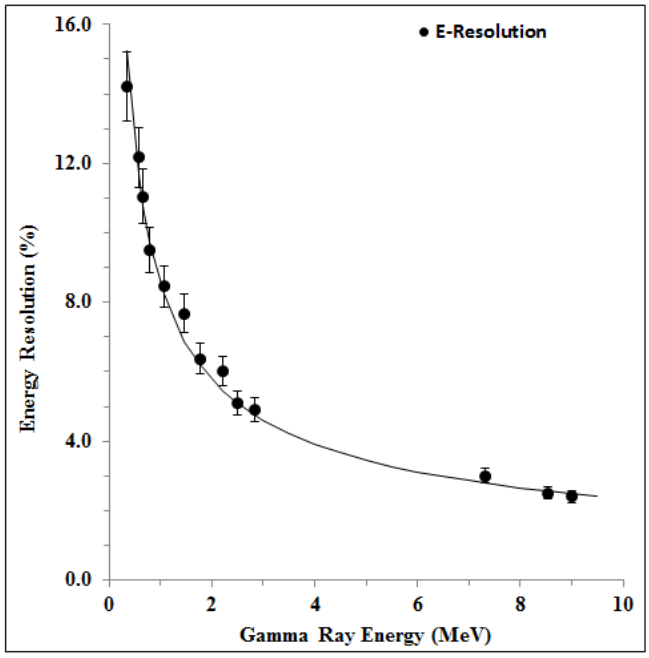

Figure 3.32: Energy resolution of BGO detector plotted as a function of gamma ray energy. Solid line represents fitted curve of type E Resol (%) =104.26 x $E^{-0.519}$ to the experimental data

CHAPTER 4

PROMPT GAMMA ANALYSIS OF B, Cd, Hg, Cr, Ni AND Cl CONTAMINATED WATER SAMPLES

In this study, contaminated water samples have been analyzed through Thermal Neutron Capture (TNC) technique using 76 mm x 76 mm (diameter x height) $CeBr_3$ and 102 mm x 102 mm (diameter x height) BGO detectors. The measurements were carried out using a portable neutron generator-based PGNAA setup shown in Fig. 4.1. Contaminated water samples analysis is importance for environmental pollution studies due to their toxicity.

4.1 Experimental Setup

The prompt gamma measurements of toxic water samples were recorded using portable neutron generator-based (PGNAA) setup shown in Figure 4.1. it consists of a cylindrical moderator made of high density polyethylene. The moderator has a central cylindrical cavity that can accommodate a cylindrical sample with a maximum diameter of 9 cm and a length of 14 cm, respectively. A gamma ray detector, placed with its longitudinal axis aligned along the moderator and sample's major axis, views the sample at a right angle to the neutron beam axis. Figure 4.1 shows the PGNAA setup used in this study. In order to prevent unwanted gamma-rays and neutrons from reaching the detector, lead and paraffin shielding were provided around the gamma-ray detector. Neutron shielding was made up of a mixture of paraffin and lithium carbonate mixed in equal weight proportions.

Samples were poured in cylindrical plastic bottles of 14 cm length and 9 cm internal diameter. They were then irradiated using a pulsed beam of 2.5 MeV neutrons with 70 keV voltage and a current of 70 μA. The prompt gamma-ray data from the samples were acquired for 25 min.

The detector's signals were acquired using standard NIM electronics modules. The signal that was routed through a preamplifier and then processed through a spectroscopy amplifier with shaping time of 1 μs. A Logical gate signal was generated for each signal processed by the amplifier using single channel analyzer and gate and delay generator modules. For dead time correction, one of the outputs of the gate and delay generator was used to gate the Multichannel Buffer, while another output was used to calculate the dead time correction.

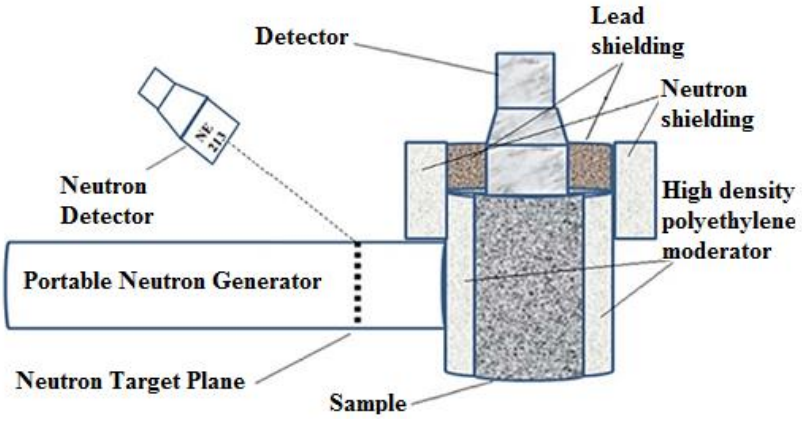

Figure 4.1: Schematic representation of the MP320 portable neutron generator used to measure the prompt gamma-ray yield from the samples.

4.2 Sample Preparation

Boric acid (H_3BO_3), Cadmium acetate ($Cd(CH_3CO_2)_2$), Mercuric nitrate ($Hg(NO_3)_2$), Chromium oxide (CrO_3), Nickel nitrate ($Ni(NO_3)_2$) and NaCl compounds were used to

prepare boron, cadmium, mercury, chromium, nickel and chlorine contaminated water samples. The concentrations of boron, cadmium, mercury, chromium, nickel and chlorine-contaminated water samples were independently measured in the Department of Chemistry, King Fahd University of Petroleum and Minerals, Dhahran, Saudi Arabia using chemical methods, such as Atomic Absorption Spectrometry. B, Cd, Hg, Cr, Ni and Cl samples were thoroughly mixed with pure water and thereafter poured in cylindrical plastic bottles with 140 mm length and 90 mm internal diameter. Table 4.1 shows the concentration of B, Cd, Hg, Cr, Ni and Cl samples mixed in water.

Table 4.1: Concentrations of B, Cd, Hg, Cr, Ni and Cl Samples Mixed in Water.

Elements	Concentrations (wt. %)
B	**0.31, 1.25 and 2.50, wt. %**
Cd	**0.0625, 0.125, and 0.250 wt. %**
Hg	**0.75 , 1.25 and 2.5 wt. %**
Cr	**2.9, 4.35, 5.8, 7.5, 11.4 and 15.7 wt. %**
Ni	**20.3, 24.2, 28.3, 36.4 and 51.7 wt. %**
Cl	**2, 4, 6 and 8 wt. %**

4.3 Prompt Gamma-ray Analysis of Contaminated Water Samples Using $CeBr_3$ Detector.

The prompt gamma-ray analysis of contaminated water samples were carried out using the $CeBr_3$ detector based PGNAA setup utilizing a portable neutron generator, following the procedure described earlier in section 4.1. A pulsed beam of 2.5 MeV neutrons was produced via D(d,n) reaction using 70 μA deuteron beam current and 70keV energy. The deuteron pulse had a width of 800 micro seconds and a frequency of 250Hz. The prompt gamma-ray data from contaminated water samples were acquired for preset number of time using Multichannel Buffer based data acquisition system. The data collection time for

samples typically varied from 20-30 mins. Due to the low neutron flux of the portable neutron generator, the data collection time for chromium and nickel samples typical varied from 60-130 mins. The neutron flux was monitored during each run using a cylindrical NE213 detector with pulse shape discrimination. The neutron monitor spectrum was used for neutron flux normalization during data correction.

4.3.1 Boron, Cadmium, Mercury, Chromium and Nickel Contaminated Water Samples Data.

Figure 4.2 shows the pulse height spectra of prompt gamma-rays from water samples containing 2.5 wt.% mercury, 0.25 wt.% boron and 0.25 wt.% cadmium superimposed upon the background spectrum.

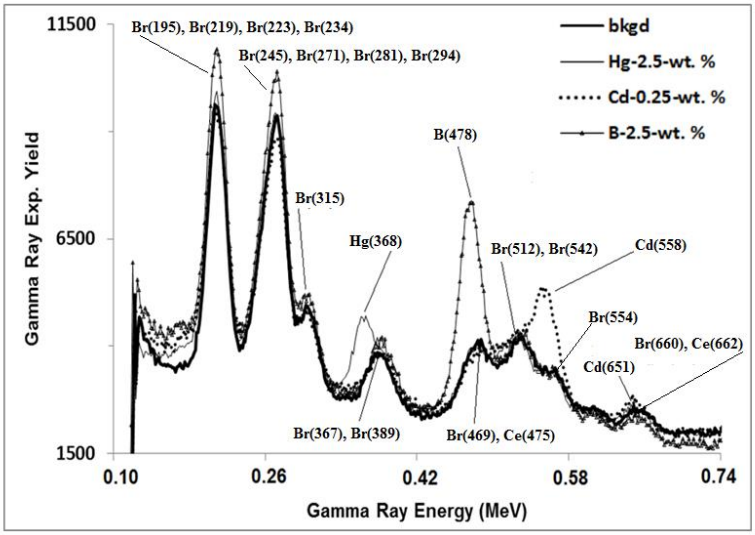

Figure 4.2: Enlarged prompt gamma-ray experimental pulse height spectra of boron, mercury and cadmium contaminated water samples superimposed upon background spectrum taken with pure water sample, showing location of boron, mercury and cadmium peaks and their interference with detector activation peaks.

Due to the finite energy resolution of the detector, the energy of the centroid of the resultant peak of the unresolved interfering peaks is given by a cross section-weighted average

energy of the peaks. For Br(367) and Br(389) peaks, the resultant peak centroid energy is 378keV, which was verified experimentally. Similarly for Br(469), Ce(475) and Br(512) peaks, the cross section-weighted energy of resultant peak centroid is 486keV. The cross section-weighted centroid energy of Br(512) and Br(542) interfering peaks is 522keV.The cross section-weighted centroid energy of Br(554), Br(616) and Br (619) interfering peaks is 576keV. All resultant peak centroid energies have been verified experimentally.

Figures 4.3 and 4.4 show pulse height spectra of prompt gamma-rays from water samples containing 0.75, 1.25 and 2.5 wt.% mercury superimposed upon each other along with a background spectrum taken with a pure water sample. In order to show the effect of increasing concentration of mercury on the pulse height spectrum, pulse height spectra for different mercury concentrations are plotted over 0.32 to 0.64 MeV. Figure 4.3 shows the 368 keV mercury peak on enlarged scale to indicate its interference with 367 and 389 keV peak from activation of bromine in $CeBr_3$ detector.

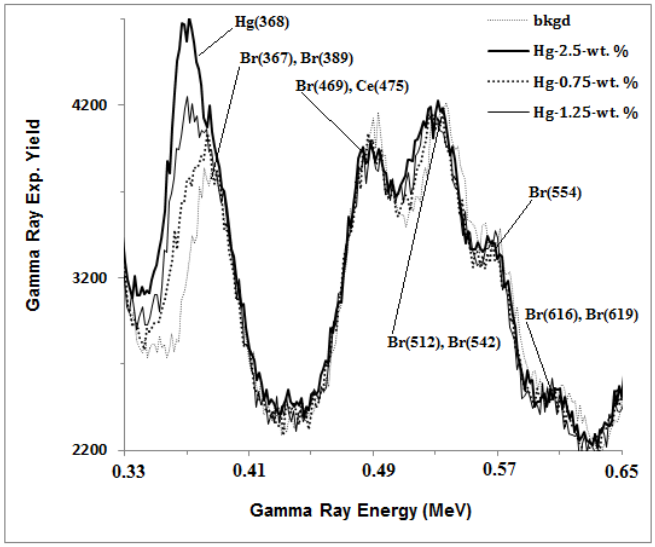

Figure 4.3: Prompt gamma-rays pulse height spectra of three mercury contaminated water samples containing 0.75, 1.25 and 2.50wt% mercury superimposed upon background spectrum taken with pure water.

Since mercury peaks contain the contribution of Br(367) and Br(389) peaks, difference spectra of mercury peaks for 0.75, 1.25 and 2.5 wt. % concentrations were generated by subtracting the background spectrum from each of them. Figure 4.4 shows the enlarged difference spectra of mercury peaks for 0.75, 1.25 and 2.5 wt % mercury concentrations.

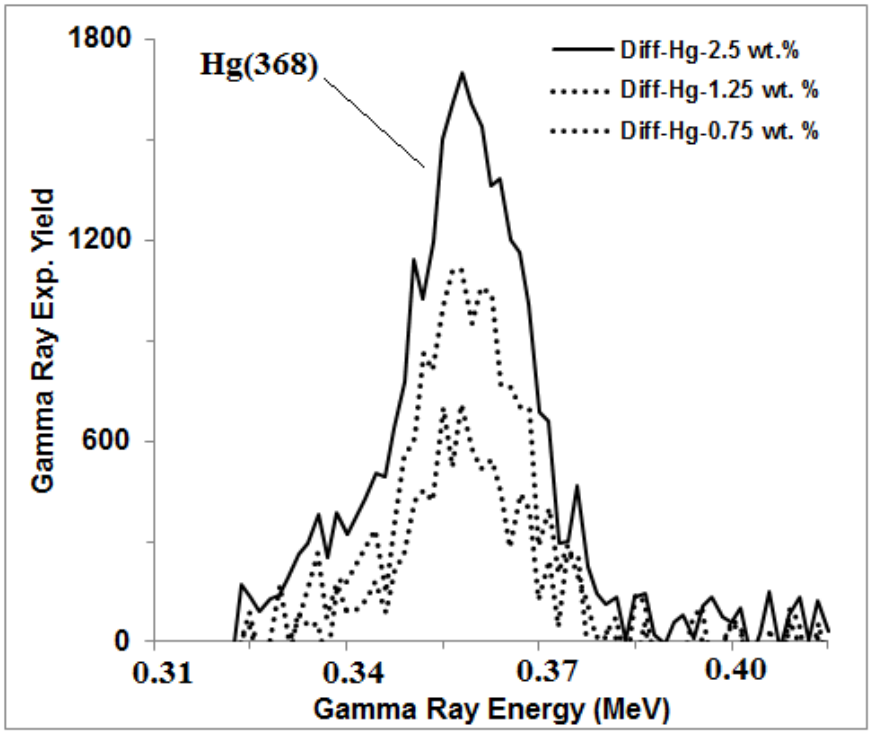

Figure 4.4: Enlarged prompt gamma-rays pulse height spectra of water samples containing 0.75, 1.25 and 2.50wt% mercury after background subtraction.

Figures 4.5 and 4.6 show pulse height spectra of prompt gamma-rays from water samples containing 0.031, 0.125, and 0.25 wt. % boron superimposed upon each other along with background spectrum taken with a pure water sample. In order to show the effect of increasing concentration of boron on the pulse height spectrum, pulse height spectra for different boron concentrations are plotted over 0.31-0.42 MeV energies. Figure 4.5 shows the 478 keV boron peak interference on enlarged scale with the Br(469) and 475 keV peak

of cerium from the activation of the $CeBr_3$ detector. Since boron peaks contain the contribution of Ce(475) and Br(469) peaks, difference spectra of boron peaks for 0.031, 0.12 and 0.25 wt. % concentrations were generated by subtracting the background spectrum from each of them. Figure 4.6 shows the difference spectra of boron peaks for 0.031, 0.125, and 0.25 wt. % boron concentrations.

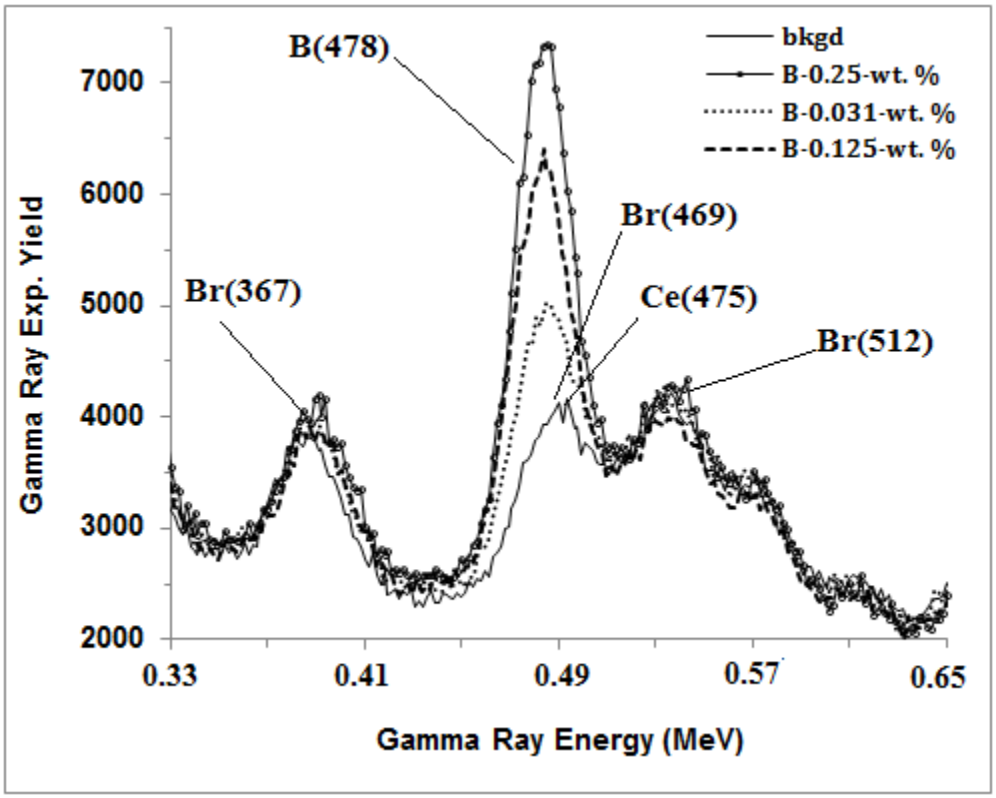

Figure 4.5: Prompt gamma-rays pulse height spectra of three boron contaminated water samples containing 0.031, 0.125 and 0.250 wt% boron superimposed upon background spectrum taken with pure water.

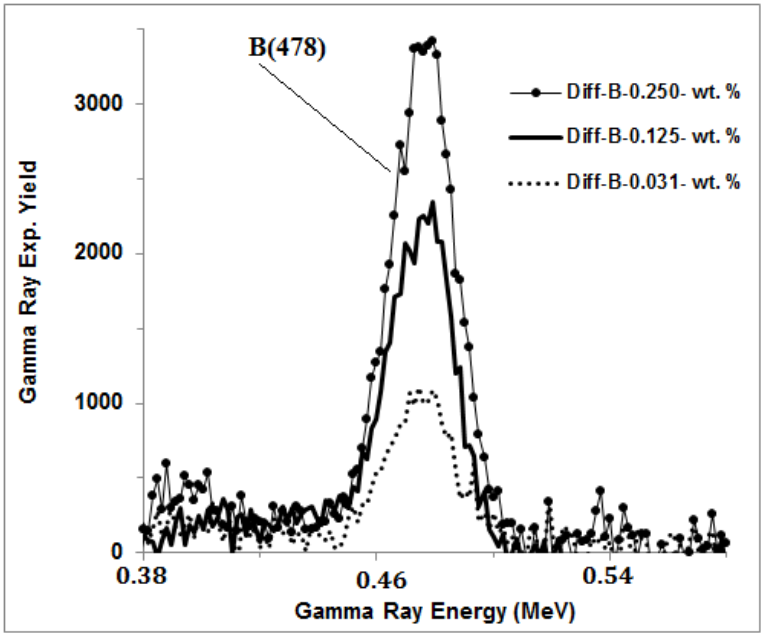

Figure 4.6: Enlarged prompt gamma-ray pulse height spectra of water samples containing 0.031, 0.125 and 0.250 wt% boron after background subtraction.

Figures 4.7 and 4.8 show the pulse height spectra of prompt gamma rays from water samples containing 0.0625, 0.125 and 0.25 wt. % cadmium superimposed upon each other along with background spectrum taken without sample. In order to show effect of increasing concentration of cadmium on the pulse height spectrum, pulse height spectra for different cadmium concentration are plotted over 0.32-0.64 MeV energies. Figure 4.7 shows the 558 keV cadmium peak on enlarged scale to indicate its interference with 554, 616 and 619 keV peaks from activation of bromine in the $CeBr_3$ detector. Since the cadmium peak contains the contribution of bromine peaks, the difference spectra of cadmium peaks for 0.0625, 0.125 and 0.25 wt. % concentrations were generated by subtracting the background spectrum from each of them. Figure 4.8 shows the difference spectra of cadmium peaks for 0.0625, 0.125 and 0.25 wt. % cadmium concentrations.

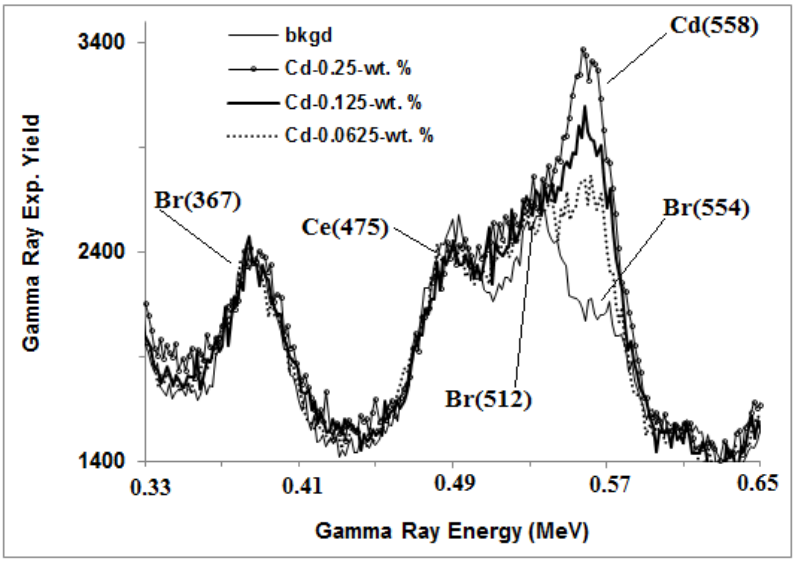

Figure 4.7: Prompt gamma-rays pulse height spectra of three cadmium contaminated water samples containing 0.0625, 0.125 and 0.250wt% cadmium superimposed upon background spectrum taken with pure water.

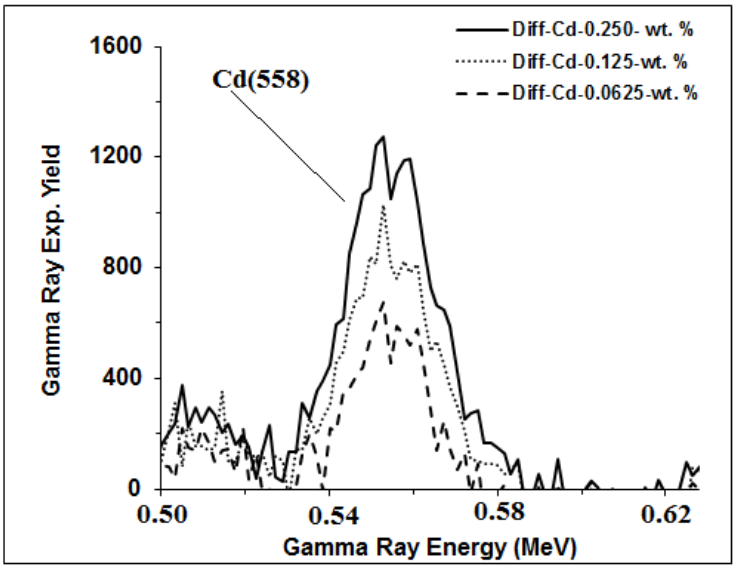

Figure 4.8: Enlarged prompt gamma-rays pulse height spectra of water samples containing 0.0625, 0.125 and 0.250wt% cadmium after background subtraction.

Figure 4.9 shows the pulse height spectra of prompt gamma-rays from water samples containing 2.9, 4.35, 5.8, 7.5, 11.4 and 15.7 wt. % chromium concentrations superimposed upon background spectrum over 1.84 to 10.1 MeV energy range. The combined Cr(8483)

and Cr(8511) chromium peaks , are quite prominent along with Cr(8884) and Cr(9719) peaks.

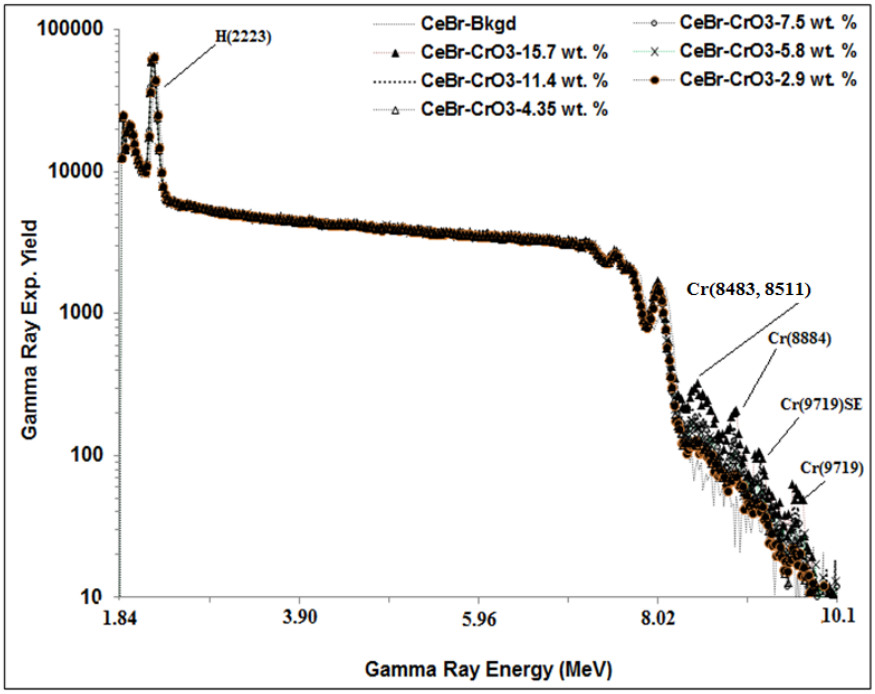

Figure 4.9: Prompt gamma-rays pulse height spectra of water samples contaminated with 2.90-15.7 wt. % chromium oxide (CrO_3) over 1.84-10.1 MeV energy range superimposed upon background spectrum.

Figures 4.10 and 4.11 show the enlarged pulse height spectra of prompt gamma-rays from chromium-contaminated water samples. Figure 4.10 shows the pulse height spectra superimposed upon each other along with beam associated-background spectrum taken with pure water sample over 8.19-9.83 MeV energy.

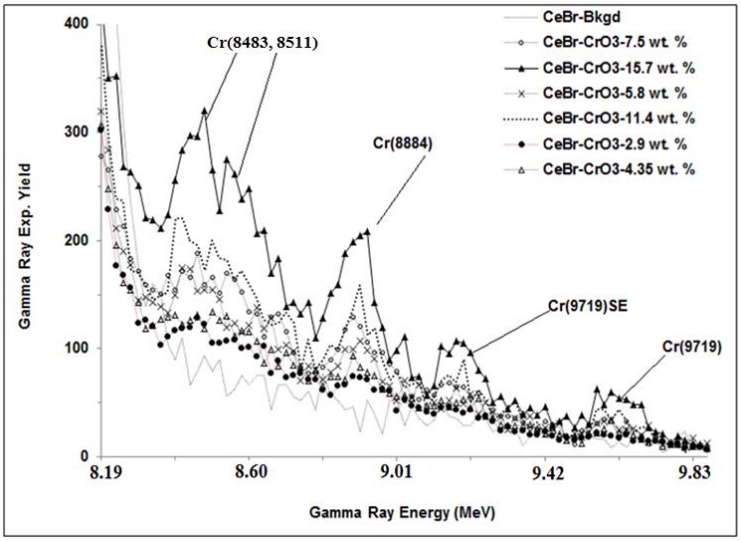

Figure 4.10: Enlarged prompt gamma-rays pulse height spectra of water samples contaminated with 2.90-15.7 wt. % chromium oxide (CrO_3) over 8.19-9.83 MeV energy range superimposed upon background spectrum.

Figure 4.11 shows the enlarged difference spectra (background subtracted**)** of chromium peaks over 8.23-9.87 MeV energy. Figures 4.10 and 4.11 show unresolved Cr(8483) and Cr(8511) chromium peaks along with Cr(8884) and Cr(9719) peaks. Also shown in the Figure is the Single Escape (SE) peak corresponding to the Cr(9719) peak.

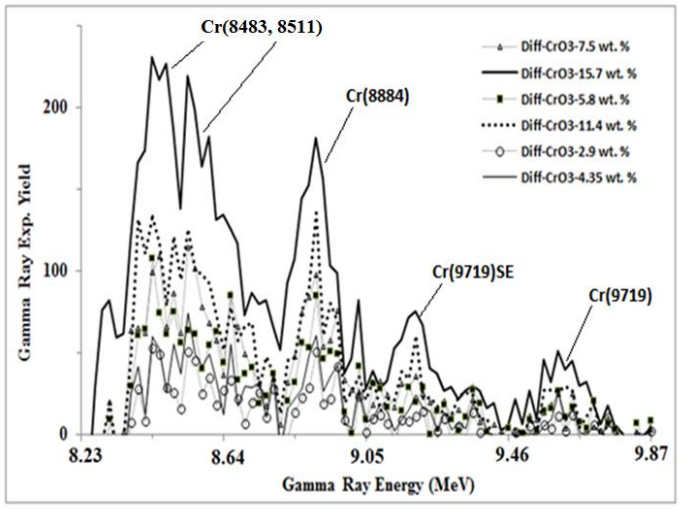

Figure 4.11: Difference pulse height spectra of water samples contaminated with 2.90-15.7 wt. % chromium oxide (CrO_3) contaminated water sample.

Figure 4.12 shows the pulse height spectra of prompt gamma-rays from water samples containing 20.3, 24.2, 28.3, 36.4 and 51.7 wt. % nickel concentrations superimposed upon the background spectrum over 1.84 to 10.1 MeV. The Ni(8533) and Ni(8998) nickel peaks , are quite prominent.

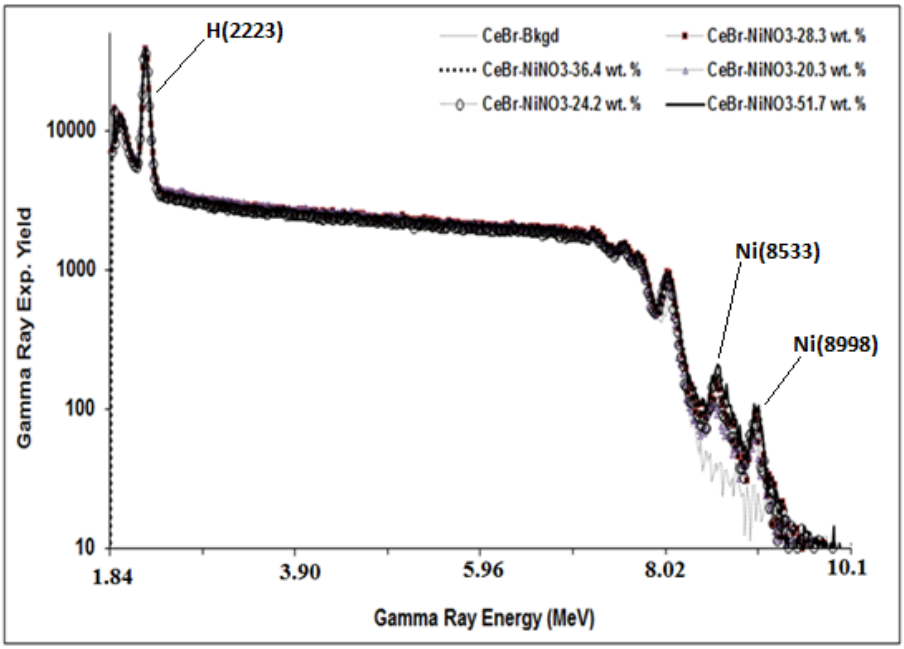

Figure 4.12: Prompt gamma-rays pulse height spectra of water samples contaminated with 20-51.7 wt % nickel nitrate $Ni(NO_3)_2$ over 1.84-10.1 MeV energy range superimposed upon background spectrum.

Figures 4.13 and 4.14 show the enlarged pulse height spectra of prompt gamma-rays from nickel-contaminated water samples. Figure 4.13 shows the nickel-contaminated water samples pulse height spectra superimposed upon each other along with beam associated-background spectrum taken with a pure water sample over 8.23-9.46 MeV energy.

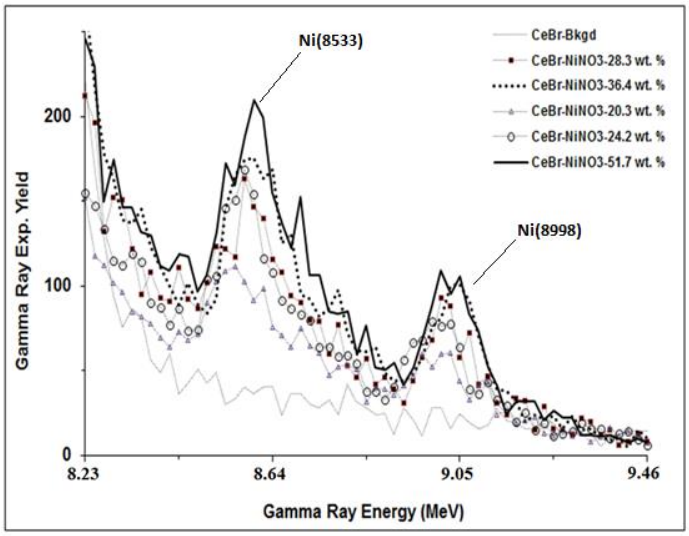

Figure 4.13: Enlarged prompt gamma-rays pulse height spectra of water samples contaminated with 20-51.7 wt % nickel nitrate $Ni(NO_3)_2$ over 8.23-9.46 MeV energy range superimposed upon background spectrum.

Figure 4.14 shows the enlarged difference spectra (background subtracted**)** of nickel peaks over 8.32-9.12 MeV energy. Figures 4.13 show the resolved Ni(8533) and Ni(8998) nickel peaks.

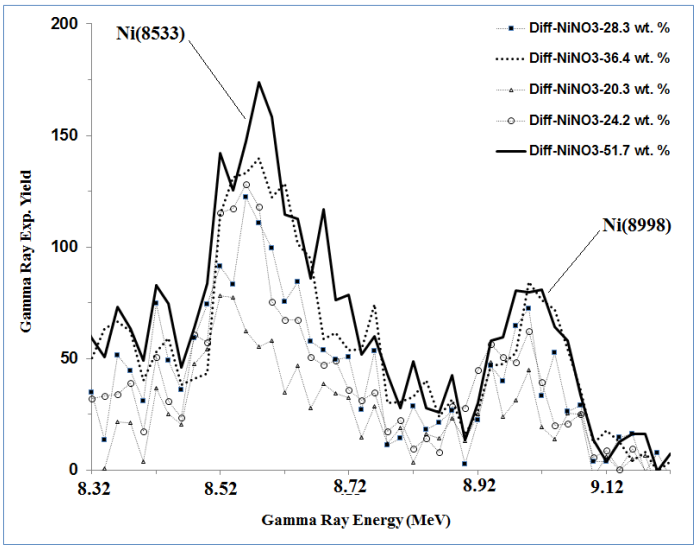

Figure 4.14: Difference pulse height spectra of water samples contaminated with 20-51.7 wt % nickel nitrate $Ni(NO_3)_2$ contaminated water sample.

4.3.2 Chlorine Contaminated Water Samples Data

The Prompt gamma ray measurements from saline samples were carried out using the $CeBr_3$ detector-based PGNAA setup utilizing the portable neutron generator described earlier in section 4.1. The setup is also shown in Fig. 4.1. Prompt gamma rays from chlorine have several intense lines with energies varying from 0.5 MeV to 8.58 MeV. In order to obtain optimum resolution of these gamma rays, measurements were carried out with two different pulse height amplifier gain settings. One setting, with larger amplifier gain was used to record low energy gamma ray energy signals below 2.22 MeV by adjusting the hydrogen peak location near the end channel of the spectrum, as shown in Fig. 4.15. Figure 4.15 shows the low energy activation spectrum of $CeBr_3$ detector due to capture of thermal neutrons in $CeBr_3$ detector material. Prompt gamma peaks due to capture of thermal neutrons in Ce, Br and H (from moderator material) are quite prominent in Figure 4.15.

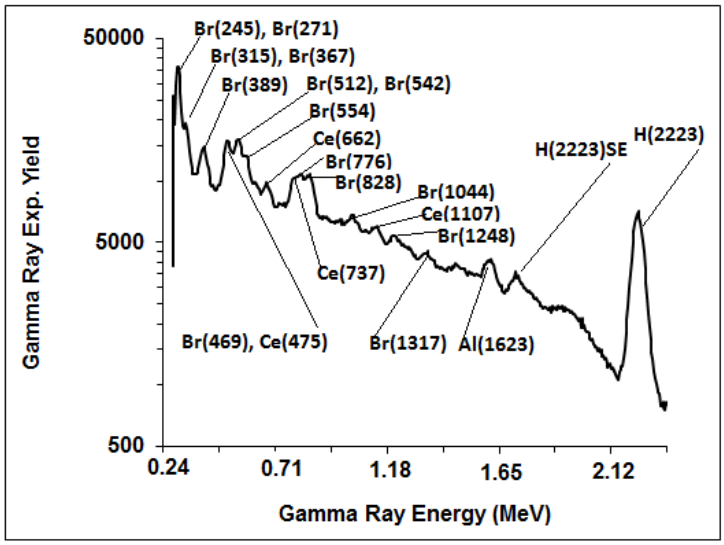

Figure 4.15: Prompt gamma-ray spectrum due to activation of the $CeBr_3$ detector caused by capture of thermal neutrons in Br and Ce elements present in $CeBr_3$ detector along with hydrogen capture peak from the moderator.

The other amplifier gain setting was used to record high energy gamma ray energies up to 9.9 MeV by adjusting the location of the hydrogen peak near the beginning channels of the spectrum, as shown in Fig. 4.16. In order to calibrate the detector for higher energy gamma rays, the detector spectrum was acquired from $NiNO_3$ sample as shown in Figure 4.16. High energy Ni(8533) and Ni(8998) keV gamma rays along with Br(7577) gamma rays peak from the detector material are quite prominent.

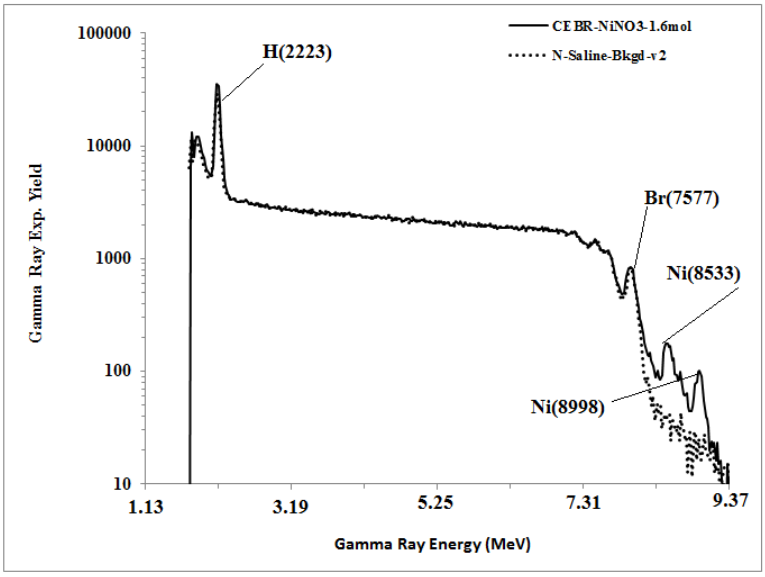

Figure 4.16: High energy calibration spectrum

For each amplifier setting, the detector background spectrum was recorded with an empty plastic container inserted into the moderator cavity. A pulsed beam of 2.5 MeV neutrons was produced via the D(d,n) reaction using a 70 μA deuteron beam current and 70 keV energy. The deuteron pulse had a width of 800 micro seconds and a frequency of 250Hz. The background spectrum of the $CeBr_3$ detector contains prompt gamma-ray peaks due to the capture of thermal neutrons in Br and Ce elements present in the $CeBr_3$ detector

material. The energies and intensities of prominent prompt gamma-rays due to the capture of thermal neutrons in cerium and bromine are listed in Table 3.1 [57].

The background spectrum must be subtracted from the sample spectrum to obtain background free prompt gamma ray spectrum of the sample. The prompt gamma-ray data from chloride-contaminated water samples were acquired for a preset time using the Multichannel Buffer based data acquisition system. The typical data collection time for saline samples varies from 20-30 mins. The neutron flux was monitored during each run using a cylindrical NE213 detector with pulse shape discrimination. The neutron flux was monitored through a beam current monitor from the neutron generator. Any fluctuation in beam current was considered while normalizing the data.

Figure 4.17 shows the low energy prompt gamma-rays spectrum from saline water samples containing 4.0 wt. % chlorine superimposed upon background spectrum over 0.41-2.29 MeV energy range. Chlorine peaks at 517, 788, 1116 and 1951-1959 keV along with 2223 keV hydrogen peak from the moderator are quite prominent.

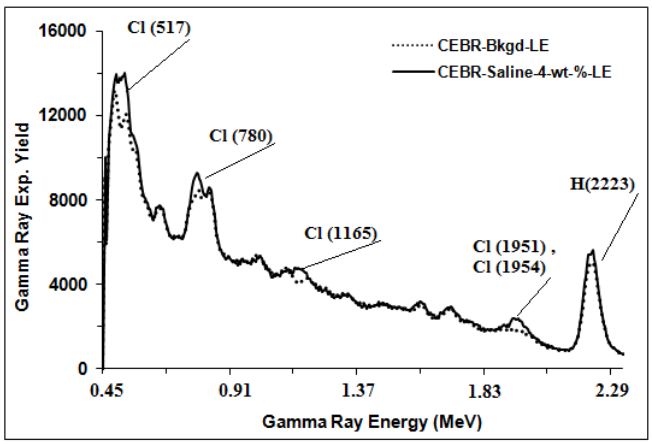

Figure 4.17: Low energy pulse height spectrum of saline water spectrum with 4 % chlorine contamination superimposed upon background spectrum.

Figure 4.18 shows low energy gamma-rays spectra from saline water samples containing 2, 4, 6 and 8 wt. % chlorine superimposed upon background spectrum over 0.41-2.32 MeV energy range. Chlorine peaks at 517, 788, 1116 and 1951 keV along with 2223 keV hydrogen peak from the moderator are quite prominent.

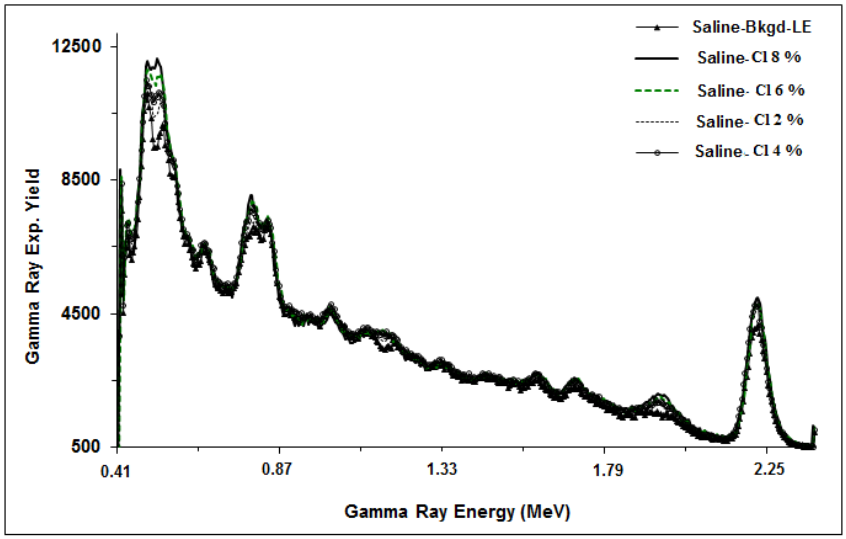

Figure 4.18: Shows the pulse height spectra of prompt gamma-rays from saline water samples containing 2, 4, 6 and 8 wt. % chlorine superimposed upon background spectrum over 0.41-2.32 MeV energy range.

Figure 4.19 shows the high-energy prompt gamma-rays spectra from saline water samples containing 4 wt. % chlorine superimposed upon background spectrum over 1.10-9.98 MeV energy range. Chlorine peaks at 6110, and 8578 keV along with 2223 keV hydrogen peak from the moderator are quite prominent. Fig. 4.20 shows enlarged part of Fig. 4.19 over 2.57-8.75 MeV range showing 2864, 3062, 4980, 5715, 6110, 6619 and 8578 keV chlorine peaks.

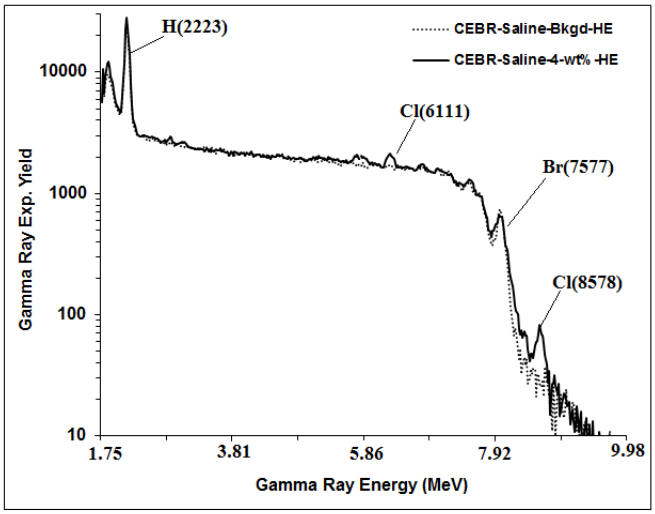

Figure 4.19: High energy pulse height spectrum of saline water spectrum with 4 % chlorine contamination superimposed upon background spectrum.

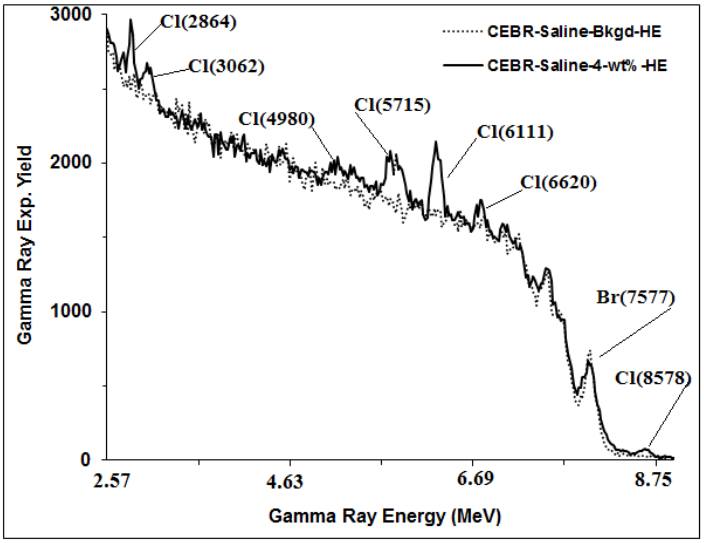

Figure 4.20: Enlarged spectrum of high energy pulse height spectrum of saline water spectrum with 4 % chlorine contamination superimposed upon background spectrum.

Figure 4.21 shows high energy gamma-rays spectra from saline water samples containing 2, 4, 6 and 8 wt. % chlorine superimposed upon background spectrum over 1.10-9.90 MeV energy range. Chlorine peaks at 8578 keV along with 2223 keV hydrogen peak from the moderator are quite prominent.

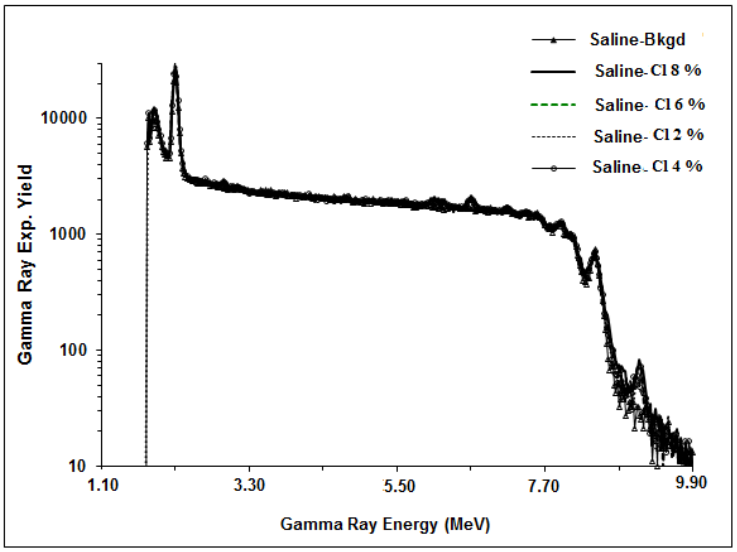

Figure 4.21: Shows the pulse height spectra of prompt gamma-rays from saline water samples containing 2, 4, 6 and 8 wt. % chlorine superimposed upon background spectrum over 1.10-9.90 MeV energy range.

Low and high energy gamma ray spectra shown in Figures 4.18 and 4.21 were analyzed using pulse height windows corresponding to 517, 788, 1165, 1951, 2863, 6110, 6619 and 8578 keV chlorine prompt gamma rays. For each gamma ray energy, the difference spectrum was generated for 2 %, 4%, 6% and 8 % chlorine sample spectra by subtracting background spectrum from each sample spectrum and normalizing to the same neutron flux. Figures 22-29 show the difference spectra of 517, 788, 1165, 1951, 2863, 6110, 6619 and 8578 keV chlorine gamma rays 2, 4, 6 and 8 wt. % chlorine in saline water. Fig. 4.22 shows 517 keV chlorine peak over 0.42-0.66 MeV energy, Fig. 4.23 shows 778 keV chlorine peak over 0.66-0.91 MeV energy, Fig. 4.24 shows 1164 keV chlorine peak over 1.09-1.24 MeV energy, Fig 4.25 shows 1951 keV chlorine peak over 1.78-2.13 MeV energy, Fig. 4.26 shows 2863 keV chlorine peak over 2.71-2.96 MeV energy, Fig. 4.27 shows 6110 keV chlorine peak over 5.84-6.28 MeV energy and Fig. 4.28 shows 6619 keV chlorine peak over 6.39-6.83 MeV energy. Fig. 4.29 shows 8578 keV chlorine peak over

8.43-8.83 MeV energy. For all the peaks, the gamma ray yield increases with increasing chlorine concentration.

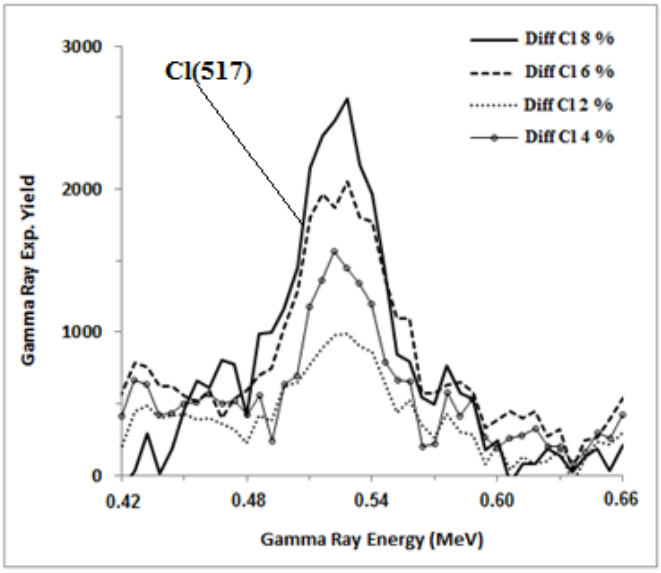

Figure 4.22: Enlarged prompt gamma-ray pulse height spectra of saline water samples containing 2, 4, 6 and 8 wt. % chlorine contamination plotted over 0.42- 0.66 MeV energy range after background subtraction.

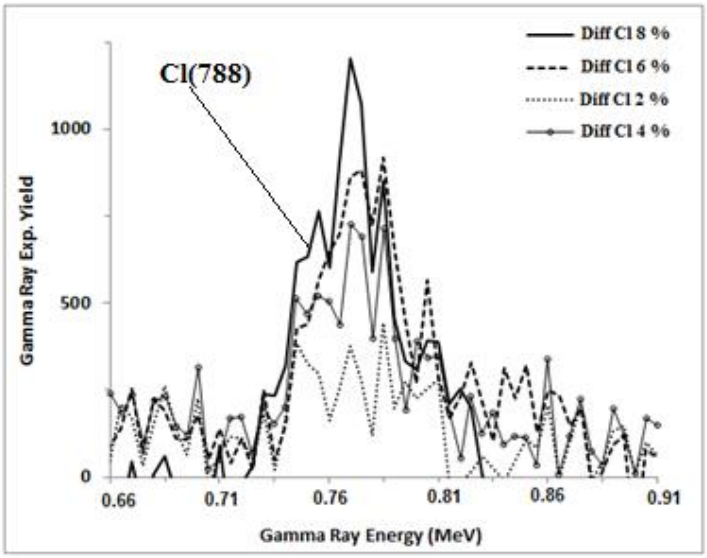

Figure 4.23: Enlarged prompt gamma-ray pulse height spectra of saline water samples containing 2, 4, 6 and 8 wt. % chlorine contamination plotted over 0.66- 0.91 MeV energy range after background subtraction.

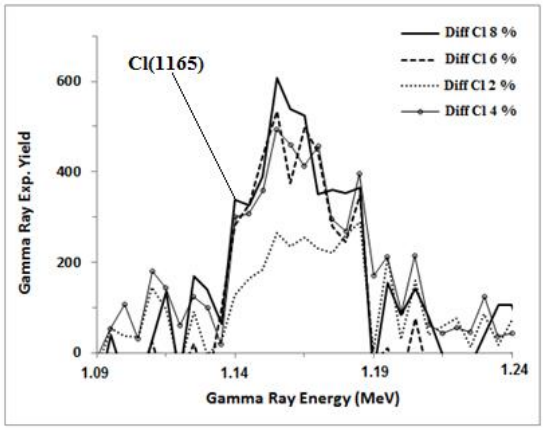

Figure 4.24: Enlarged prompt gamma-ray pulse height spectra of saline water samples containing 2, 4, 6 and 8 wt. % chlorine contamination plotted over 1.09- 1.24 MeV energy range after background subtraction.

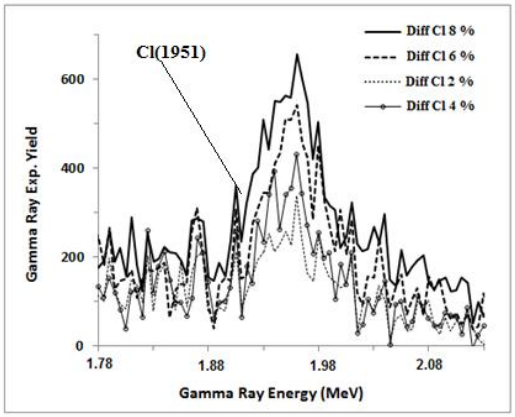

Figure 4.25: Enlarged prompt gamma-ray pulse height spectra of saline water samples containing 2, 4, 6 and 8 wt. % chlorine contamination plotted over 1.78- 2.13 MeV energy range after background subtraction.

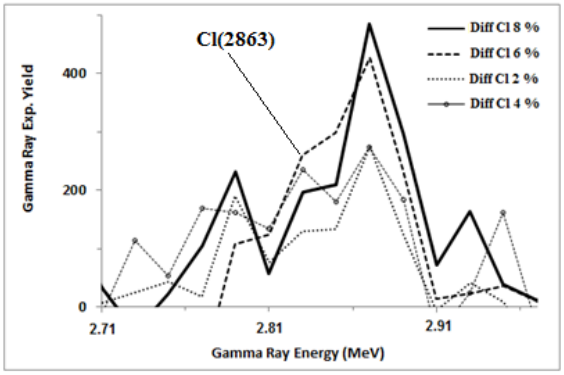

Figure 4.26: Enlarged prompt gamma-ray pulse height spectra of saline water samples containing 2, 4, 6 and 8 wt. % chlorine contamination plotted over 2.71- 2.96 MeV energy range after background subtraction.

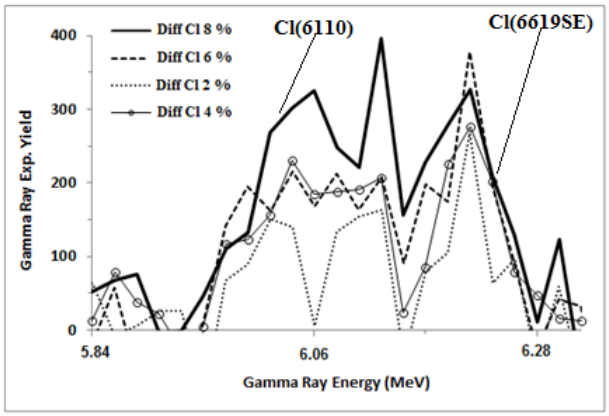

Figure 4.27: Enlarged prompt gamma-ray pulse height spectra of saline water samples containing 2, 4, 6 and 8 wt. % chlorine contamination plotted over 5.84- 6.28 MeV energy range after background subtraction.

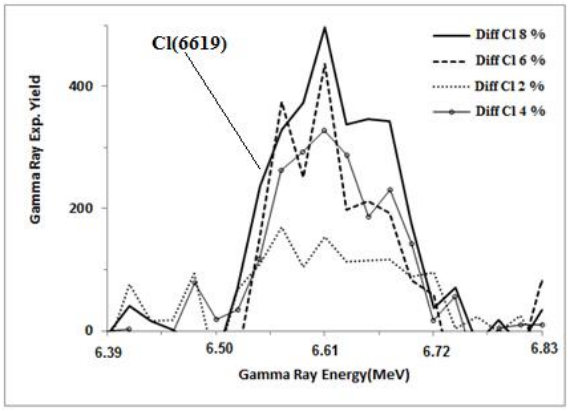

Figure 4.28: Enlarged prompt gamma-ray pulse height spectra of saline water samples containing 2, 4, 6 and 8 wt. % chlorine contamination plotted over 6.39- 6.83 MeV energy range after background subtraction.

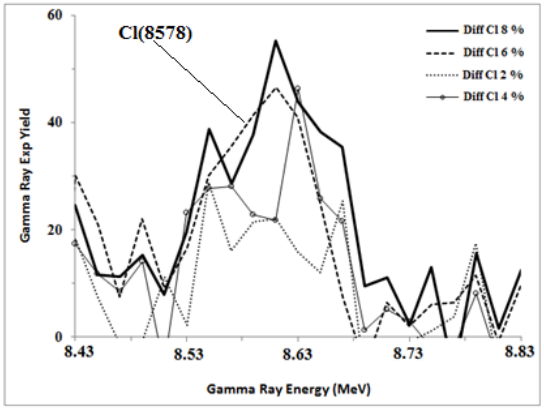

Figure 4.29: Enlarged prompt gamma-ray pulse height spectra of saline water samples containing 2, 4, 6 and 8 wt. % chlorine contamination plotted over 8.43- 8.83 MeV energy range after background subtraction.

4.4 Prompt Gamma-ray Analysis of Chromium and Nickel Contaminated Water Samples using the BGO detector

The prompt gamma-ray yield of the chromium and nickel-contaminated water samples were measured using the portable neutron generator based PGNAA setup utilizing the BGO detector following the procedure described in Section 4.1. The six chromium samples with 2.9, 4.35, 5.8, 7.5, 11.4 and 15.7 wt. % chromium concentrations and five nickel samples with 20.3, 24.2, 28.3, 36.4 and 51.7 wt. % nickel concentrations were irradiated in the portable neutron generator based PGNAA setup utilizing the BGO detector with similar accelerator beam parameters given in Section 4.5 for the measurement using the $CeBr_3$ detector. For the BGO detector based measurements the data collection time for chromium and nickel samples typical varied from 40-120 minutes.

Figure 4.30 shows the pulse height spectra of prompt gamma-rays from water samples containing 2.9, 4.35, 5.8, 7.5, 11.4 and 15.7 wt. % chromium concentrations superimposed upon background spectrum over 1.64-9.75 MeV taken with the BGO detector. The Cr(7938) peak, unresolved Cr(8483, 8511) and Cr(8884) peaks and Cr(9719) peaks are quite prominent.

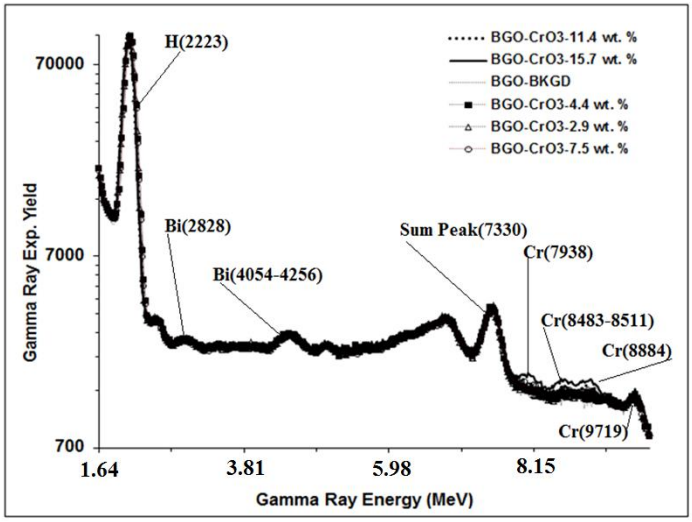

Figure 4.30: Prompt gamma-rays pulse height spectra of water samples contaminated with 2.90-15.7 wt. % chromium oxide (CrO_3) over 1.67-9.98 MeV energy range superimposed upon background spectrum.

Figures 4.31 and 4.32 show the enlarged pulse height spectra of prompt gamma-rays from chromium-contaminated water samples. Figure 4.31 shows the pulse height spectra superimposed upon each other along with beam associated-background spectrum taken with a pure water sample over 7.54-9.98 MeV energy.

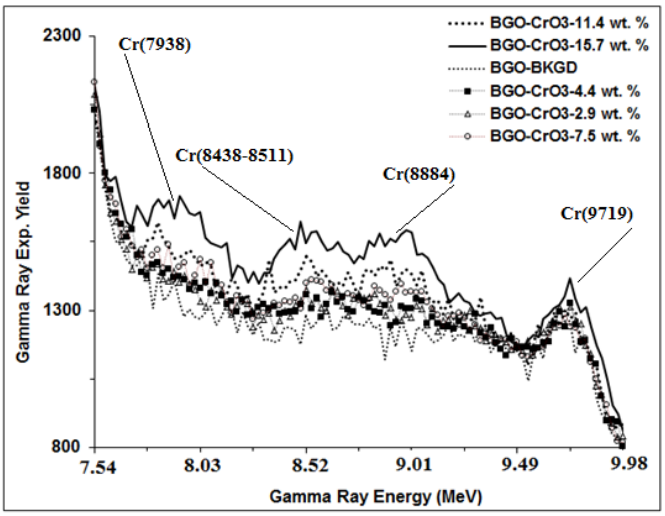

Figure 4.31: Enlarged prompt gamma-rays pulse height spectra of water samples contaminated with 2.90-15.7 wt. % chromium oxide (CrO3) over 7.54-9.98 MeV energy range superimposed upon background spectrum.

Figure 4.32 shows the enlarged difference spectra (background subtracted**)** of chromium peaks over 7.74 -9.84 MeV energy. Figures 4.31 and 4.32 show unresolved Cr(8483-8511) and Cr(8884) chromium peaks along with Cr(9719) peak.

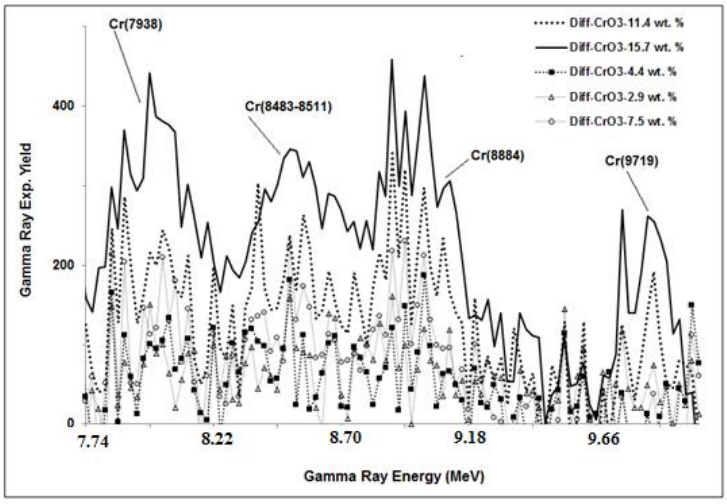

Figure 4.32: Difference pulse height spectra of water samples contaminated with 2.90-15.7 wt. % chromium oxide (CrO_3) contaminated water sample.

Figure 4.33 shows the pulse height spectra of prompt gamma-rays from water samples containing 20.3, 24.2, 28.3, 36.4 and 51.7 wt. % nickel concentrations superimposed upon background spectrum over 1.72-9.60 MeV taken with the BGO detector. The Ni(8533) and Ni(8998) nickel peaks , are quite prominent.

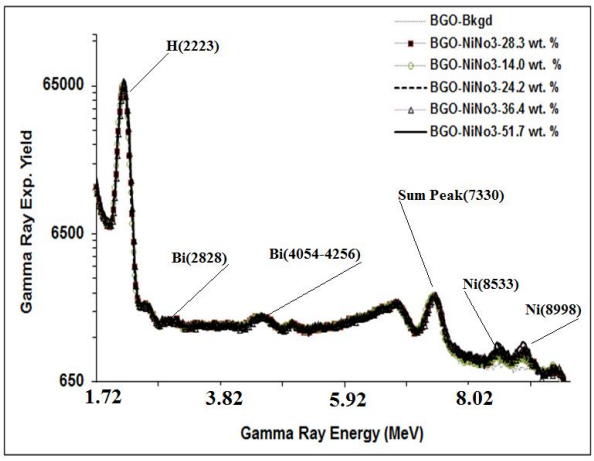

Figure 4.33: Prompt gamma-rays pulse height spectra of water samples contaminated with 20-51.7 wt % nickel nitrate $Ni(NO_3)_2$ over 1.67-9.60 MeV energy range superimposed upon background spectrum.

Figures 4.34 and 4.35 show the enlarged pulse height spectra of prompt gamma-rays from nickel-contaminated water samples. Figure 4.34 shows the nickel-contaminated water samples pulse height spectra superimposed upon each other along with beam associated-background spectrum taken with a pure water sample over 8.26-9.31 MeV energy. Figure 4.35 shows the enlarged difference spectra (background subtracted**)** of nickel peaks over 8.26-9.31 MeV energy. Figures 4.34 and 4.35 show barely resolved Ni(8533) and Ni(8998) nickel peaks.

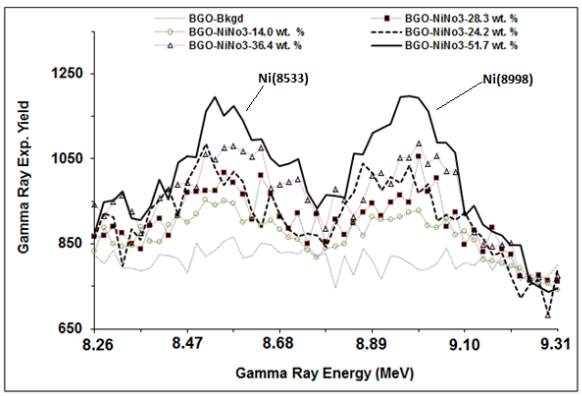

Figure 4.34: Prompt gamma-rays pulse height spectra of water samples contaminated with 20-51.7 wt % nickel nitrate $Ni(NO_3)_2$ over 1.67-9.60 MeV energy range superimposed upon background spectrum.

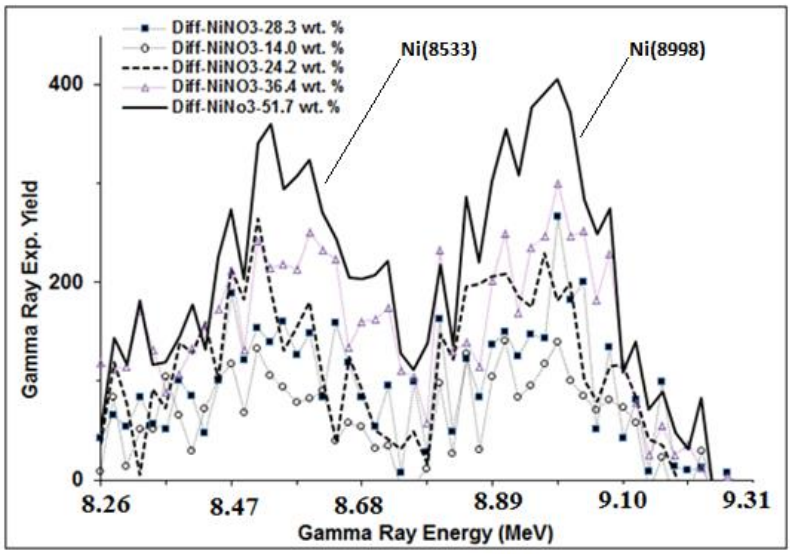

Figure 4.35: Difference pulse height spectra of water samples contaminated with 20-51.7 wt % nickel nitrate $Ni(NO_3)_2$ contaminated water sample.

4.5 Results and Discussion

Finally, integrated yield of boron, mercury, cadmium, chromium, nickel and chlorine samples gamma ray spectra were calculated by integrating the difference spectra peaks. The integrated yield data was normalized to the same neutron flux and data acquisition time. Fig. 4.36 shows the integrated yield from difference spectra of boron, cadmium and mercury-contaminated water samples as a function of boron, cadmium and mercury element concentration in water samples. The lines in Fig. 4.36 represents results of calculated yield of prompt gamma-ray obtained from Monte Carlo calculations following the procedure described elsewhere [62]. There is an excellent agreement between the theoretical yield and the experimental yield of prompt gamma-ray from boron, cadmium and mercury samples measured by $CeBr_3$ detector as a function of concentration of the respective element in water samples.

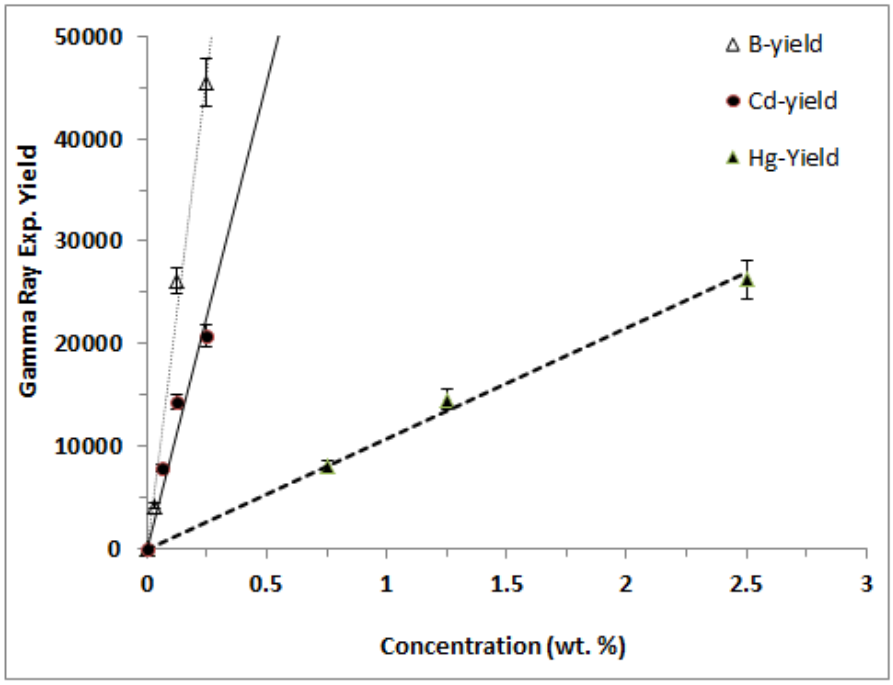

Figure 4.36: Integrated yield of Hg(368), B(478) and Cd(558) keV prompt gamma-rays from mercury, boron and cadmium contaminated water samples plotted as a function of mercury, boron and cadmium concentration respectively. The solid line shows normalized-calculated yield of the gamma-rays obtained through Monte Carlo calculations.

Then integrated yield of chromium and nickel gamma ray spectra were calculated by integrating the difference spectra of Cr(8483, 8511) , Cr(8884) , Cr(9719) peaks , Ni(8533) and Ni(8998) nickel peaks. The integrated yield data was normalized to the same neutron flux and data acquisition time. Figure 4.37 and 4.38 shows the integrated yield from difference spectra of chromium and nickel-contaminated water samples as a function of chromium and nickel elemental concentration in these water samples.

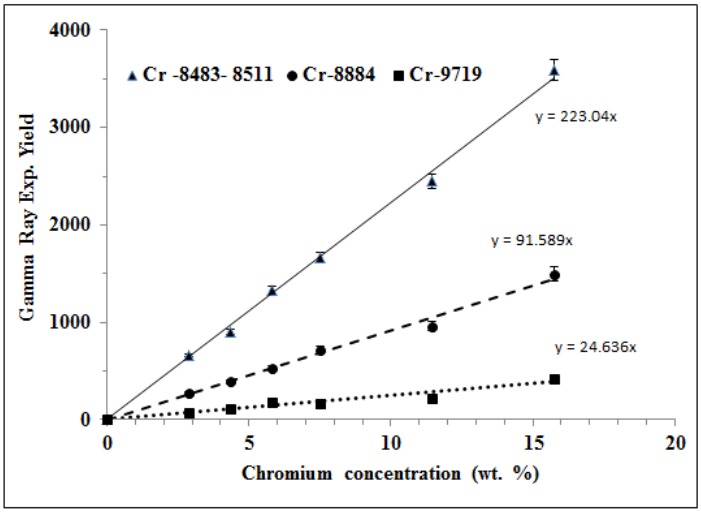

Figure 4.37: Experimental yield of Cr(7938), Cr(8511), Cr(8884) and Cr(9719) prompt gamma rays from chromium measured by the $CeBr_3$ detector plotted as a function of chromium concentration in water samples. Data is fitted with Monte Carlo simulations results shown as lines.

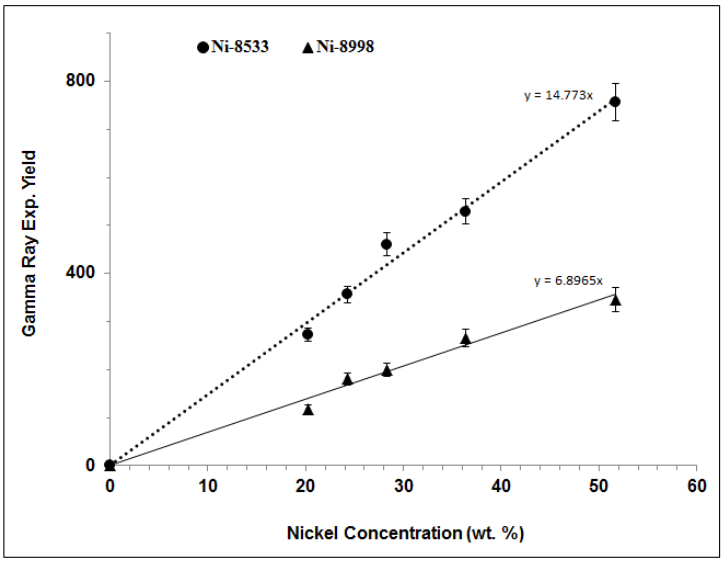

Figure 4.38: Experimental yield of Ni(8533) and Ni(8998) prompt gamma rays from nickel measured by the $CeBr_3$ detector plotted as a function of nickel concentration in water samples. Data is fitted with Monte Carlo simulations results shown as lines.

The lines in Fig. 4.37 represent results of calculated yield of prompt gamma-ray obtained from Monte Carlo calculations for the chromium-contaminated water samples following the procedure described elsewhere [62]. The lines in Fig. 4.38 represent results of

calculated yield of prompt gamma-ray obtained from Monte Carlo calculations for the nickel-contaminated water samples. The experimental results and the results of Monte Carlo calculation are in good agreement in Figures 4.37 and 4.38 within experimental uncertainties.

Figs. 4.39-4.40 show integrated gamma rays yield of the eight chlorine gamma rays as a function of chlorine concentration in saline water samples. Experimental data points for each gamma ray line are superimposed on calculated yield of the respective gamma ray. There is an excellent agreement between the experimental results and results of Monte Carlo calculations.

Fig. 4.39 shows the integrated yield of 517, 788, 1165 and 1951 keV gamma rays as a function of chlorine concentrations in saline water samples. Among this group of chlorine gamma rays, maximum slope of the gamma ray line has been observed for 517 keV gamma ray line while minimum slope for 1951 keV gamma ray line.

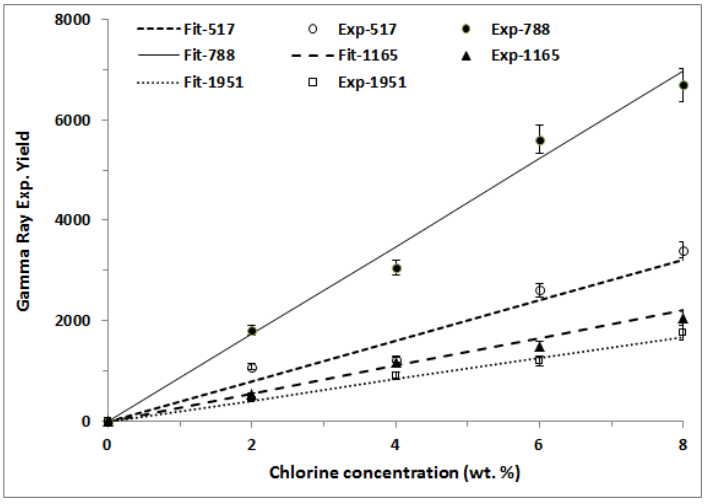

Figure 4.39: Integrated intensity of 517, 788, 1165 and 1951 KeV chlorine peaks from saline water samples plotted as a function of chlorine concentration of the saline water sample over 0- 8 wt. % chlorine concentration. The lines are results of Monte Carlo Simulation.

Fig. 4.40 shows the integrated yield of 2863, 6110 and 6619 and 8578 keV chlorine gamma rays as a function of chlorine concentrations in saline water samples. Among this group of chlorine gamma rays, maximum slope of the gamma ray line has been observed for 2863 keV gamma ray line while minimum slope has been observed for 6610 keV gamma ray line.

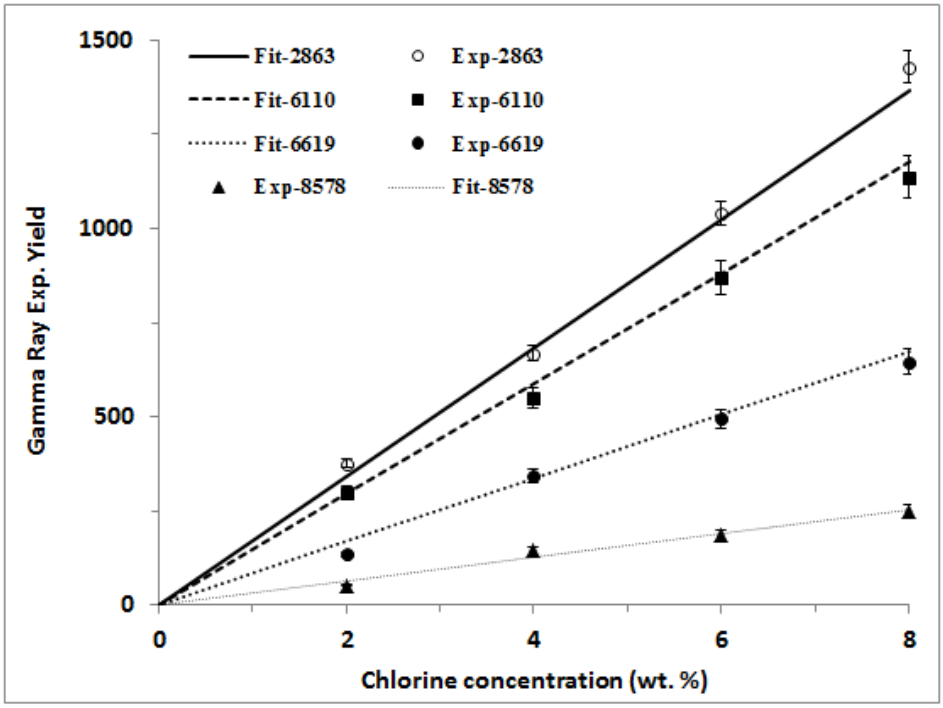

Figure 4.40: Integrated intensity of 2863, 6110, 6619 and 8578 KeV chlorine peaks from saline water samples plotted as a function of chlorine concentration of the saline water sample over 0- 8 wt. % chlorine concentration. The lines are results of Monte Carlo Simulation.

Figure 4.41 and 4.42 shows the integrated yield from difference spectra of chromium and nickel-contaminated water samples as a function of chromium and nickel elemental concentration in these water samples.

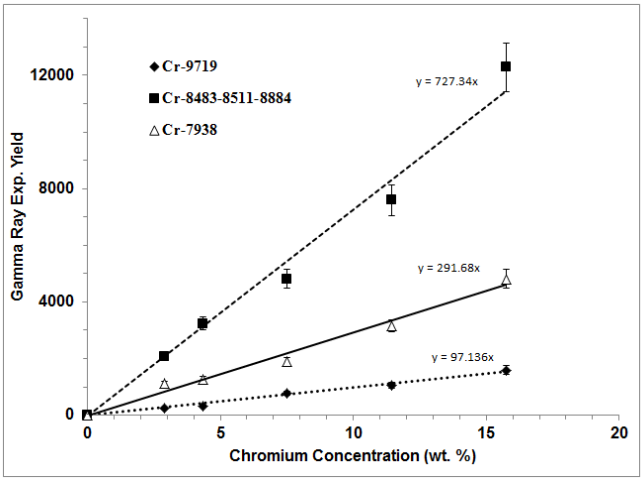

Figure 4.41: Experimental yield of Cr(7938), Cr(8483, 8511, 8884) and Cr(9719) prompt gamma rays from chromium measured by the BGO detector plotted as a function of chromium concentration in water samples. Data is fitted with Monte Carlo simulations results shown as lines.

The lines in Fig. 4.41 represent results of calculated yields of prompt gamma-ray obtained from Monte Carlo calculations for the chromium-contaminated water while the lines in Fig. 4.42 represent results of Monte Carlo calculations for the nickel-contaminated water samples. The experimental results and the results of Monte Carlo calculation are in good agreement within experimental uncertainties.

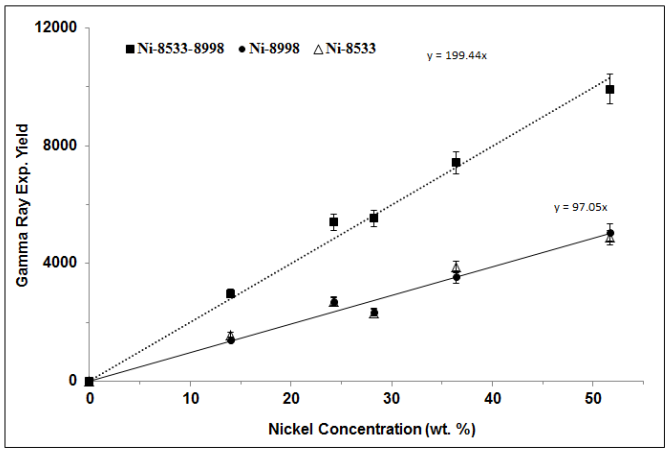

Figure 4.42: Experimental yield of Ni(8533) and Ni(8998) prompt gamma rays from nickel measured by the BGO detector plotted as a function of nickel concentration in water samples. Data is fitted with Monte Carlo simulations results shown as lines.

4.5.1 Minimum Detection Limits of Boron, Cadmium, Mercury, Chlorine, Chromium and Nickel in Water Samples using $CeBr_3$ Detector

The minimum detection limit (MDC) of KFUPM portable neutron generator-based PGNAA setup was determined for the 76 mm x 76 mm $CeBr_3$ detector based system. The detection limit for an elemental concentration MDC measured under a peak with net counts P and associated background counts B (under the peak) can be approximated using the equation [63]

$$MDC = 3.29C \left\{ \sqrt{\left[\left(1+\frac{\eta_p}{\eta_B}\right)\right]} \Big/ \sqrt{\left[t'\left(\frac{P}{B}\right)\left(\frac{P}{t}\right)\right]} \right\}$$

where C is the element's concentration in the peak, t′ is the counting time, P/t is net count rate, and η_P and η_B are the number of channels used to integrate the peak and background areas to calculate P and B counts. If η_P and η_B are equal and t′ and t are equal then the equation reduces to:

$$MDC = 4.653\left(\frac{C}{P}\right)\sqrt{B}$$

where C/P is concentration (wt%)/counts, i.e. the calibration constant of the setup for a specific gamma ray peak. This is the Currie Equation of Minimum Detection Limit (MDL) of counts given by Knoll [64], with counts converted into element concentration.

The error in MDC i.e.

$$\sigma_{MDC} = \left(\frac{C}{P}\right)\sqrt{2B}$$

For 90 mm x 140 mm (diameter x height) cylindrical water sample, the measured minimum detection limit MDC and its standard deviation σ_{MDCB} for boron, mercury and cadmium are listed in Table 4.2. For comparison sake MDC data of 76 mm x 76 mm cylindrical $LaBr_3$:Ce detector [4] has also been included in Table 4.2.

For the $CeBr_3$ detector, the measured values of minimum detection limit MDC_B and σ_{MDCB} are 24.4 ppm and 7.43 ppm respectively. Compared to a $LaBr_3$:Ce detector of equivalent volume, the $CeBr_3$ detector has 23 % higher detection sensitivity. This improvement might be due to absence of lanthanum contamination in $CeBr_3$ detector and absence of its associated interfering peaks in background peaks at La(487) closely interfering boron B(478) peak.

For the $CeBr_3$ detector, the measured values of minimum detection limit of cadmium MDC_{Cd} and σ_{MDCCd} are 95.6 ppm and 29.1 ppm respectively. The detection sensitivity MDC_{Cd} of the $CeBr_3$ detector is 18 % poorer than that the a $LaBr_3$:Ce detector. Although due to absence of interference of La(549) and La(567) in the background spectrum of $CeBr_3$ detector , it was expected to have improved detection sensitivity for the cadmium detection. Due to excessive doping of Ce in $CeBr_3$ deteriorated the energy resolution hence decreasing the detection sensitivity. This effect becomes more pronounced at higher energies.

For mercury detection, the measured values of minimum detection limit of mercury MDC_{Hg} and σ_{MDCHg} are 0.15 wt. % and 0.05 wt. % respectively. The detection sensitivity of the detector for the mercury is quite poor due to complete overlap of Hg(368) peak with Br(367) and Br(389) peaks in the detector background.

Minimum detection limit (MDC) values for 0.5-8.58 MeV Chlorine Gamma Rays are measured in wt. % range due to the weak thermal neutron flux from the 2.5 MeV portable neutron generator-high density polyethylene - moderator setup. For the 106 mm x 125 mm (diameter x height) cylindrical water samples, the measured minimum detection limits MDC and their standard deviations for eight chlorine prompt gamma rays with 517, 788, 1165, 1951, 2863, 6110, 6619 and 8578 keV energies varies from 1.75 wt % to 4.20 wt. %. The detailed MDC values for each gamma ray along with its standard deviation σ_{MDC} are listed in Table 4.2.

For the $CeBr_3$ based PGNAA setup the optimum values of MDC$\pm\sigma_{MDC}$ have been measured to 1.47 $\pm$0.45 and 1.75$\pm$0.53 wt % respectively for 1951/1959 and 788 keV chlorine gamma rays. Although there are gamma rays with higher intensities such as 517 keV and 6110 keV but they have poorer values of MDC i.e 3.48$\pm$1.06 and 2.34$\pm$0.71 respectively. Within standard the error ($\pm\sigma$) limits, value of MDC for 6110, 6619 and 8578 keV gamma rays keV overlaps with our optimum values of MDC for 1951/1959 and 788 keV chlorine gamma rays. Larger values of MDC of 3.48 wt % - 4.20 wt. % have been measured for 517, 1165 and 2863 keV.

The smaller values of MDC have been measured for those gamma rays with higher intensities and relatively smaller background under the gamma ray peak. Similarly, larger values of the MDC have been observed for less intense peaks or peaks having higher background underneath due to gamma rays produced from $CeBr_3$ detector material. Inspite of large production cross section of 7.58 barn and 8.91 barn, the MDC for 517 and 1165 keV chlorine gamma rays have larger values of 3.48 and 3.87 wt % respectively. This is

due to strong interference of Br(513) gamma ray with Cl(517) gamma ray and interference of Ce(1107) gamma ray with Cl(1165) gamma rays.

A comparison of the MDC values of the various chlorine gamma rays in the low energy range reveals that the optimum choice of gamma ray energy for chlorine detection may be either 1951 keV or 788 keV gamma ray with corresponding MDC of 1.47±0.45 and 1.75±0.53 respectively. In the higher energy range the optimum choice of gamma ray energy is 6110 keV or 6619 keV gamma ray with MDC values of 2.34±0.71 and 2.41±0.73 respectively.

For an Am–Be source based PGNAA setup, Khelifi et al have reported a value of MDC of 22.3 ppm for 6110 keV chlorine gamma ray for detection of chlorine in water samples [65]. In this study, an Am–Be source with much higher neutron flux than our neutron generator was used.

This study has provided useful data on MDC values of chlorine gamma rays for a large volume $CeBr_3$ detector based PGNAA setup utilizing a portable neutron generator.

The measured minimum detection limits MDC and their standard deviations σ_{MDC} for chromium and nickel samples are listed in Table 4.2 for the $CeBr_3$ and the BGO detectors. For both the detectors, MDC values were calculated for both resolved and un-resolved gamma ray peaks. For the $CeBr_3$ detector, MDC was calculated for unresolved Cr(8483, 8511) peaks while for the BGO detector, MDC was calculated for unresolved Cr(8483, 8511, 8884) peaks and Ni(8533, 8998) peaks.

For chromium detection the minimum detection limit MDC_{Cr} and $\sigma_{MDC\text{-}Cr}$ are 1.03 wt. % and 0.31 wt. % respectively have been measured for the $CeBr_3$ detector using Cr(8483, 8511) gamma rays . For the BGO detector the minimum detection limit MDC_{Cr} and $\sigma_{MDC\text{-}Cr}$ are 1.95 wt. % and 0.59 wt. % respectively have been measured for the Cr(8483, 8511, 8884) gamma rays. For nickel detection the minimum detection limit MDC_{Ni} and $\sigma_{MDC\text{-}Ni}$ are 1.98 wt. % and 0.60 wt. % respectively have been measured for the $CeBr_3$ detector using Ni(8533) gamma rays . For the BGO detector the minimum detection limit MDC_{Ni} and $\sigma_{MDC\text{-}Ni}$ are 4.72 wt. % and 1.43 wt. % respectively have been measured for the Ni(8533-8998) gamma rays.

Comparison the minimum values of MDC values of chromium and nickel for both the $CeBr_3$ and the BGO detector have revealed that inspite of almost 3 times poorer energy resolution of the BGO detector (4 % for the $CeBr_3$ detector as compared to 11 % for BGO detector at 661 keV gamma rays) as compared to the superior $CeBr_3$ detector, the MDC values of the BGO detector for chromium and nickel are about 2-2.4 times poorer than those of the superior $CeBr_3$ values.

Table 4.2: Minimum detection limit (MDC) of boron, cadmium, mercury, chromium, nickel and chlorine in water samples using $CeBr_3$, BGO and $LaBr_3$:Ce [4] detector based PGNAA setup.

Element	Eγ(keV)	$CeBr_3$ Detector		BGO (3″ x 3″)		$LaBr_3$:Ce Detector [4]	
		MDC(wt.%)	σ_{MDC}(wt.%)	MDC(wt.%)	σ_{MDC}(wt.%)	MDC	σ_{MDC}
Cr	7938	-	-	2.70	0.82	-	-
	8483-8511*	1.03	0.31	-	-	-	-
	8483-8511-8884*	-	-	1.95	0.59	-	-
	8884	1.41	0.43	-	-	-	-
	9719	2.98	0.91	-	-	-	-
Ni	8533	1.98	0.60	6.77	2.06	-	-
	8998	3.88	1.18	6.58	2.00	-	-
	8533-8998*	-	-	4.72	1.43	-	-
Cl	517	3.48	1.06	-	-	-	-
	788	1.75	0.53	-	-	-	-
	1165	3.87	1.18	-	-	-	-
	1951	1.47	0.45	-	-	-	-
	2863	4.20	1.28	-	-	-	-
	6110	2.34	0.71	-	-	-	-
	6619	2.41	0.73	-	-	-	-
	8578	2.81	0.81			-	-
B	478	24.4 Ppm	7.43 Ppm	-	-	30.1 ppm	9.3 ppm
Cd	558	95.6 Ppm	29.1 Ppm	-	-	78.3 ppm	23.8 ppm
Hg	368	0.15 wt%	0.05 wt%	-	-	-	-

*MDC calculation over unresolved peaks by taking total counts under the region of peaks.

CHAPTER 5

PROMPT GAMMA ANALYSIS OF MOISTURE (WATER)-AND BENZENE-CONTAMINATED SOIL SAMPLES

The moisture and petroleum (benzene) contamination effect on yield of silicon, carbon, oxygen, and hydrogen prompt gamma rays was studied from soil samples containing different water and benzene proportion via neutron inelastic scattering (NIS) using 14 MeV neutrons based PGNAA setup. The prompt gamma rays were produced using 14 MeV neutron beams and were detected using a $LaBr_3$:Ce gamma ray detector.

5.1 Experimental Setup

The prompt gamma ray spectra from the soil samples and standards were recorded using the 14 MeV neutron based PGNAA setup shown in Fig. 5.1. The setup is located at the end of the zero-degree beam line located in a reinforced concrete shielded room. It mainly consists of a cylindrical sample 106 mm x 125 mm (diameter x height) dimensions placed 7.0 cm away from a tritium target at a 0^o angle with respect to the 14 MeV neutron beam. A cylindrical 76 mm x 76 mm (diameter x height) $LaBr_3$:Ce detector, placed at a center-to-center distance of 125 mm from the sample, detects the gamma rays from the sample at an angle of 90° with respect to the 14 MeV neutron beam axis. The detector was shielded against 14 MeV neutrons and gamma rays through tungsten and lead shielding respectively. The tungsten blocks are placed between the target and the gamma ray detector to prevent detector from direct beam of 14 MeV neutrons. Lead blocks inserted between the detector

and tungsten shield to prevent 14 MeV neutron-induced gamma ray background. Paraffin was placed next to the tungsten blocks to shield the detector from concrete room scattered neutrons. The paraffin shield is a mixture of lithium carbonate and paraffin wax in equal weight proportions.

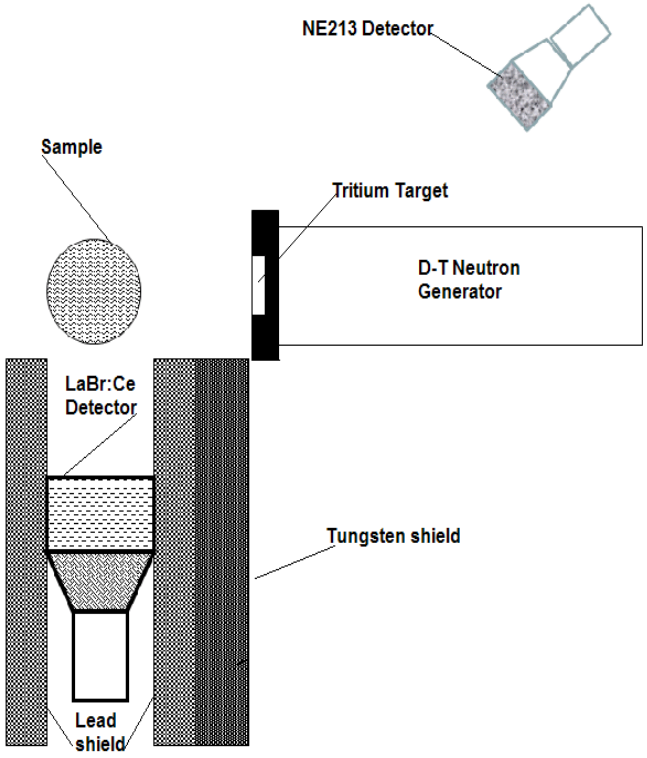

Figure 5.1: Schematic of 14 MeV neutron-based setup used for analysis of soil bulk samples.

5.2 Sample Preparation

In this study, the soil samples were prepared by mixing 1863.8 g of dry soil with 5.1, 7.4, 9.7, 11.9 and 14.0 wt.% moisture (water) shown in Table 5.1. The soil and water were thoroughly mixed together and soil completely absorbed the water. Then, the dry soil and as well as soil mixed with moisture samples were filled in plastic containers with 106 mm

x 125 mm (diameter x height) dimensions. However, the benzene samples were also prepared by mixing 1863.8 g of dry soil with 2.2, 4.4, 6.5, 8.5 and 10.4. wt.% benzene. The soil and benzene were thoroughly mixed together and soil completely absorbed the benzene. Then, the dry soil and as well as soil mixed with benzene samples were filled in plastic containers with 106 mm x 125 mm (diameter x height) dimensions.

Table 5.1: Concentrations of Moisture and Benzene Samples Mixed in Soil

Sample	Concentrations (wt. %)
Moisture	**5.1, 7.4, 11.9 and 14.0 wt.%**
Benzene	**2.2, 4.4, 6.5, 8.5 and 10.4. wt.%**

5.3 Prompt Gamma Ray Analysis of Contaminated Soil Samples Using $LaBr_3$:Ce Detector.

The prompt gamma ray analysis of contaminated soil samples were recorded using the 14 MeV neutron based PGNAA setup described section 5.1. A pulsed beam of 14 MeV neutrons was produced via the T(d, n) reaction using a pulsed 110 keV deuteron beam with 200 ns pulse width and a frequency of 31 kHz. Pulsed ion beams are produced in the pre-acceleration stage of the KFUPM 350 keV accelerator using a diverter system. 200 ns pulses of 26 keV deuteron dc beams are produced by deflecting the dc deuteron beam across a water-cooled aperture through a 2000 V voltage pulse of 200 ns duration and 31 kHz frequency, directly applied across the deflector plates of the diverter system.

The typical pulsed beam current of the accelerator was 60 μA averaged over the duty cycle of the 350 keV accelerator. The fast neutron flux from the tritium target was monitored using a cylindrical 76 mm x 76 mm (diameter x height) NE213 fast neutron detector, placed

at a distance of 1.8 m from the target and making an angle of 130° with respect to the beam. The neutron flux spectrum was recorded through the proton recoil spectrum of the NE213 liquid scintillation detector during each run. In neutron spectroscopy, neutron detectors are operated at a specific discrimination level to suppress background neutrons and gamma ray signals. Therefore, the neutron detector signals are acquired in coincidence with a single channel analyzer SCA whose lower level is set at a fixed gamma-ray energy (also neutron energy). The neutron detector signals were acquired through a single channel analyzer, whose lower level was set at half-Cs pulse height bias that was electronically set by using the half-height of Compton edge spectrum of the ^{137}Cs gamma ray source.

The neutron spectrum counts were integrated for each run and were used later on for neutron flux normalization. The prompt gamma-ray spectra of the $LaBr_3$:Ce detector were recorded for a preset real time. The neutron and gamma ray detectors' spectra were acquired with a PC-based data acquisition system utilizing fast multichannel ADC buffer module 'ETHER-NIM 90E' manufactured by EG&G-ORTEC. The module utilizes Scintivision software to analyze the pulse height spectra of the detectors. Each detector spectrum was acquired in 512 channels.

For prompt gamma ray analysis, empty and filled sample containers were then irradiated in the 14 MeV neutron-based PGNAA setup. The prompt gamma-ray data from the samples were acquired for 20–30 min. The typical dead-time of the pc-based data acquisition system was less than 1%. The empty container measurements were only repeated a few times because they had almost a constant spectrum. The empty container spectrum was used later on for background subtraction. The prompt gamma-ray data from the samples were acquired using the personal computer-based data acquisition system described earlier.

For the identification of high-energy silicon, carbon, oxygen and hydrogen gamma ray peaks in the soil sample spectrum, gamma ray yields from samples with known elemental composition such as silica fume, benzene and water samples were recorded. For the identification of the silicon peak, the gamma ray spectrum was recorded from the silica fume, which contains 43.2 wt. % concentration of silicon [49]. For the carbon peak identification, gamma ray spectrum was recorded from pure benzene sample which contained 92.3 wt. % carbon. Similarly, for identification of hydrogen and oxygen peaks water samples were used.

5.3.1 Moisture Contaminated Soil Samples Data

Fig. 5.2 shows the spectrum of a dry soil sample superimposed upon a background spectrum taken with an empty container spectrum over 0.59–6.87 MeV range. The 1.78 MeV gamma ray peak from silicon and the 6.13 MeV peak from oxygen are quite prominent, along with the 789 and 1468 keV intrinsic peaks of lanthanum, 1.07 MeV as well as 2.62 MeV peak from lead shielding.

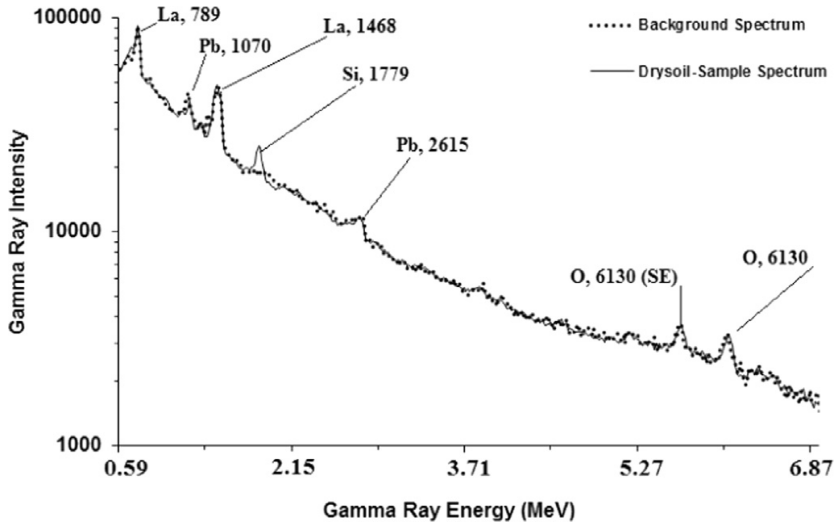

Figure 5.2: Prompt gamma ray spectra of dry soil sample superimposed upon background spectrum and plotted over 0.59–6.87 MeV energy range.

Fig. 5.3 shows the prompt gamma ray spectra of silica fume and water samples superimposed over the 1.59–2.92 MeV range showing 1.78, 2.22, 2.09 and 2.62 MeV prompt gamma rays from silicon, hydrogen and lead (shielding material), respectively. The Single Escape peak (SE) corresponding to the 2.62 MeV full energy peak of lead is also shown in Fig. 5.3.

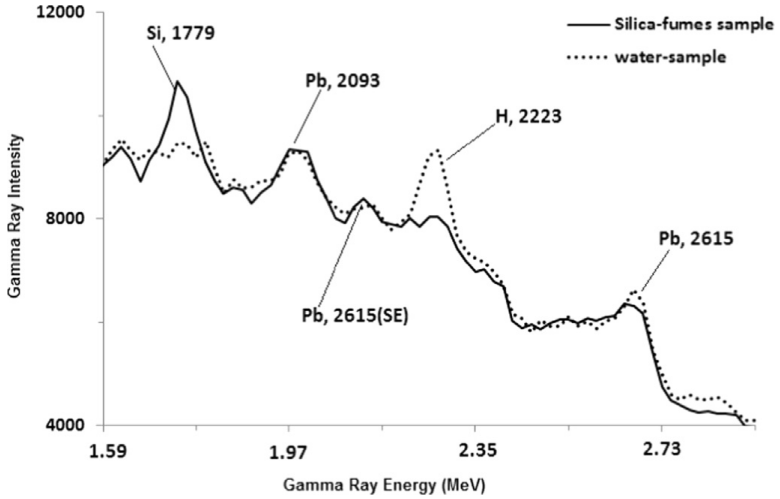

Figure 5.3: Prompt gamma ray spectrum of silica fume sample superimposed upon water sample and plotted over 1.59–2.92 MeV energy range.

After the identification of silicon and oxygen prompt gamma ray peaks in the gamma ray spectrum, gamma ray spectra from dry soil and soil mixed with 5.1, 7.4, 11.9 and 14.0 wt.% moisture were recorded to study the effect of moisture using the PGNAA setup. In order to show the effect of moisture on silicon, hydrogen, and oxygen prompt gamma ray intensity, enlarged soil spectra containing 5.1–14 wt.% moisture are superimposed upon a dry soil sample spectrum, as shown in Figs. 5.4–5.6. Fig. 5.4 shows enlarged soil spectra containing 5.1–14.0 wt.% moisture over 1.65–1.95 MeV range showing 1.78 MeV gamma ray peaks from silicon. Effects of moisture on gamma ray intensity is quite significant and the intensity of 1.78 MeV Si gamma rays decreases with increasing moisture concentration, with its maximum intensity observed for the dry soil sample.

Fig. 5.5 shows the 2.22 MeV hydrogen peak along with lead 2.09 MeV peak along with the single escape (SE) peak of lead 2.62 MeV full energy peak plotted over 1.95–2.55 MeV energy range for samples containing 5.1–14.0 wt% moisture. The increasing trend of the hydrogen peak intensity with increasing moisture concentration is quite prominent.

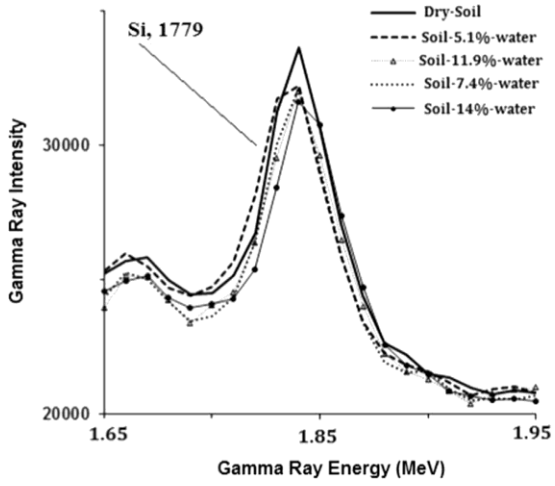

Figure 5.4: Enlarged prompt gamma ray spectra of soil samples containing 5.1–14 wt% moisture superimposed upon dry soil sample plotted over 1.65–1.95 MeV energy range showing silicon peak.

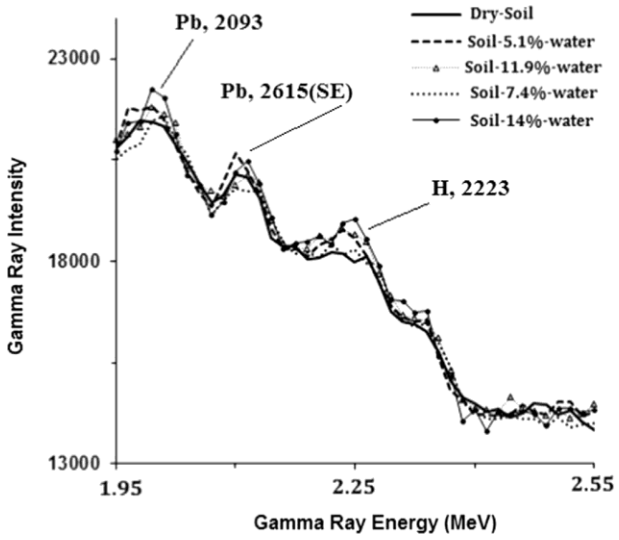

Figure 5.5: Enlarged prompt gamma ray spectra of soil samples containing 5.1–14 wt% moisture superimposed upon dry soil sample and plotted over 1.95–2.55 MeV energy range, showing hydrogen and lead peaks.

Fig. 5.6 shows the 6.13 MeV oxygen full energy peak on an enlarged scale plotted over 5.92–6.24 MeV energy range for samples containing 5.1–14.0 wt% moisture concentration. The decreasing peak intensity of the 6.13 MeV oxygen full energy peak with increasing moisture concentration is clearly visible in Fig. 5.6.

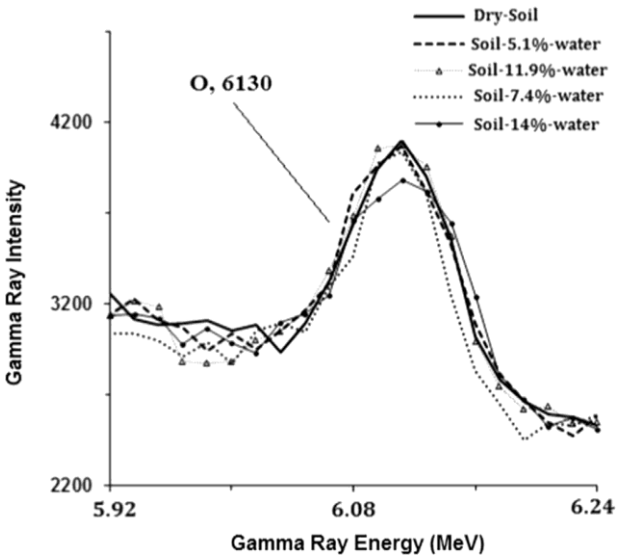

Figure 5.6: Enlarged prompt gamma ray spectra of soil samples containing 5.1–14 wt% moisture superimposed upon dry soil sample and plotted over 5.92–6.24 MeV energy range, showing oxygen full energy peak.

5.3.2 Benzene Contaminated Soil Samples Data

Figure 5.7 shows the prompt gamma ray spectra from pure benzene and pure water samples superimposed upon each other over 0.09-6.49 MeV range. The 4.44 and 2.22 MeV gamma ray peaks from carbon and hydrogen, respectively, are quite prominent in Fig. 5.7 along with 6.13 MeV peaks from oxygen. Figure 5.8 shows the prompt gamma spectra of pure silica fume and pure water samples superimposed over the 0.76-8.20 MeV range showing 1.78, 2.22 and 6.13 MeV prompt gamma rays from silicon, hydrogen and oxygen respectively. Also shown in the Fig. 5.8 is lead Pb peak from the shielding material.

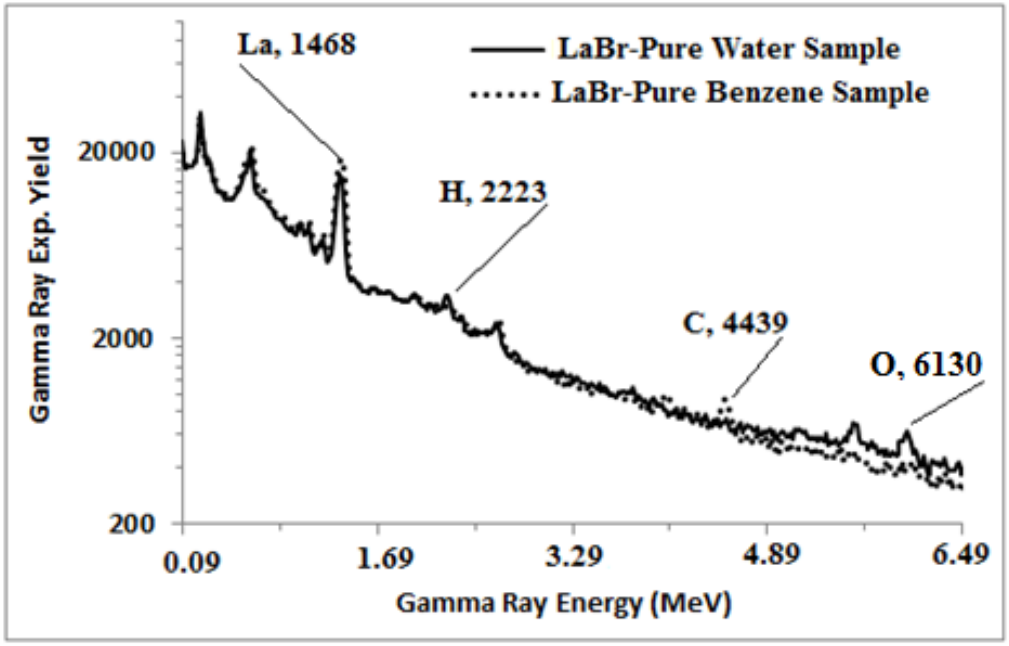

Figure 5.7: Prompt gamma ray spectra of pure benzene and pure water bulk samples superimposed upon each other over 0.09 to 6.49 MeV energy range, showing carbon, hydrogen and oxygen peaks.

After the identification of silicon, hydrogen, carbon and oxygen prompt gamma ray peaks in the gamma ray spectrum, gamma ray spectra from dry soil and soil mixed with 2.2, 4.4, 6.5, 8.5 and 10.4 wt. % benzene were recorded to study the effect of petro-hydrocarbon contamination using the PGNAA setup. The prompt gamma-ray data from the samples

were acquired for 20-30 minutes. Figure 5.9 shows the pulse height spectra of soil samples containing 2.2, 4.4, 6.5, 8.5 and 10.4 wt. % benzene concentration superimposed upon a spectrum of dry soil sample over 0.50-6.90 MeV energy range.

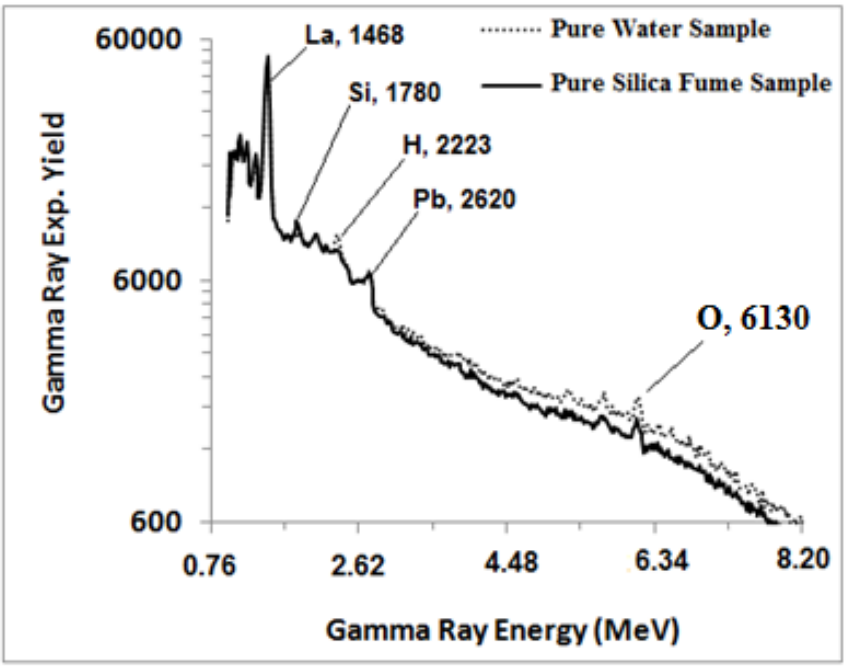

Figure 5.8: Prompt gamma ray spectra of LaBr3:Ce gamma ray detector from pure silica fume, and pure water bulk samples superimposed upon each other plotted over 0.76 to 8.20 MeV energy range , showing silicon, hydrogen and oxygen peaks.

In order to show the effect of benzene concentration on silicon, carbon, hydrogen, and oxygen prompt gamma ray yields, enlarged soil samples spectra for silicon, carbon, hydrogen, and oxygen gamma ray are plotted in Figs. 5.10- 4.13 respectively.

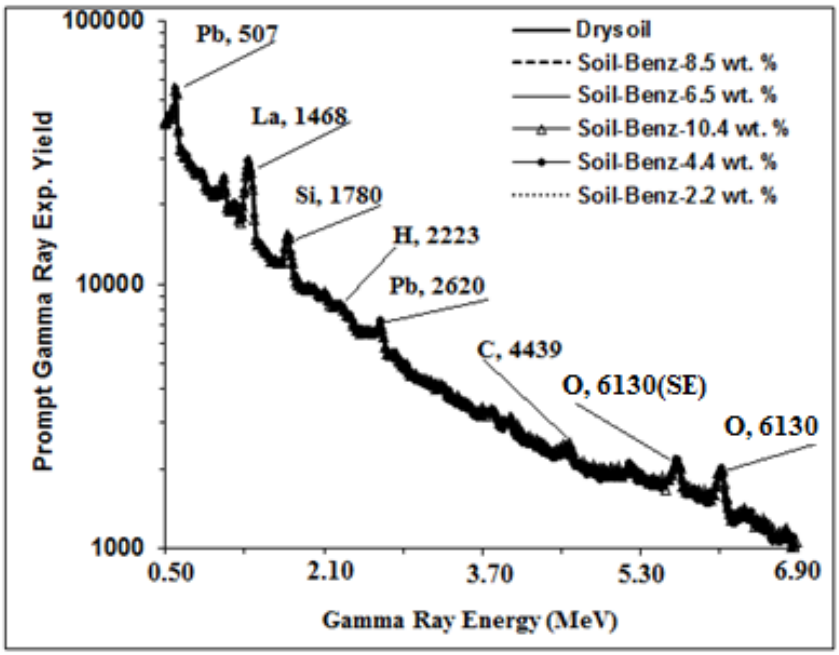

Figure 5.9: Prompt gamma ray spectra of soil samples containing 2.2-10.4 wt.% benzene plotted over 0.50 to 6.90 MeV superimposed upon dry soil sample spectrum and showing silicon, carbon, oxygen, hydrogen and lead peaks.

Figure 5.10 shows enlarged 1.78 MeV silicon peak spectra from soil samples containing 2.2, 4.4, 6.5, 8.5 and 10.4 wt. % benzene concentration along with dry soil sample over 1.66-2.41 MeV. Effects of benzene concentration on silicon gamma ray yields are quite significant and the yield of 1.78 MeV silicon gamma rays decreases with increasing benzene concentration, with its maximum yield observed for the dry soil sample.

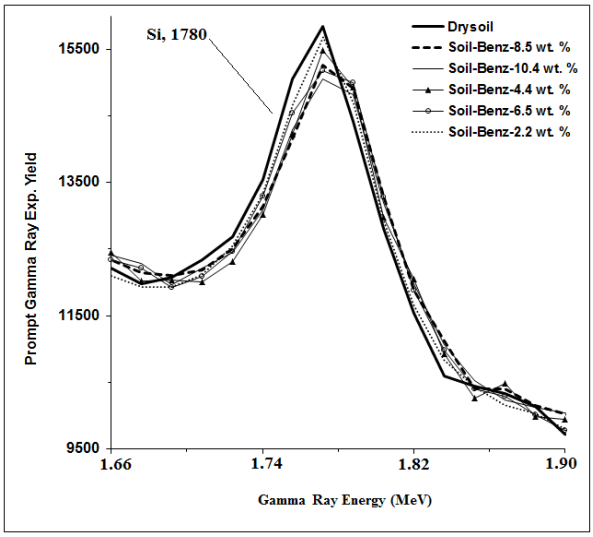

Figure 5.10: Silicon prompt gamma ray spectra of soil samples containing 2.2-10.4 wt.% benzene shown on enlarged scale over 1.66-1.90 MeV and superimposed upon dry soil sample spectrum.

Figure 5.11 shows enlarged 4.44 MeV carbon peak spectra from soil samples containing 2.2, 4.4, 6.5, 8.5 and 10.4 wt. % benzene concentration along with dry soil sample over 4.20-4.68 MeV energy range. Effects of benzene on carbon gamma ray yields is quite significant and the yield of 4.44 MeV carbon gamma rays increase with increasing benzene concentration, with its maximum yield observed for the soil sample with 10.4 wt. % benzene concentration.

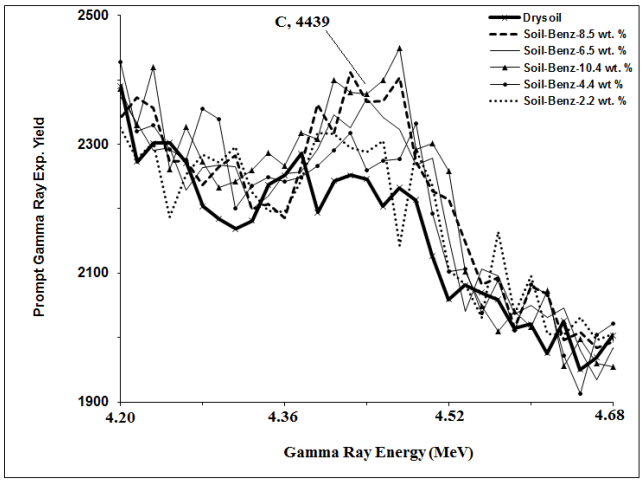

Figure 5.11: Carbon prompt gamma ray spectra of soil samples containing 2.2-10.4 wt.% benzene shown on enlarged scale over 4.20-4.68 MeV and superimposed upon dry soil sample spectrum.

Figure 5.12 shows the enlarged 6.13 MeV oxygen peak spectra from soil samples containing 2.2, 4.4, 6.5, 8.5 and 10.4 wt. % benzene concentration along with dry soil sample over 5.80-6.43 MeV. Effects of benzene on oxygen gamma ray yields is quite significant and the yield of 6.13 MeV oxygen gamma rays decreases with increasing benzene concentration, with its minimum yield observed for the soil sample with 10.4 wt. % benzene concentration.

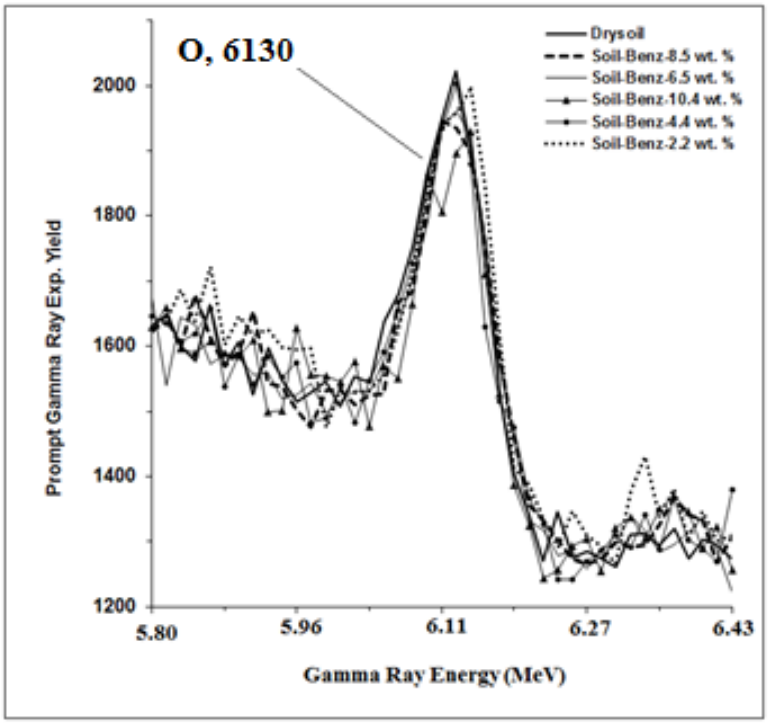

Figure 5.12: Oxygen prompt gamma ray spectra of soil samples containing 2.2-10.4 wt.% benzene shown on enlarged scale over 5.80-6.43 MeV and superimposed upon dry soil sample spectrum.

Figure 5.13 shows the enlarged 2.22 MeV hydrogen peak spectra from soil samples containing 2.2, 4.4, 6.5, 8.5 and 10.4 wt. % benzene concentration along with dry soil sample over 1.98-2.46 MeV. Effects of benzene on hydrogen gamma ray yields are not quite significant and gamma ray yield spectra for different benzene concentration are overlapping with each other.

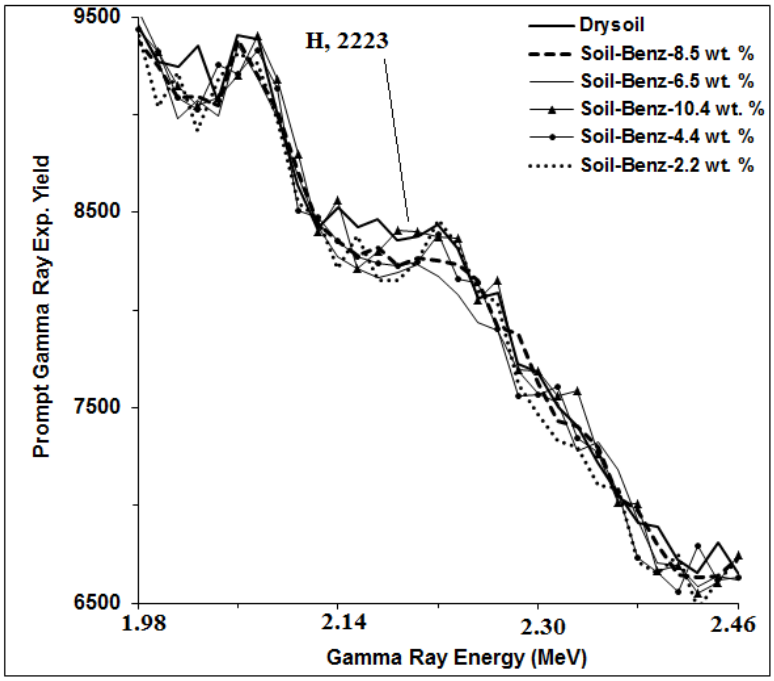

Figure 5.13: Hydrogen prompt gamma ray spectra of soil samples containing 2.2-10.4 wt.% benzene shown on enlarged scale over 5.80-6.43 MeV and superimposed upon dry soil sample spectrum.

5.4 Results and Discussion

The concentration of moisture was measured from moisture contaminated soil samples through $LaBr_3$:Ce detector using 14 MeV neutron inelastic scattering based PGNAA setup shown in Fig. 5.1. The background was subtracted under the 1.78 MeV Silicon, 4.44 MeV carbon, 6.13 MeV oxygen and 2.22 MeV hydrogen peaks spectrum by subtracting the background spectrum from the sample spectrum. For 6.13 MeV oxygen peaks the background under each peak was obtained by linear interpolation between two points, one on the lower energy side and the other on the higher energy side of the peak. The net counts under the peak were then obtained by integrating the counts in a window chosen on the background-subtracted peak. The net counts under each peak were further normalized to

the integrated counts of the NE213 neutron monitor spectra to correct for any variation in neutron flux.

The corrected net counts for 1.78 MeV Si, 2.22 MeV H, and 6.13 MeV O peaks were plotted as a function of sample moisture concentration and are shown in Figs. 5.14 and 5.15. Fig. 5.14 shows the integrated counts of the 1.78 MeV silicon peak and 6.13 MeV oxygen peak plotted as a function of sample moisture over 0.0–16.0 wt% concentration range. The fitted lines to the experimental data are the result of Monte Carlo calculations discussed in Section 2.2.3. Within the experimental uncertainties, the experimental results shown in Figs. 5.14 and 5.15 are in good agreement with the results of Monte Carlo calculation.

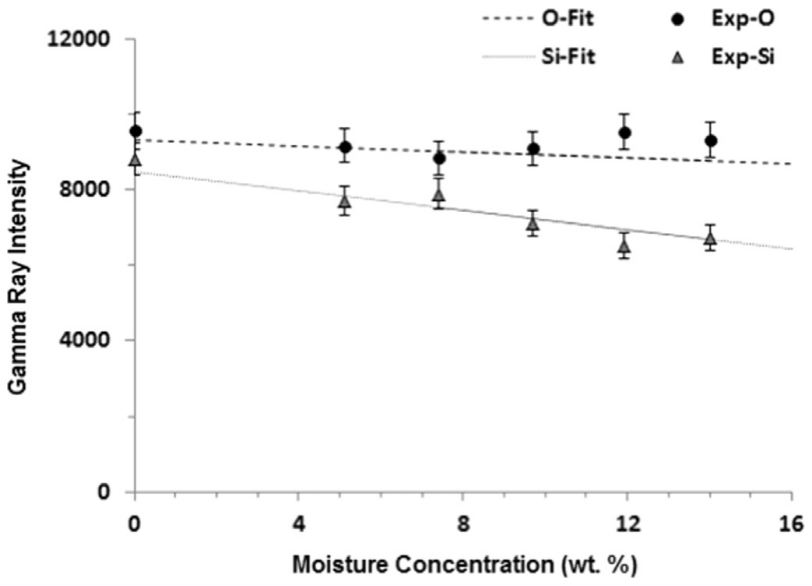

Figure 5.14: Integrated intensity of 1.78 MeV silicon peak and 6.13 MeV oxygen peak from soil samples plotted as a function of moisture concentration of the soil samples over 0–16 wt% moisture concentration. The fitted line are results of Monte Carlo simulations.

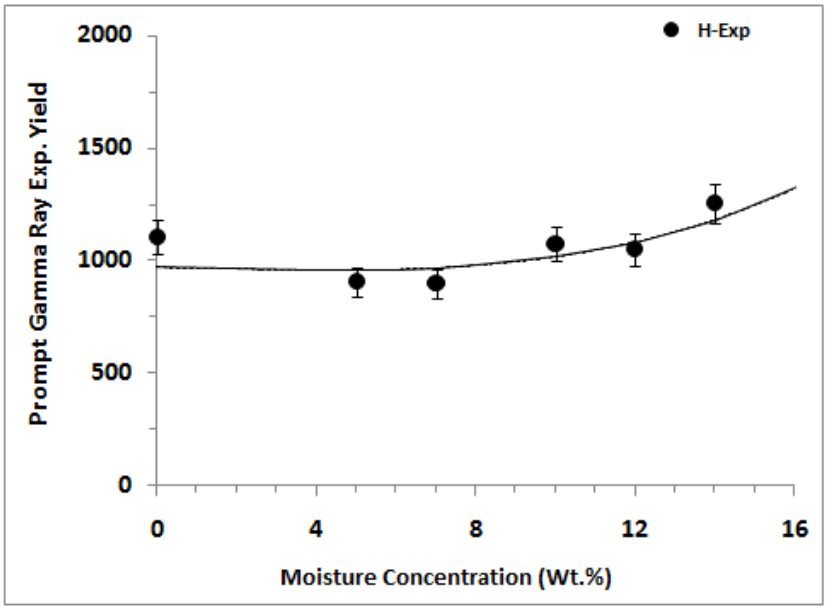

Figure 5.15: Integrated intensity of 2.22 MeV hydrogen peak from soil samples plotted as a function of moisture concentration of the soil samples over 0–16 wt% moisture concentration. The fitted line is results of Monte Carlo simulations.

The corrected net counts for the Si, C, O and H peaks were plotted as a function of sample benzene concentration and are shown in Fig. 5.16. Figure 5.16 shows the integrated yield of the 1.78 MeV silicon, 4.44 MeV carbon, 6.13 MeV oxygen and 2.22 MeV hydrogen peaks plotted as a function of soil sample benzene concentration over 0.0-10.4 wt. % range. As expected the yield of 4.44 MeV carbon gamma rays increases with benzene concentration. The yield of silicon and oxygen gamma rays decreases with increasing benzene concentration due to loss of 14 MeV neutron beam flux from scattering and moderation in benzene contents. The yield of hydrogen gamma rays is insensitive to increasing benzene concentration due to insignificant increase in hydrogen concentration with increasing benzene concentration. The lines fitted to the experimental data are the result of Monte Carlo calculations discussed in Section 2.2.4. Within the experimental

uncertainties, the experimental results shown in Figures 5.16 are in good agreement with the results of Monte Carlo calculation.

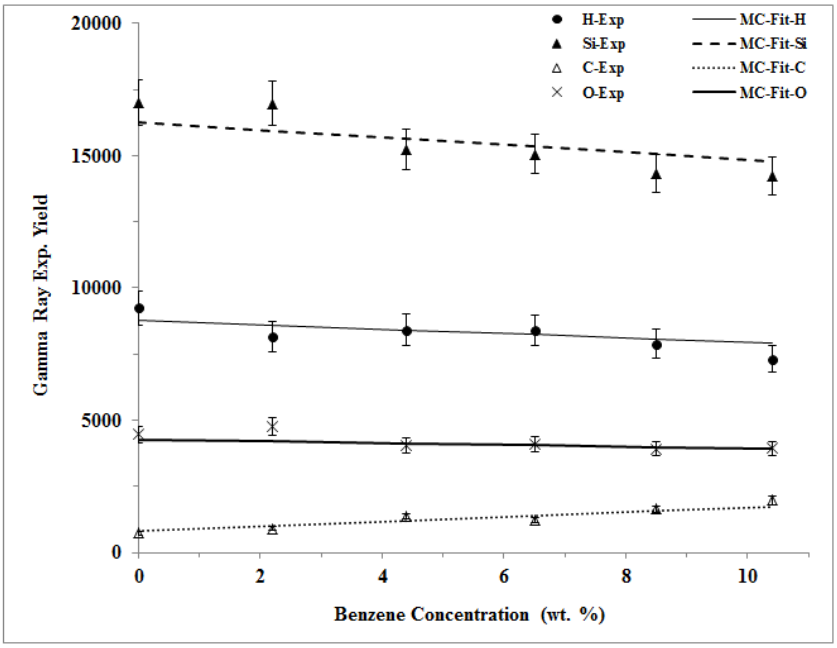

Figure 5.16: Integrated yield of 1.78 MeV silicon, 4.44 MeV carbon, 6.13 MeV oxygen and 2.22 MeV hydrogen peaks from soil samples contaminated with 0.0-11 wt. % benzene concentration plotted as a function of benzene concentration. The lines fitted to the experimental data are results of Monte Carlo simulations.

This study has provided useful results on prompt gamma analysis of benzene-contaminated soil samples, moisture-dependent correlations of NIS and TNC prompt gamma ray intensities from the same sample. The data obtained in the present study can be used to develop a scheme to correct for loss of NIS gamma ray intensity due to the presence of sample moisture.

CHAPTER 6

CONCLUSION

In this study, toxic elements and petroleum hydrocarbons (PHCs) contaminated samples were analysed using Thermal Neutron Capture (TNC) and 14 MeV neutrons inelastic scattering (NIS) based Prompt Gamma-ray Neutron Activation Analysis (PGNAA) techniques. The study was undertaken at KFUPM 350 keV accelerator and MP320 portable neutron generator laboratories using $LaBr_3$:Ce, $CeBr_3$ and BGO gamma ray detectors. The toxic elements Mercury, Chromium, Nickel, Boron, Cadmium and Chlorine were chosen along with petroleum hydrocarbon (PHC) due to their significant adverse effect on the environment.

In the analysis of Hg, Cr, Ni, B, Cd and Cl-contaminated water samples minimum detection limit (MDC) have been measured for a $CeBr_3$ detector based PGNAA setup using thermal neutron capture technique. For $CeBr_3$ detector, the MDC$\pm\sigma_{MDC}$ of Hg, Cr, Ni, B, Cd and Cl were measured to be 0.15±0.05 wt.%, 1.03 ± 0.31 to 2.98 ± 0.91 wt.%, 1.98 ± 0.60 to 3.88 ± 1.18 wt.%, 24.4±7.43 ppm, 95.6±29.1 ppm and 1.47 ± 0.45 to 4.20 ± 1.28 wt.% respectively.

For the analysis of petroleum contamination soil samples, measurement were carried out using a $LaBr_3$:Ce detector based 14 MeV PGNAA setup using neutron inelastic scattering technique. Effect of moisture and petroleum contamination in prompt gamma yields of carbon, silicon, oxygen and hydrogen for the soil samples were measured. The study showed the moderating effect of hydrogen in moisture and petroleum causing loss of 14 MeV neutron flux and a reduction in silicon (Si) intensity. This established the decrease

silicon (Si) intensity with increase moisture and petroleum concentration in moisture and petroleum contamination soil samples respectively.

Additionally, energy resolution of the $CeBr_{3,}$ and the $LaCl_3$:Ce detectors, were measured for 0.3 to 8.6 MeV gamma rays. The energy resolution of the detectors, which varies as $1/\sqrt{E_\gamma}$ was found to be varied from 7.09 ± 0.02 to 0.90 ± 0.01 % over this energy range.

References

[1] Sun Y, Zhou Q, Xie X, Liu R (2010) Spatial, sources and risk assessment of heavy metal contamination of urban soils in typical regions of Shenyang, China. J Hazard Mater 174(1):455–462

[2] Ravankhah, N., Mirzaei, R., & Masoum, S. (2016). Spatial Eco-Risk Assessment of Heavy Metals in the Surface Soils of Industrial City of Aran-o-Bidgol, Iran. *Bulletin of Environmental Contamination and Toxicology*, *96*(4), 516–23. http://doi.org/10.1007/s00128-016-1761-3

[3] Xie H, Li J, Zhang C, Tian Z, Liu X, Tang C, Han Y, Liu W (2014) Assessment of heavy metal concentrations in surface soil in the Lhasa–Shigatse–Nam Co area of the Tibetan Plateau, China. Bull Environ Contam Toxicol 93(2):192–198

[4] A.A. Naqvi, M.S. Al-Anezi, Zameer Kalakada, A.A. Isab, M.Raashid, Khateeb-ur-Rehman, F.Z. Khiari, M.A. Garwan, O.S.B. Al-Amoudi, M. Maslehuddin. "Detection efficiency of low levels of boron and cadmium with a $LaBr_3$:Ce scintillation detector". *Nuclear Instruments and Methods in Physics Research, section A* 665 (2011) 74-79.

[5] K.A. Cengiz, T. Levent, Murat Dikilitas, Muhammed Ashraf, Cientia Horticulturae 121 (2009) 284-288.

[6] F. Zahir, S. J. Rizwi, S. K. Haq, and R. H. Khan, "Low dose mercury toxicity and human health," vol. 20, pp. 351–360, 2005.

[7] Lebel, J., Mergler, D., Lucotte, M., Amorim, M., Dolbec, J., Miranda, D., Arantes, G., Rheault, I., Pichet, P., 1996. Evidence of early nervous system dysfunction in Amazonian populations exposed to low-levels of methylmercury. Neurotoxicology 17 (1), 157–167.

[8] F. Ben Hamida, A. Troudi, and M. Sefi, "The protective effect of propylthiouracil against hepatotoxicity induced by chromium in adult mice," vol. 32, no. 2, pp. 235–245, 2016.

[9] Dutta Deb D, Parimala G, Saravana Devi S and Chakrabarti T (2012) Role of Carum copticum seeds immodulating chromium-induced toxicity on human bronchial epithelial cells and human peripheral blood lymphocyte. Experimental and Toxicologic Pathology 64: 889–897.

[10] Chervona Y, Arita A, Costa M. (2012). Carcinogenic metals and the epigenome: understanding the effect of nickel, arsenic, and chromium. Metallomics. Jul, Vol. 4(7), pp. 619-27.

[11] Forgacs Z, Massányi P, Lukac N, Somosy Z.(2012). Reproductive Toxicology Of Nickel – Review. J Environ Sci Health A Tox Hazard Subst Environ Eng., Vol. 47(9), pp. 1249-60.

[12] Mullaney, J. R.; D. L. Lorenz, and A. D. Arntson (2009), Chloride in Groundwater and Surface Water in Areas Underlain by the Glacial Aquifer System, Northern United States. National Water-Quality Assessment Program Scientific Investigations Report # 2009–5086, U.S. Department of the Interior *and* U.S. Geological Survey [World Wide Web: http://www.usgs.gov]

[13] Bubeck, R.C., W.H., Diment, B.L., Deck, A.L Baldwin,., and S.D., Lipton (1971), Runoff of deicing salt—Effect on Irondequoit Bay, Rochester, New York: Science, Vol. 172, pp. 1128–1132.

[14] Huling, E.E., and Hollocher, T.C.(1972), Groundwater contamination by road salt—Steady-state concentrations in east-central Massachusetts: Science, Vol. 176, pp. 288–290.

[15] Wulkowicz, G.M., and Saleem, Z.A.(1974). Chloride balance of an urban basin in the Chicago area: Water Resources Research, Vol.. 10, No. 5, pp. 974–982.

[16] U.S. Environmental Protection Agency,(1992) Secondary drinking water regulations—Guidance for nuisance chemicals: EPA 810/K–92–001 [*http://www.epa.gov/safewater/consumer/2ndstandards.html*.]

[17] S. Peng, Q. Zhou, Z. Cai, and Z. Zhang, "Phytoremediation of petroleum contaminated soils by Mirabilis Jalapa L . in a greenhouse plot experiment," vol. 168, pp. 1490–1496, 2009.

[18] C. Hall, P. Tharakan, J. Hallock, C. Cleveland, M. Jefferson, Hydrocarbons and the evolution of human culture, Nature 426 (2003) 318–322.

[19] J.M. Pena-Castro, B.E. Barrera-Figueroa, L.F. Linares, R.R. Medrano, Isolation and identification of up-regulated genes in bermudagrass roots (*Cynodon dactylon* L.) grown under petroleum hydrocarbon stress, Plant Science 170 (2006) 724–731.

[20] N. Merkl, R.S. Kraft, C. Infante, Phytoremediation in the tropics-influence of heavy crude oil on root morphological characteristics of graminoids, Environmental Pollution 138 (2005) 86–91.

[21] K. Das, A.K. Mukherjee, Crude petroleum-oil biodegradation efficiency of *Bacillus subtilis* and *Pseudomonas aeruginosa* strains isolated from a petroleum-oil contaminated soil from North-East India, Bioresource Technology 98 (2007) 1339–1345.

[22] E.J. Joner, D. Hirmann, O.H.J. Szolar, D. Todorovic, C. Leyval, A.P. Loibner, Priming effects on PAH degradation and ecotoxicity during a phytoremediation experiment, Environmental Pollution 128 (2004) 429–435.

[23] M.J. Smith, T.H. Flowers, H.J. Duncan, J. Alder, Effects of polycyclic aromatic hydrocarbons on germination and subsequent growth of grasses and legumes in freshly contaminated soil and soil with aged PAHs residues, Environmental Pollution 141 (2006) 519–525.

[24] A. Meudec, N. Poupart, J. Dussauze, E. Deslandes, Relationship between heavy fuel oil phytotoxicity and polycyclic aromatic hydrocarbon contamination in *Salicornia fragilis*, Science of the Total Environment 381 (2007) 146–156.

[25] N. Merkl, R.S. Kraft, M. Arias, Effect of the tropical grass *Brachiaria brizantha* (Hochst. ex A. Rich.) Stap on microbial population and activity in petroleumcontaminated soil, Microbiological Research 161 (2006) 80–91.

[26] K. Euliss, C-h. Ho, A.P. Schwab, S. Rock, M.K. Banks, Greenhouse and field assessment of phytoremediation for petroleum contaminants in a riparian zone, Bioresource Technology 99 (2008) 1961–1971.

[27] H.H. Liste, D. Felgentreu, Crop growth, culturable bacteria, and degradation of petro hydrocarbons (PHCs) in a long-term contaminated field soil, Applied Soil Ecology 31 (2006) 43–52.

[28] Harding, G., 2004, "Explosives detection with X-ray scatter tomography". *Radiation Phys. Chem*., Vol. 71(2004) pp. 750-756

[29] Jorgelina C.A de Wuilloud, Rodolfo G Wuilloud, María F Silva, Roberto A Olsina and Luis D Martinez, 2002. "Sensitive determination of mercury in tap water by cloud point extraction pre-concentration and flow injection-cold vapor-inductively coupled plasma optical emission spectrometry". Spectrochimica Acta Part B: Atomic Spectroscopy, vol. 57, pp. 365 – 374.

[30] https://en.wikipedia.org/wiki/Gravimetric_analysis

[31] A. J. Zimmerman and D. C. Weindorf, "Heavy Metal and Trace Metal Analysis in Soil by Sequential Extraction : A Review of Procedures," *International Journal of Analytical Chemistry*, vol. 2010, 2010

[32] Rosalba Gaudiuso , Marcella Dell'Aglio , Olga De Pascale , Giorgio S. Senesi and Alessandro De Giacomo, 2010." Laser Induced Breakdown Spectroscopy for Elemental Analysis in Environmental, Cultural Heritage and Space Applications: A Review of Methods and Results". *Sensors* Vol. 10, pp. 7434-7468; doi:10.3390/s100807434

[33] E. H. Seabury, B. W. Blackburn, D. L. Chichester, C. J. Wharton, and A. J. Caffrey, "Comparison of DD, DT and Cf-252 neutron excitation of light and medium mass nuclei for field PGNAA applications," vol. 261, pp. 839–844, 2007.

[34] Csikai, J., 1987. "CRC Handbook of Fast Neutron Generators", Vol.I and II.CRC Press, Boca Raton, Florida.

[35] Hussein, E.M.A., 2003. "Handbook on Radiation Probing, Gauging, Imaging and Analysis", Vols.I and II.Kluwer Academic Publishers, Dordrecht.

[36] Seabury E. H. and A. J. Caffery, "Explosive Detection and Identification by PGNAA". Report # INL/EXT-06-01210 (April-2006). *Idaho National Laboratory*, Idaho Falls, Idaho 83415, USA.

[37] Naqvi, A. A., Zameer Kalakada, Faris A. Al-Matouq, M. Maslehuddin and O.S.B. Al-Amoudi. "Prompt Gamma-Ray Analysis of Chlorine in Superpozz Cement Concrete". *Nuclear Inst. and Methods in Physics Research*, A Vol. 693 (November 2012), pp. 67-73

[38] Naqvi, A. A., Zameer Kalakada, Faris A. Al-Matouq, M. Maslehuddin and O.S.B. Al-Amoudi. "Chlorine Detection in Fly Ash Concrete using a Portable Neutron Generator". *Applied Radiation and Isotopes* Vol. 70 (2012) pp.1671-4.

[39] Buffler, "A Contraband detection with fast neutrons"; *Radiation Physics And Chemistry*, Vol. 71(2004) pp.853-861

[40] Lee, W.C., Mahood, D.B., Ryge, P., Shea, P. and Gozani, T., 1995. "Thermal neutron analysis (TNA) explosive detection based on electronic neutron generators".*Nucl.Instrum. Methods B* 99, pp. 739–742.

[41] Brown, D.R., Gozani, T., Loveman, R., Bendahan, J., Ryge, P., Stevenson, J., Liu, F. and Sivakumar, M., 1994. "Application of pulsed fast neutrons analysis to cargo inspection".*Nucl.Instrum.Methods. A* 353, pp. 684–688.

[42] Overley, J.C., 1995. “Explosives detection through fast-neutron time-of-flight attenuation measurements”. *Nucl.Instrum. Methods B* 99, pp. 728–732.

[43] Overley, J.C., Chmelik, M.S., Rasmussen, R.J., Sieger, G.E., Schofield, R.M.S. and Lefevre, H.W., 1997. “Results of tests for explosives in luggage from fast-neutron time-of-flight transmission measurements”. *Proc. Int. Soc. Opt. Eng.* 2867, pp. 219–222.

[44] http://www.iki.kfki.hu/nuclear/research/index_en.shtml

[45] Lewis Chisholm Thompson, 1952.” Gamma Rays Produced by the Inelastic Scattering of 14 Mev. Neutrons” the Rice Institute, Houston, Texas

[46] Briesmeister J. F. (Ed). 1997. “MCNP4B2 –A General Monte Carlo N-Particles Transport Code”. *Los Alamos National Laboratory Report* LA-12625-M, Version 4A.

[47] Rinard, P.: Neutron interactions with matter, Los Alamos Technical Report, available at: http://www.fas.org/sgp/othergov/doe/ lanl/lib-www/la-pubs/00326407.pdf, 2009

[48] Naqvi A. A., Maslehuddin M., Garwan M. A., Nagadi M. M., Al-Amoudi O.S. B., Raashid M., and Khateeb-ur-Rehman, 2010. “Effect of Silica Fume Addition on the PGNAA Measurement of Chlorine in Concrete”. *Applied Radiation Isotopes*, 68, 412-417.

[49] Naqvi A.A., F.Z.Khiari, F.A.Liadi, Khateeb-ur-Rehman, M.A.Raashid, A.H.Isab, (2016). Moisture effect in prompt gamma measurements from soil samples .Applied Radiation and Isotopes, Vol. 115, pp. 61-66.

[50] Naqvi , A.A. , M.A. Garwan , M. Maslehuddin , M.M. Nagadi , O.S.B. Al-Amoudi, Khateeb-ur-Rehman , M. Raashid ,(2009). Prompt gamma analysis of fly ash, silica fume and Superpozz blended cement concrete specimen. Applied Radiation and Isotopes, Vol. 67, pp. 1707–1710

[51] A.A. Naqvi, Zameer Kalakada, M.S. Al-Anezi, **Faris. A. Al-Matouq**, M.Raashid, Khateeb-ur-Rehman, M. Maslehuddin. “Response tests of a $LaCl_3$:Ce scintillation detector with Low energy prompt Gamma Rays from Boron and Cadmium”. *Applied Radiation and Isotopes* 70 (2012) 882–887

[52] Gerhart C. Lowenthal,P. L. Airey. “Practical applications of radioactivity and nuclear radiations an introductory text for engineers, scientists, teachers and students”. *Cambridge university press*, 2001.

[53] Giaz, A., Pellegri, L., Riboldi, S., Camera, F., Blasi, N., Boiano, C., Bracco, A., Brambilla, S., Ceruti, S., Coelli, S., Crespi, F. C. L., Csatlòs, M., Frega, S., Gulyàs, J., Kraszna-horkay, A., Lodetti, S., Million, B., Owens, A., Quarati, F., Stuhl, L., Wieland, O., 2013. Characterization of large volume 3.5″ x 8″ $LaBr_3$:Ce detectors. Nuclear Instrument. Methods Phys. Res. Sect.A :Accel. Spectrum. Detect. Assoc. Equip. 729, 910–921.

[54] Naqvi, A.A., Al-Anezi,M.S., Kalakada,Z., AlMatouq,F.A., Maslehuddin,M., Gondal, M.A., Isab, A.A., Khateeb-ur,R., Dastageer,M., 2012a. Response tests of a $LaCl_3$:Ce scintillation detector with low energy prompt gamma-rays from boron and cadmium.Appl.Radiat.Isot.70,882–887.

[55] Naqvi, A.A.,Al-Matouq, F.A.,Khiari,F.Z., Isab,A.A.,Khateeb-urRehman, M.R.,2012b. Prompt gamma tests of $LaBr_3$:Ce and BGO detectors for detection of hydrogen, carbon and oxygen in bulk samples. Nucl. Instrum. Methods Phys. Res. Sect. A: Accel. Spectrom.Detect.Assoc.Equip.684,82–87.

[56] Menge, P.R., Gautier, G.,Iltis, A.,Rozsa, C.,Solovyev, V., 2007. Performance of large lanthanum bromide scintillators. Nucl. Instrum. Methods Phys. Res. Sect. A: Accel. Spectrum. Detec. Assoc. Equip. A 579,6–10.

[57] Choi H.D., Firestone R.B., Lindstrom R.M., Molnar G.L.; Mughabghab S.F.; Paviotti Corcuera R., Revay Zs.; Trkov A. and. Zhou C.M,(2006). Database of Prompt Gamma-Rays from Slow Neutron Capture for Elemental Analysis, INTERNATIONAL ATOMIC ENERGY AGENCY, VIENNA

[58] Camera, F., Giaz, A., Pellegri, L., Riboldi, S., Blasi, N., Boiano, C., Bracco, A., Brambilla, S., Ceruti,S., Coelli, S., Crisp, F. C. L., Csatlòs, M., Krasznahorkay, A., Gulyàs, J., Lodetti, S., Frega, S., Miani, A., Million, B., Stuhl, L., Wieland, O., 2014. Characterization of large volume 3.5″ x 8″ $LaBr_3$:Ce detectors for the HECTOR array. In: Proceedings of INPC 2013 – International Nuclear Physics Conference, Firenze, Italy,vol. 66, Article number 11008.

[59] Quarati, F.G.A., Dorenbos, P., Biezen J.vander, Owens Alan , Selle M., Parthier L., Schotanus P.(2013), Scintillation and detection characteristics of high-sensitivity $CeBr_3$ gamma-ray spectrometers . Nuclear Instruments and Methods in Physics Research A729, pp. 596–604.

[60] Naqvi A.A., F. Z. Khiari , M. Maslehuddin , M. A. Gondal ; O. S. B. Al-Amoudi , M.S. Ukashat , A. M. Ilyas , F. A. Liadi , A. A. Isab , Khateeb-ur-Rehman , M. Raashid , M. A. Dastageer. (2015). Pulse height tests of a large diameter fast $LaBr_3$:Ce scintillation detector. Applied Radiation and Isotopes Vol. 104 pp. 224–231.

[61] Naqvi A. A.; Khiari; F. Z.; Liadi F. A.; Khateeb-ur-Rehman; A. A. Isab (2016). Energy Resolution Measurements of $Cebr_3$ And $Lacl_3$:Ce Detectors. J Journal of Radioanalytical and Nuclear Chemistry Vol. 310 , pp. 849–855

[62] Naqvi, A.A., Nagadi, M.M., Rehman,Khateeb.-ur., Maslehuddin, M., Kidwai, S., 2003. Monte Carlo simulation of the KFUPM PGNAA facility. Radiat. Phys. Chem.66, 89–98.

[63] Gedcke D.A., 2001. “How counting statistics controls detection limits and peak precession”. In: ORTEC Application Notes AN59. Website: /www.ortec-online.com.

[64] Knoll G.F., Radiation Detection and Measurements, John Wiley, 2000.

[65] Khelifi R.; A. Amokrane and P. Bode (2007).Detection limits of pollutants in water for PGNAA using Am–Be source. Nuclear Instruments and Methods in Physics Research B 262, pp. 329–332.

Vitae

Name	: Liadi Fatai Ayofe
Nationality	: Nigeria
Date of Birth	: 6th July, 1985
Email	: fatay02@gmail.com
Address	: No 3 Wonsebolatan Street Mapoline, Allahu-Lateef Sawmill, Ede, Osun State, Nigeria.
Academic Background	: Master of Science in Physics, King Fahd University of Petroleum and Minerals, Dhahran, Saudi Arabia Bachelor of Technology in Physics/Computer Science Federal University of Technology, Minna, Niger State, Nigeria.

Publications

Refereed Journals

[1] A. A. Naqvi, F. Z. Khiari, **F. A. Liadi,** Khateeb-ur-Rehman, M. A. Raashid, & A. A. Isab. (2016). Moisture effect in prompt gamma measurements from soil samples. *Applied Radiation and Isotopes, 115, 61-66.* https://doi.org/10.1016/j. apradiso. 2016.06.010

[2] A. A. Naqvi, F. Z. Khiari, **F. A. Liadi,** Khateeb-ur-Rehman, & A. A. Isab. (2016). Energy resolution measurements of $CeBr_3$ and $LaCl_3$:Ce detectors. *Journal of Radioanalytical and Nuclear Chemistry, 310:849-855.* https://doi.org/10.1007/s10967-016-4904-4

[3] A. A. Naqvi, F. Z. Khiari, **F. A. Liadi,** Khateeb-ur-Rehman, & A. A. Isab. (2016). Performance tests of a large volume cerium tribromide ($CeBr_3$) scintillation detector. *Applied Radiation and Isotopes, 114: 50-56.* https://doi.org/10.1016/j.apradiso.2016.04.031

[4] A. A. Naqvi, F. Z. Khiari , M. Maslehuddin , M. A. Gondal ; O. S. B. Al-Amoudi , M.S. Ukashat , A. M. Ilyas , **F. A. Liadi** , A. A. Isab , Khateeb-ur-Rehman , M. Raashid , M. A. Dastageer. (2015). Pulse height tests of a large diameter fast $LaBr_3$:Ce scintillation detector. *Applied Radiation and Isotopes Vol. 104 pp. 224–231.* https://dx.doi.org/10.1016/j.apradiso.2015.07.009

Appendix A: MCNP Description

A.1 Monte Carlo N-Particles (MCNP) Code

Monte **C**arlo **N**-**P**articles code (MCNP) is general purpose software package for simulating nuclear processes. Monte Carlo method obtains physical quantities by simulating the interactions of a large number of individual particles, and recording some of their properties. The average behavior of particles in the physical system is then inferred from the average behavior of the simulated particles. Model of the PGNAA setup such as NIS- and TNC-based setups were obtained through Monte Carlo simulations. The MCNP code is used to transport neutral particles. It can be used in several transport modes; neutron only, photon only, electron only or combined neutron/photon transport where neutron interactions produce photons. The code can be used to replicate a statistical process such as the interaction of nuclear particles with materials. It is particularly useful for complex problems that cannot be modeled by computer codes that use mathematical techniques such as deterministic methods. The isolated probabilistic events that comprise a process are simulated sequentially. The probability distributions governing these events are statistically sampled to describe the entire process. In general, the simulation is performed on a digital computer since the number of trials necessary to effectively describe the phenomenon is usually quite large. The statistical sampling process is based on the selection of random numbers. Monte Carlo technique is preeminently realistic (a theoretical experiment). It consists of actually following each of many particles from a source throughout its life to its death in some terminal category (absorption, escape, etc.).

Probability distributions are randomly sampled using transport data to determine the outcome at each step of its life [46]. During the transport process the code specifically transports the predetermined particles and reaction channels. Generally, neutrons and gamma rays are the common neutral particles to be transported in the design of low energy nuclear physics experiments. Common nuclear interactions encountered by the neutral particles in such experiments are: capture, elastic and inelastic scattering etc. In the following brief, descriptions of these processes relevant to MCNP code are given.

A. 1.1 Theory of Particle Interactions

A.1.1.1 Neutron Interactions

There are many ways in which neutron can interact with the nucleus. It can be one of two main types, either scattering (including elastic and inelastic) or absorption. When a neutron is scattered by a nucleus, the direction and the speed of neutron change but the number of protons and neutrons of the nucleus remain the same just as it had before the interaction. When a neutron is absorbed by a nucleus, several fission can be induced or radiations can be emitted such as (n, γ), (n, f), (n, α) etc… The MCNP code takes care of the transport of the respective particle with built-in theoretical basis for the required reaction. The PGNAA setups design calculations of this study mainly needed inelastic scattering as well as capture processes of the particles.

Inelastic Scattering

Scattering moderates or reduces neutrons energy and provides the basis for some neutron detectors. Inelastic scattering is a process in which the kinetic energy of an incident particle is not conserved. The nucleus undergoes internal rearrangement and move to excited state

from which it finally releases radiation [47]. The treatment of inelastic scattering depends upon the particular inelastic reaction chosen. Inelastic reactions are defined as (n, ***y***) reactions such as *(n, n')*, *(n, 2n)*, *(n, f)*, *(n, n', α)* in which ***y*** includes at least one neutron. For many inelastic reactions, such as *(n,2n),* more than one neutron can be emitted for each incident neutron. The weight of each exiting particle is always the same as the weight of the incident particle minus any implicit capture. Various scattering laws that are sampled independently from the cross-section files for each exiting particle govern the energy of exiting particles. Which law is used is prescribed by the particular cross-section evaluation used. In fact, more than one law can be specified, and the particular one used at a particular time is decided with a random number.

The exiting particle energy and direction in the target -at rest- (laboratory) coordinate system are related to the center of mass energy and direction as follows [46]:

$$E' = E'_{cm} + \frac{E + 2\mu_{cm}(A+1)\sqrt{EE'_{cm}}}{(A+1)^2}, \text{ and } \mu_{lab} = \mu_{cm}\sqrt{\frac{E'_{cm}}{E'}} + \frac{1}{A+1}\sqrt{\frac{E}{E'}} \quad (2.1)$$

Where:

E' = Exiting particle energy (laboratory)

E'_{cm} = Exiting particle energy (center of mass)

E = Incident particle energy (laboratory)

μ_{cm} = Cosine of center of mass scattering angle

μ_{lab} = Cosine of laboratory scattering angle

A = Atomic weight ratio (mass of nucleus divided by mass of incident particle.)

Neutron Capture

MCNP treats neutron capture in one of two ways: analog or implicit. Either way, the incident incoming neutron energy does not include the relative velocity of the target nucleus from the free gas thermal treatment because non-elastic reaction-cross sections are assumed to be nearly independent of temperature. In MCNP, "absorption" and "capture" are used interchangeably, σ_c and σ_a are used interchangeably also [46].

a. **Analog Capture**: In analog capture, the particle is killed with probability σ_a / σ_T where σ_a and σ_T are the absorption and total cross sections of the collision nuclide at the incoming neutron energy respectively. The absorption cross section is specially defined for MCNP as the sum of all (n, x) cross sections, where ***x*** is anything except neutrons. Thus σ_a is the sum of $\sigma_{n,\gamma}$, $\sigma_{n,\alpha}$, $\sigma_{n,d}$ . . . etc. For all particles killed by analog capture, the entire particle energy and weight are deposited in the collision cell.

b. **Implicit Capture:** For implicit capture, the neutron weight W_n is reduced to W_n' such that $W_n' = [1 - (\sigma_a / \sigma_T)]W_n$, the fraction (σ_a / σ_T) of the incident particle weight and energy is deposited in the collision cell corresponding to that portion of the particle that was captured. Implicit capture is the default method of neutron capture in MCNP [46].

A.1.1.2 Photon Interactions

Photons interact with mater via three different ways: photoelectric effect, pair production and scattering.

Photoelectric Effect

The photoelectric effect consists of the absorption of the incident photon of energy ***E***, with the consequent emission of several fluorescent photons and the ejection (or excitation) of an orbital electron of binding energy ***e*** < ***E***, giving the electron a kinetic energy of ***E*** - ***e***. Zero, one, or two fluorescent photons are emitted. The description of those three cases is as follows [46]:

(1) Zero photons greater than 1 keV are emitted. In this event, the cascade of electrons that fills up the orbital vacancy left by the photoelectric ejection produces electrons and low-energy photons. These particles can be followed in Mode P E problems, or be treated with the TTB (Thick-Target Bremsstrahlung) approximation, or be assumed to deposit energy locally. Because no photons are emitted by florescence (some may be produced by electron transport or the TTB model), the photon track is terminated. This photoelectric "capture" of the photon is scored like analog capture in the summary table of the output file. Implicit capture is not possible.

(2) One fluorescent photon of energy greater than 1 keV is emitted. The photon energy E' is the difference in incident photon energy ***E***, less than the ejected electron kinetic energy ***E*** - ***e***, and less than the residual excitation energy e' that is ultimately dissipated by further Auger processes. This dissipation leads to additional electrons or photons of still lower energy. The ejected electron and any Auger electrons can be transported or treated with the TTB approximation. In general, $E' \leq E - (E - e) - e' \leq e - e'$

(3) Two fluorescence photons can occur if the residual excitation e' of process (2) exceeds 1 keV. An electron of binding energy e'' can fill the orbit of binding energy

e¢, emitting a second fluorescent photon of energy E¢= e¢- e¢. As before, the residual excitation e¢is dissipated by further Auger events and electron production that can be modeled with electron transport in Mode P E calculations, approximated with the TTB model, or assumed to deposit all energy locally. These secondary transitions come from all upper shells and go to **L** shells.

Pair Production

This process is considered only in the field of a nucleus. The threshold is $2mc^2 = [1+(m/M)]$@1.022 MeV, where ***M*** is the nuclear mass and ***m*** is the mass of the electron. There are three cases [46]:

(1) In the case of electron transport (Mode P E), the electron and positron are created and banked and the photon track terminates.

(2) For Mode P problems with the TTB approximation, both an electron and positron are produced but not transported. Both particles can make TTB approximation photons. If the positron is below the electron energy cutoff, then it is not created and a photon pair is created as in the following case.

(3) For Mode P problems when positrons are not created by the TTB approximation, the incident photon of energy ***E*** vanishes. The kinetic energy of the created positron/electron pair, assumed to be $E - 2mc^2$, is deposited locally at the collision point. The positron is considered to be annihilated with an electron at the point of collision, resulting in a pair of photons, each with the incoming photon weight, and each with energy of $2mc^2 = 0.511$ MeV. The first photon is emitted isotropically, and the second is emitted in the opposite direction. The very rare single-annihilation

photon of 1.022 MeV is omitted.

Incoherent (Compton) Scattering

To model Compton scattering it is necessary to determine the angle q of scattering from the incident line of flight (and thus the new direction), the new energy $E¢$ of the photon, and the recoil kinetic energy of the electron, $E - E¢$. The recoil kinetic energy can be deposited locally, and can be transported in Mode P E problems, or can be treated with the TTB approximation. Incoherent scattering is assumed to have the differential cross section $s_1(Z,a,m)dm = I(Z,v)K(a,m)$ where $I(Z,v)$ is an appropriate scattering factor modifying the Klein-Nishina cross section in Equation (2.2).

The differential cross section for the process is given by the Klein-Nishina formula:

$$K(\alpha,\mu)d\mu = \pi r_0^2 \left(\frac{\alpha'}{\alpha}\right)^2 \left[\frac{\alpha'}{\alpha} + \frac{\alpha}{\alpha'} + \mu^2 - 1\right] d\mu \qquad (2.2)$$

Where r_o is the classical electron radius 2.817938 x 10^{-13}cm, a and $a¢$ are the incident and final photon energies in units of 0.511 MeV [$a = E/(mc^2)$, where m is the mass of the electron and c is the speed of light], and $a¢ = a/[1+a(1-m)]$[46].

Coherent (Thomson) Scattering

Thomson scattering involves no energy loss, and thus is the only photon process that cannot produce electrons for further transport and that cannot use the TTB approximation. Only the scattering angle q is computed, and then the transport of the photon continues. The differential cross section is $s_2(Z,a,m)dm = C^2(Z,v)T(m)dm$ where $C(Z,v)$ is a form factor modifying the energy-independent Thomson cross-section $T(m) = pr_o^2(1+m^2)dm$ [46].

A.1.2 MCNP Code Features

Various features, concepts, and capabilities of MCNP are summarized in this section. Files created in MCNP contains the information to describe the various parts of the setup design including: **a)** Geometry specification, **b)** Materials and cross-section evaluations, **c)** The neutron, photon, or electron source location and characteristics, **d)** The desired type of answers or tallies, **e)** Variance reduction techniques used to improve the efficiency [46].

Experimental Geometry Specification

MCNP geometry treats an arbitrary three-dimensional configuration of user-defined materials in geometric cells bounded by first- and second-degree surfaces and fourth-degree elliptical tori. The cells are defined by the intersection, unions, and complements of the regions bounded by the surfaces. Surfaces are defined by supplying coefficients to the analytic surface equations or, for certain types of surfaces, known points on the surfaces. MCNP has a more general geometry than is available in most combinatorial geometry codes. Instead of combining several predefined geometrical bodies as in a combinatorial geometry scheme, MCNP gives the user the flexibility of defining geometrical regions from all the first and second degree surfaces of analytical geometry and elliptical tori and then of combining them with Boolean operators. The code does extensive internal checking to find input errors. Additionally, the geometry-plotting capability in MCNP helps the user check for geometry errors [46].

Material and Nuclear Cross-Section Data Library

MCNP code uses continuous-energy nuclear and atomic data libraries. Over 500 neutron interaction tables are available for approximately 100 different isotopes and elements. Multiple tables for a single isotope are provided primarily because data have been derived from different evaluations, but also because of different temperature regimes and different processing tolerances. Photon interaction tables including coherent and incoherent scattering, photoelectric absorption exist for all element from $Z=1$ through $Z=94$. Cross sections for nearly 2000 dosimetry or activation reactions involving over 400 target nuclei in ground states are part of the MCNP data package. Users may select specific data tables through unique identifiers for each table [46].

Neutron and Gamma Source Specification

In MCNP the user is allowed to specify a wide variety of source conditions without making code modifications. Independent probability distributions may be specified for the source variables of energy, time, position and direction, and for other parameters such as starting cell(s) or surface(s). Information about the geometrical extent of the source can also be given. The source selection list in the input file is symbolized by SDEF, which is followed by some source parameter, such as position, energy, radiation type…etc. [46].

Tallies and Output

Tallies represent the digital record of the random events from neutron interaction with the sample elements. MCNP can be instructed to make various tallies related to particle current, particle flux, and energy deposition. MCNP tallies are normalized to be per starting

particle except for a few special cases with criticality sources. Currents can be tallied as a function of direction across any set of surfaces, surface segments, or sum of surfaces in the problem. Charge can be tallied for electrons and positrons. Fluxes across any set of surfaces, surface segments, sum of surfaces, and in cells, cell segments, or sum of cells are also available. Similarly, the fluxes at designated detectors are standard tallies [46].

Estimation of Monte Carlo Errors

MCNP tallies are normalized to be per starting particle and are printed in the output accompanied by a second number ***R***, which is the estimated relative error defined to be one estimated standard deviation of the mean $S_{\bar{x}}$ divided by the estimated mean $\bar{x}$ ($R = S_{\bar{x}} / \bar{x}$). In MCNP, the quantities required for this error estimate are computed after each complete Monte Carlo history, which accounts for the fact that the various contributions to a tally from the same history are correlated. For a well-behaved tally, ***R*** will be proportional to $1/\sqrt{N}$ where ***N*** is the number of histories. Thus, we must increase the total number of histories fourfold in order to halve ***R***. For a poorly behaved tally, ***R*** may increase as the number of histories increases. The quantity ***R*** should be less than 0.10 to produce generally reliable confidence intervals. For a given MCNP run, the computer consumed time ***T*** proportional to ***N***. Thus:

$R = C/\sqrt{T}$, where ***C*** is a positive constant. There are two ways to reduce ***R*** (estimated relative error); by increasing ***T*** and / or decreasing ***C***. Computer budgets often limit the utility of the first approach. For example, if it has taken 2 hours to obtain $R = 0.10$, then 200 hours will be required to obtain $R = 0.01$. For this reason, MCNP has special variance

reduction techniques for decreasing $\boldsymbol{C}$, the constant $\boldsymbol{C}$ depends on the tally choice and / or the sampling choices [46].